University of Vermont
ScholarWorks @ UVM

Graduate College Dissertations and Theses | Dissertations and Theses

2019

Multi-Polarized Channel Characterization

Marcia Golmohamadi
University of Vermont

Follow this and additional works at: https://scholarworks.uvm.edu/graddis

 Part of the Electrical and Electronics Commons

Recommended Citation
Golmohamadi, Marcia, "Multi-Polarized Channel Characterization" (2019). *Graduate College Dissertations and Theses*. 1026.
https://scholarworks.uvm.edu/graddis/1026

This Dissertation is brought to you for free and open access by the Dissertations and Theses at ScholarWorks @ UVM. It has been accepted for inclusion in Graduate College Dissertations and Theses by an authorized administrator of ScholarWorks @ UVM. For more information, please contact donna.omalley@uvm.edu.

Multi-polarized Channel Characterization

A Dissertation Presented

by

Marcia Golmohamadi

to

The Faculty of the Graduate College

of

The University of Vermont

In Partial Fulfillment of the Requirements
for the Degree of Doctor of Philosophy
Specializing in Electrical Engineering

May, 2019

Defense Date: February 15, 2019
Dissertation Examination Committee:

Jeff Frolik, Ph.D., Advisor
Taras Lakoba, Ph.D., Chairperson
Mads Almassalkhi, Ph.D.
Tian Xia, Ph.D.
Cynthia J. Forehand, Ph.D., Dean of the Graduate College

Abstract

Machine-to-machine (M2M) communication is becoming an important aspect of warehouse management, remote control, robotics, traffic control, supply chain management, fleet management and telemedicine. M2M is expected to become a significant portion of the Industrial Internet and, more broadly, the Internet of Things (IoT). The environments in which M2M systems are expected to operate may be challenging in terms of radio wave propagation due to their cluttered, multipath nature, which can cause deep signal fades and signal depolarization. Polarization diversity in two dimensions is a well-known technique to mitigate such fades. But in the presence of reflectors and retarders where multipath components arrive from any direction, we find the detrimental effects to be three-dimensional and thus consider herein mitigation approaches that are also 3D. The objectives of this dissertation are three. First, to provide a theoretical framework for depolarization in three dimensions. Second, to prepare a tripolar antenna design that meets cost, power consumption, and simplicity requirements of M2M applications and that can mitigate the expected channel effects. Finally, to develop new channel models in three dimensional space for wireless systems.

Accordingly, this dissertation presents a complete description of 3D electromagnetic fields, in terms of their polarization characteristics and confirms the advantage of employing tripolar antennas in multipath conditions. Furthermore, the experimental results illustrate that highly variable depolarization occurs across all three spatial dimensions and is dependent on small changes in frequency and space. Motivated by these empirical results, we worked with a collaborating institution to develop a three-dimensional tripolar antenna that can be integrated with a commercially available wireless sensor. This dissertation presents the testing results that show that this design significantly improves channels over traditional 2D approaches. The implications of tripolar antenna integration on M2M systems include reduction in energy use, longer wireless communication link distances, and/or greater link reliability. Similar results are shown for a planar antenna design that enables four different polarization configurations. Finally, the work presents a novel three-dimensional geometry-based stochastic channel model that builds the channel as a sum of shell-like sub-regions, where each sub-region consists of groups of multipath components. The model is validated with empirical data to show the approach may be used for system analyses in indoor environments.

Citations

Material from this dissertation has been published in the following forms:

Golmohamadi, M., Chowdhury, S., Jamison, J., Kravitz, E. and Frolik, J.. 2018, July. 28 GHz Channel Measurements in High Multipath, Indoor Environments. In 2018 IEEE International Symposium on Antennas and Propagation & USNC/URSI National Radio Science Meeting (pp. 767-768). IEEE.

Golmohamadi, M., Chowdhury, S. and Frolik, J.. 2017, July. Markov modeling of spatial variations in multipath. In Antennas and Propagation & USNC/URSI National Radio Science Meeting, 2017 IEEE International Symposium on (pp. 611-612). IEEE.

Golmohamadi, M., Ramirez, R., Hewgill, B., Jamison, J., Frolik, J. and Weller, T.. 2017, March. Characterization of a geometrically constrained tripolar antenna under M2M channel conditions. In Antennas and Propagation (EUCAP), 2017 11th European Conference on (pp. 2998-3002). IEEE.

Golmohamadi, M. and Frolik, J.. 2016, April. Depolarization in three dimensions: theoretical formulations and empirical results. In Wireless and Microwave Technology Conference (WAMICON), 2016 IEEE 17th Annual (pp. 1-6). IEEE.

Materials from this dissertation have been submitted for publication in the following forms:

Golmohamadi, M., Narbudowicz, A. and Frolik, J.. Submitted on December 1, 2018. Mitigating indoor channels with hybrid polarization diversity. IEEE Antennas and Wireless Propagation Letters. **in revision**

Golmohamadi, M. and Frolik, J.. Submitted on December 28, 2018. A geometric scattering model for circularly polarized indoor channels. IEEE Transactions on Antennas and Propagation. **in revision**.

Golmohamadi, M. and Frolik, J.. Submitted on January 20, 2019. A 3D Stokes Framework for Wireless Depolarized Channels. Progress In Electromagnetics Research (PIER) Letters. **accepted**.

Acknowledgements

Firstly, I would like to express my sincere gratitude to my advisor Professor Jeff Frolik for the continuous support of my Ph.D study and related research, for his patience, motivation, and immense knowledge. His guidance helped me in all the time of research.

I would also like to thank my committee members, Professors Taras Lakoba, Mads Almassalkhi, and Tian Xia for their insightful comments and encouragement.

My sincere thanks also goes to Dr. Tom Weller, Dr. Ramiro Ramirez, and Dr. Adam Narbudowicz, who collaborated with us on conducting this research and publishing several articles.

I thank my fellow labmates in UVM Sensor Networks & Wireless Lab for the stimulating discussions, for the times we were working together before deadlines, and for all the fun we have had.

Last but not the least, I would like to thank my family for supporting me throughout writing this dissertation and my life in general.

Table of Contents

List of Figures

List of Tables

1 Introduction

1.1 Motivation

Wireless systems are being deployed in evermore complex environments. Such environments can consist of a variety of surfaces that block and/or reflect the wireless signals thus introducing non-line-of-sight (NLOS) and/or multipath conditions, respectively. Signals may arrive at the receiving antenna not only through the direct path, i.e., the line-of-sight (LOS) path, but also on multiple indirect paths, due to different electromagnetic effects such as signal reflection, diffraction. These signal components arrive with a certain delay, phase, and amplitude difference relative to the LOS component. We will call these signal components, multipath components (MPCs), and the phenomena, multipath propagation. Multipath can not only cause fading in a channel but also depolarize the transmitted signal [4]. A well-known approach to mitigating multipath is to leverage multiple branches whose fading statistics are poorly correlated [5]. Branches can, for example, consist of utilizing multiple frequencies, antennas, or polarizations. This is called channel diversity.

Machine-to-Machine (M2M) communication is the self-determining interaction of a large number of machine devices to perform sensing, processing, and actuation activities without human involvement [6]. This communication paradigm is becoming very popular in wide areas such as smart grids, e-healthcare, home area networks, intelligent transportation systems, environmental monitoring, smart cities, and industrial automation [7]. For M2M systems that involve multiple devices, coordinating multiple frequencies is not a tenable diversity approach, for it is possible that an appropriate frequency for one particular device to device link may exhibit deep fades in another. Employing multiple antennas (i.e., spatial diversity) requires elements to be located sufficiently far from each other ($\sim \lambda/2$) to guarantee decorrelation of fading effects. This constraint makes spatial diversity a less than desirable approach for applications where the size of the antenna system is a crucial design parameter. Cross-polarized antenna systems resolve this problem by using perpendicular antennas. This technique reduces the correlation while keeping antennas co-located.

Polarization diversity in two dimension has been long considered [8, 9]. However exploiting

all three polarizations in multipath conditions is comparatively a new concept [10]. Three dimensional polarization diversity can be regarded as a suitable technique for implementation for applications where device size and power consumption is a concern.

1.2 Concepts

In this section, I overview some basic concepts that have been largely used throughout this dissertation.

1.2.1 What is fading?

The wireless channel refers to the electromagnetic propagation environment that lies between a transmit antenna and a receive antenna. The transmitted electromagnetic wave interacts with the surrounding environment before reaching to the receiving antenna. The interaction of the electromagnetic waves with their surrounding is very complicated, especially in cluttered environments. The transmitted signal goes through several kinds of attenuation mechanisms: including path loss, shadowing, multipath attenuation etc. These fading types can be classified into two main categories: large-scale fading and small-scale fading.

Large-scale fading is the result of path loss and shadowing effects. The solution of Maxwell's equations reveal that the magnitude of the electric field in the free space is inversely proportional to the traveled path. The free space path loss can be expressed as follows [11].

$$\frac{P_r}{P_t} = \left[\frac{\sqrt{G_l}\lambda}{4\pi d}\right]^2 \tag{1}$$

where, P_r and P_t are the transmit and the receive power, respectively. $\sqrt{G_l}$ is the product of the transmit and receive antenna field radiation patterns and λ is the wavelength of the transmitted signal. d denotes the distance between the transmitting and receiving antenna. Another type of fading is shadowing that is the result of obstacles between the transmitter and the receiver. Since the variations due to both path loss and shadowing occur over large distances, they are categorized as large-scale fading types.

Small-scale fading, on the other hand, refers to variation in the received signal over very short distances (on the order of the signal wavelength) or short period of time or small movements

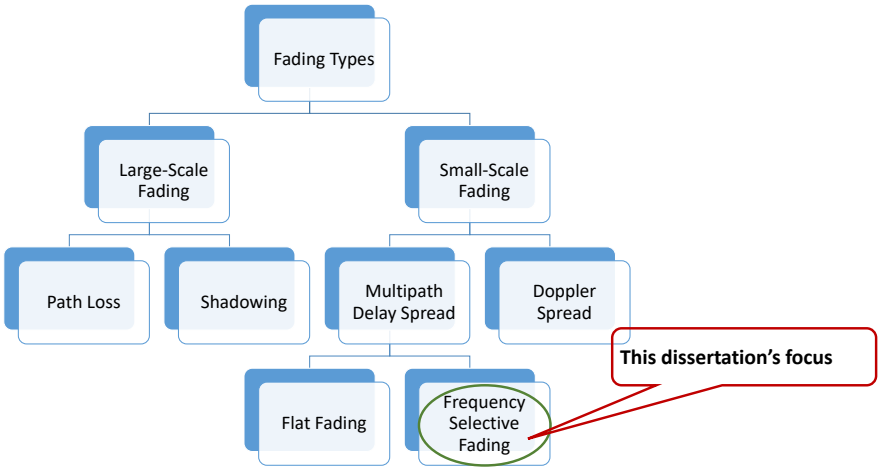

Figure 1.1: Types of fading in wireless communication

in frequency. Two phenomena cause small-scale fading in a wireless channel. First, multipath spread that is the outcome of the constructive and destructive interference of the different propagation paths arriving from various directions. Second, Doppler spread that is the result of moving the transmitter of a signal in relation to the receiver. Classification of fading types is shown in Fig. 1.1 [11]. Multipath fading can affect wireless communication channels in two general ways:

- Flat fading: This fading affects all the frequencies across a given channel almost equally.
- Frequency-selective fading: This fading affects different frequencies across the channel differently. Sometimes relatively deep nulls may be experienced in the frequency response. This effect can be reduced by exploiting diversity techniques [12]. The focus of this dissertation is mostly on the effects, characterization, and mitigation of this fading type in wireless channels.

The main mechanisms of multipath wave prorogation can be classified as follows (Fig. 1.2) [13]

- Reflection occurs when signal encounters a smooth surface (in sense of Rayleigh criteria [14]) that is large relative to the wavelength of the signal.
- Diffraction happens when the path is blocked by an object with large dimensions relative to wavelength of the signal and sharp edges. Diffraction causes bending of waves around

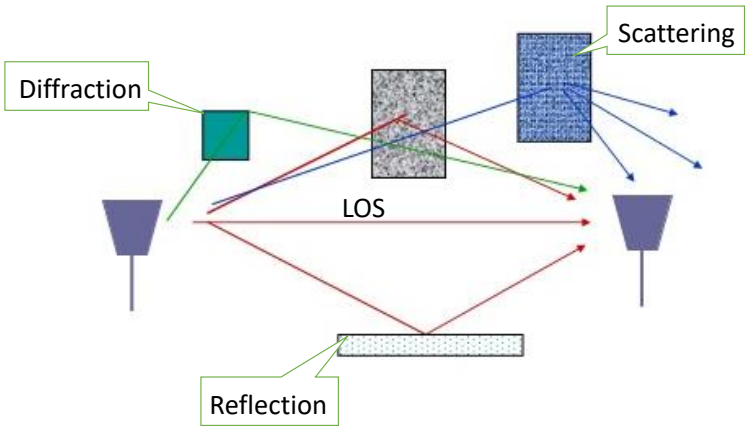

Figure 1.2: Main multipath propagation mechanisms.

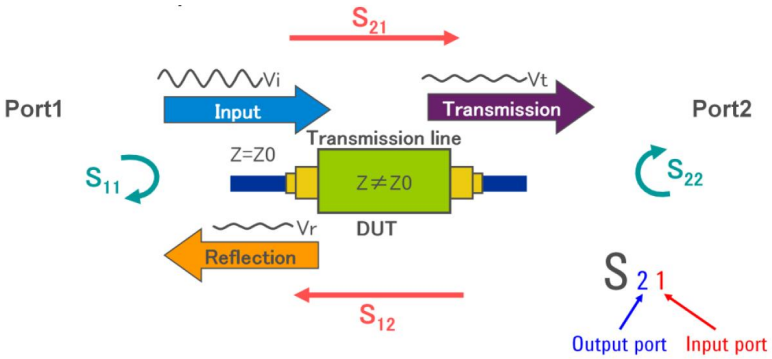

Figure 1.3: S-parameters

the obstacle [15].

- Scattering occurs when incoming signal hits an object that its size is the order of the wavelength of the signal or a rough surface. This phenomena causes signals to scatter in different directions [16, 17].

S-parameters are complex matrix that show Reflection/Transmission characteristics in frequency domain. Specifically, $S21$ is a measure of the signal coming out the port 2 of the measurement equipment (vector network analyzer) relative to the RF stimulus entering the port 1 of the device and shows the transmission loss or fading of the channel [18]. These parameters are illustrated in Fig. 1.3. The magnitude of the scattering parameter, S_{21} , over a bandwidth of

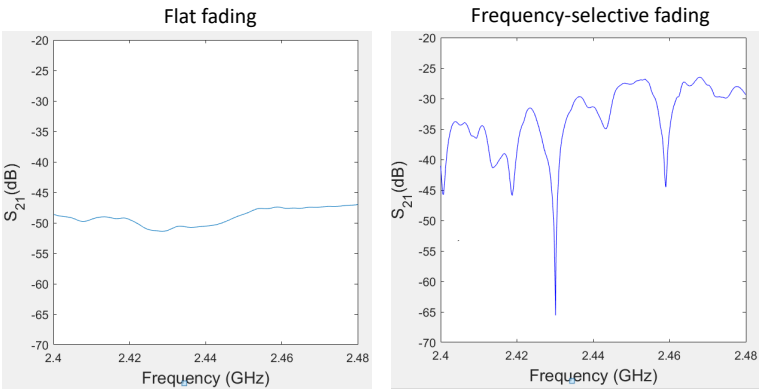

Figure 1.4: Measured S_{21} over frequency band of 2.40 GHz - 2.48 GHz. Left: flat fading channel. Right: frequency-selective channel

2.40 GHz - 2.48 GHz is shown in Fig. 1.4 and presents examples of a flat and a frequency-selective fading channel.

1.2.2 Rayleigh and Rician fading models

In cluttered environments where multipath components arrive from so many different directions, the deterministic methods are not able to describe radio channels and the statistical methods should be employed. Here, I introduce Rayleigh and Rician distributions that have been largely used for description of fading in multipath conditions.

Let a_n be the amplitude and θ_n be the relative phase of the n^{th} multipath component. Then, the received signal is [19]

$$y(t) = \sum_{n=1}^{N} a_n(t) e^{-j\theta_n(t)} \tag{2}$$

or

$$y(t) = y_I(t) + y_Q(t) \tag{3}$$

Both the in-phase, y_I, and the quadrature-phase, y_Q, components are the sum of numerous, N, random variables. Based on the central limit theorem, *pdf*'s of such summation are zero mean normal distributions. It is well known that the envelope of the sum of two quadrature Gaussian signals obeys a Rayleigh distribution [5]. The probability density function (*pdf*) of Rayleigh

distribution is given by [20].

$$p(r) = \frac{r}{\sigma^2} exp(-\frac{r^2}{2\sigma^2}),\ r \geq 0 \tag{4}$$

where, $r = \sqrt{y_I^2 + y_Q^2}$ is the envelope of the random variable r, and σ^2 is the average of the received power. In calculating radio link budget, we are interested in the probability that the envelope of the received signal drops below a specific value R. This probability is given by the corresponding cumulative distribution function (CDF)

$$P(R) = Pr(r \leq R) = \int_0^R p(r)dr = 1 - exp(-\frac{R^2}{2\sigma^2}) \tag{5}$$

On the other hand, Rician distribution describes a more benign wireless channel where in addition to so many multipath components, there is a strong LOS component. As the LOS signal becomes weaker, the distribution of the envelope of the received signal gets closer to Rayleigh distribution. The *pdf* of Rician distribution is given by

$$p(r) = \frac{r}{\sigma^2} exp(-\frac{r^2 + A^2}{2\sigma^2}) I_0(\frac{Ar}{\sigma^2}),\ r \geq 0 \tag{6}$$

where, the parameter A denotes the peak amplitude of the dominant or specular component and $I_0()$ is the modified Bessel function of the first kind and zero-order. Parameter K, which is the ratio of the power of the specular component to the power of nonspecular or diffuse components [21], is found

$$K = \frac{Average\ specular\ power}{Average\ diffuse\ power} = \frac{A^2}{2\sigma^2} \tag{7}$$

The parameter K is often given as a dB value. As the power of the specular component decreases, K gets closer to $-\infty$. Fig. 1.5 shows CDF plots of a Rayleigh channel and various Rician channels with different K values. As the value of K increases, the channel becomes a more benign Rician channel.

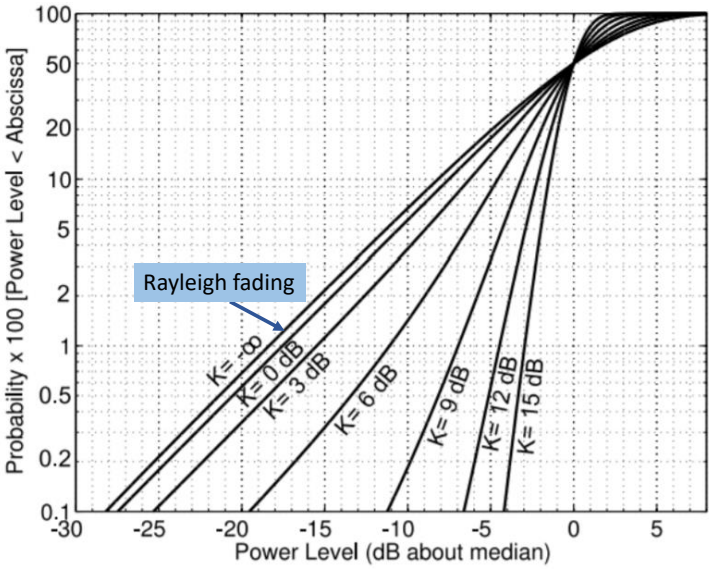

Figure 1.5: Rician CDF for different K factors [1].

1.2.3 Diversity techniques

Diversity in wireless communications leverages the idea that different links can experience fading effects that are statistically independent, if the links themselves are "distinct enough". Consider two independent Rayleigh fading paths, then diversity would leverage the one that is most favorable to the receiver. Choosing the branch with maximum signal strength reduces the probability that the received signal drops below a specified threshold which means that the reliability of the link increases. The four most common diversity methods are as follows [5]:

- Time diversity: the same data is transmitted at different time instants. This technique is efficient for time-varying channels. It utilizes coding of channel to mitigate channel fading that leads to added delay and loss of bandwidth efficiency.

- Frequency diversity: the signal is transmitted using several frequency channels. This method is not a plausible diversity approach for M2M systems. Because it is possible that an appropriate frequency for one particular device to device link may exhibit deep fades in another.

- Spatial diversity: the transmit signal is received at several antenna elements. These el-

ements should be sufficiently far from each other to guarantee low correlation between signals at antenna elements. This constraint make spatial diversity a less than desirable approach for M2M applications where the size of the antenna system is a crucial design parameter.

- Polarization diversity: orthogonal polarized components propagate differently in a wireless channel. The fading of signals with different polarization is statistically independent. Therefore, receiving two polarizations using a dual-polarized antenna, or three polarizations using a tripolar antenna, as we investigate in this dissertation, offers diversity without any need for a minimum distance between antenna elements.

Generally, there are two ways of exploiting signals from the multiple diversity branches namely selection diversity in which the "best" signal copy is selected, while the other copies are discarded, and combination diversity that combine all signals received from diverse branches. Diversity gain expresses the fact that it is unlikely that several antenna elements are in a fading dip simultaneously. Selection diversity can be implemented in two ways :

- Received-signal-strength-indication-driven-diversity: in this method, the RX selects the signal with the largest instantaneous power (or Received Signal Strength Indication, RSSI. This techniques needs N_r antenna elements, N_r RSSI sensors, and a N_r-to-1 multiplexer and one RF chain.

- Switched diversity: this approach is simpler to implement. Switched diversity just monitors the active diversity branch at one time and if this branch falls below a threshold, it switches to the next branch.

1.2.4 What is polarization?

An electromagnetic wave can be characterized by four features: frequency of the oscillation of the wave, direction of propagation, intensity of the wave, and its polarization. Among mentioned features, polarization is unique to electromagnetic waves and is not defined in other waves [22]. At a fixed point in space, the electric field of an electromagnetic wave outlines an ellipse, the polarization ellipse (Fig. 1.6), in a plane perpendicular to the propagation direction [23]. The

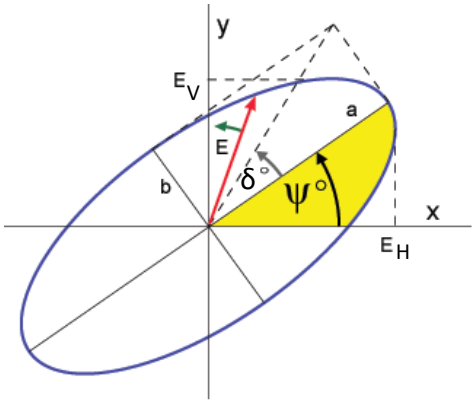

Figure 1.6: Polarization ellipse showing the orientation angle Ψ and ellipticity δ [2].

shape of the ellipse is dependent on the magnitudes and relative phase between the horizontal and vertical components of the electric field vectors. When the components are in phase, the polarization is linear ($\delta = 0$). In case of $\pi/2$ radians phase difference between orthogonal polarization components, the ellipse transforms to a circle which represents circular polarization. Polarization is described by time variations of the electric field vector such that the electric field vector variation in time and space for a wave traveling in $+z$ direction is

$$E(\vec{t}, z) = E_H cos(2\pi ft - kz)\hat{x} + E_V cos(2\pi ft - kz + \delta)\hat{y} \tag{8}$$

where, f is the frequency of the wave and k is the phase constant. E_H and E_V are the amplitude of horizontal and vertical polarized components of the electric field. δ defines phase difference between these horizontal and vertical components.

In an ideal environment (i.e., anechoic chamber), both the propagation direction and the polarization ellipse remain constant at each point in space, whereas in a multipath environment like inside a reverberation chamber, as shown in this dissertation, these two parameters change over time/frequency/space. There are different representations for describing polarization of a wave. The phasor representation of electric field is called the associated Jones' vector and contains all the information about the polarization of the wave. In general, an arbitrary plane wave that propagates in a direction orthogonal to the horizontal and vertical polarization components, has

the following Jones' vector [22].

$$\vec{E} = \begin{bmatrix} E_H \\ E_V e^{j\delta} \end{bmatrix} \tag{9}$$

where, E_H and E_V are horizontally and vertically polarized components of the electric field, respectively and δ defines phase difference between them. The state of polarization of an electromagnetic wave rotates as it goes through reflection, diffraction, or scattering in a wireless channel. This rotation can be described as [24]

$$\begin{bmatrix} E_H^r \\ E_V^r e^{j\delta^r} \end{bmatrix} = \begin{bmatrix} \gamma_{HH} & \gamma_{HV} \\ \gamma_{VH} & \gamma_{VV} \end{bmatrix} \begin{bmatrix} E_H^t \\ E_V^t e^{j\delta^t} \end{bmatrix} \tag{10}$$

where, E_H^t and E_V^t are the components of the wave before the interaction, E_H^r and E_V^r are the components of the wave after the interaction. δ^t and δ^r are phase difference between two polarization components before and after the interaction, respectively. The terms of matrix γ also contain the complex loss coefficients due to the interaction. Unlike single polarized channels that only one loss coefficient should be characterized, in a dual-polarized channel, all four elements of the matrix γ should be determined.

1.2.5 Wireless channel model

A major requirement in the design of any digital wireless system in terms of selecting modulation schemes, channel equalization techniques, and network concepts is the adequate understanding of the radio channel [25]. A wireless channel model is a tool to simulate certain aspects of what happens between transmitter and receiver without the need to actually implement the real wireless communication system. This helps us in better utilization of wireless resources. Creating a channel model can be described as a three step procedure. First, measurements must be collected. Then, the actual model will be designed and finally, the model should be validated using some predetermined metrics. Channel models are categorized as three main types [24]:

- Deterministic methods: These are exact channel models, where a specific environment is constructed and the field at every point in the space is computed. Ray-tracing model that uses very narrow beams in different directions is the most common deterministic

methods. In a basic ray-tracing algorithm, the main task is to determine the trajectory of a ray launched from a transmitting antenna. This procedure involves the calculation of the intersection of a ray with a surface or a ray with an edge segment using simple reflection, transmission and diffraction laws. The disadvantage of this method is the huge computation time for complex environments [26].

- Statistical channel models: In these models statistical properties of channels are modeled based on measurements and without requiring physical justifications. These methods require the environment to be statistically stationary. Though in this method disassociating antenna effects from channel effects is not possible, its mathematical simplicity has made this technique very popular for channel characterization. A good example of statistical channel model can be found in [27]. In this paper, a comprehensive statistical radio impulse channel model for factory and open plan buildings is presented. The statistical model is built based on measurements taken at 50 different locations within five different factory buildings. Small scale effects are accounted for by moving receiver on a 1 m track with step sizes of $\lambda/4$.

- Geometry-based stochastic channel models (GBSCM): These models are simplified ray-tracing approaches in which scatterers are specified by spatial distributions which are described using parameters that are extracted from experimental measurements. The main advantage of these models is their independence of antennas characteristics [3, 28, 29].

1.3 Research Objectives and Organization

The first two objectives of this dissertation are to provide a theoretical framework for depolarization in three dimensions and to prepare a tripolar antenna design that is suitable for M2M applications and that can mitigate severe fading in such channels. The third objective is to develop new dual-polarized channel models in a 3D space for wireless systems that are able to incorporate different polarization types. This dissertation is organized as seven chapters. Chapters 2-6 are presented as published or submitted for publication. Chapter 7 discusses the Conclusions and avenues for future work. Each Chapter's goal is summarized as follows.

- Though 2D polarization formalism has found its way in wireless communication and sensing, the new 3D definition has not received attention in wireless communication and so far the performance analysis of tripolar systems has been mostly through experiments. In Chapter 2, an analytical study of depolarization in three dimensions and also justification of employing 3D polarization diversity instead of traditional 2D approach for mitigating fading in cluttered environments are provided.

- In Chapter 3, the data taken in an environment, that can be a representative of a M2M communication channel, show that highly variable depolarization occurs across all three spatial dimensions and is dependent on small changes in frequency and space. These empirical results illustrate the use of a prototype tripolar antenna to mitigate the depolarization in three dimensions caused by such channels.

- The results obtained in Chapters 2 and 3 motivated development of tripolar antenna designs. In the first part of Chapter 4, antenna system geometries that can be cofabricated with the device's enclosure using 3D printing technologies are explored. The second part of this chapter concludes by presenting the efficacy of the fabricated tripolar antenna for mitigating fading in a highly-reflective, fading environment.

- Chapter 5 discusses the effectiveness of different types of polarization (linear, circular) in suppressing multipath effects in cluttered settings. In this chapter, a 3D dual-polarized geometrical channel model is proposed to evaluate circular and linear polarization in indoor channels. The second part of this chapter focuses on effects of implementing hybrid polarization diversity for mitigating deep fading in harsh multipath environments. Hybrid polarization diversity is achieved by choosing between four different polarizations of a simple low-cost omnidirectional antenna.

- Bandwidth shortage has motivated the exploration of the under-utilized millimeter wave (mm-wave) frequency spectrum for future broadband cellular communication networks. There is, however, little knowledge about mm-wave propagation in cluttered indoor environments. The first part of Chapter 6 discusses dual-polarized channel measurements at 28 GHz band inside an office. In the second part of this chapter, multipath effects at 60

GHz are characterized over small-scale movements using a finite-state Markov model.

- Conclusions and avenues for future work are summarized in Chapter 7.

2 Depolarization Evaluation Using Stokes Vector

Foreword

This chapter studies depolarization in three dimensions using a Stokes vector framework. First it introduces the well defined 2D Stokes vector and then discusses its insufficiency for description of polarization state of a signal in multipath conditions. Thereafter, the 3D generalized Stokes vector framework is provided as a suitable option for determining depolarization in such cases. Section 2.1 is the work as presented at the "2016 Wireless and Microwave Technology Conference" [30]. Section 2.2 presents the submitted paper to "2019 Progress In Electromagnetics Research (PIER) Letters". This letter builds on the conference paper by elaborating on analytical frameworks by which 2D and 3D depolarization are described using a spectral polarization matrix. Degree of polarization in 3D is decomposed into two polarization indices to quantitatively distinguish between 2D and and 3D depolarization.

2.1 Depolarization in three dimensions: theoretical formulations and empirical results

2.1.1 Abstract

Depolarization of wireless communication signals in two dimensions is a well studied phenomenon. However, with systems being deployed in ever more cluttered environments, this work herein illustrates that depolarization should be considered a three dimensional effect. The work presents analytical frameworks to study depolarization in three dimensions and empirical results illustrating its potentially significant impact[1].

2.1.2 Introduction

Point-to-point wireless communication systems are becoming evermore pervasive with the advent of machine-to-machine (M2M) and other Internet of Things (IoT) systems. This pervasiveness

[1]Golmohamadi, M. and Frolik, J.. 2016, April. Depolarization in three dimensions: theoretical formulations and empirical results. In Wireless and Microwave Technology Conference (WAMICON), 2016 IEEE 17th Annual (pp. 1-6). IEEE.

leads to systems being deployed in environments that are less than ideal for wireless communications. These include, for example, about and/or within industrial machinery or home appliances. Such environments can consist of a variety of surfaces that block and/or reflected the wireless signals thus introducing non line of sight (NLOS) and/or multipath conditions, respectively, and multipath can not only cause fading in a channel but also depolarize the transmitted signal [4]. A well-known approach to mitigating multipath is to leverage multiple 'branches' whose fading statistics are poorly correlated [5]. Branches can, for example, consist of utilizing multiple frequencies, antennas, or polarizations.

For M2M systems that involve multiple devices, potentially implemented as an ad hoc mesh network, coordinating multiple frequencies is not a tenable diversity approach, for it is possible that an appropriate frequency for one particular device to device link may exhibit deep fades in another. Employing multiple antennas (i.e., spatial diversity) requires elements to be located sufficiently far from each other ($\sim \lambda/2$) to guarantee decorrelation of fading effects. This constraint makes spatial diversity a less than desirable approach for applications where the size of the antenna system is a crucial design parameter.

Although polarization diversity in two dimensions has been long considered [8, 9], leveraging all three spatial dimensions has received limited attention [10]. For point-to-point systems with a line of sight (LOS), it is reasonable to state that there are only two relevant polarizations (e.g., linearly vertical and horizontal) which lie in a plane normal to the direction of propagation. However, in the presence of reflectors and retarders that eliminate a LOS component, an environment can lead to depolarization in a third dimension and thus, we contend and show herein, one should consider a 3D polarization space versus a 2D plane.

Recognizing depolarization effects in three dimensions, there has been some efforts in designing antennas to leverage the extra degree of freedom. For example, use of colocated antenna elements with three (one loop and two coplanar dipoles) and four elements (one loop and three mutually orthogonal dipoles) led to channel capacities greater than a single element antenna [31]. Tripolarized antennas have also been demonstrated to achieve channel capacities comparable to three spatially separated single polarized antennas in a MIMO system [32]. In addition, prior work has also studied extra degrees of freedom provided by the magnetic field components [10, 33, 34]. For example, the feasibility of hexapolarized antenna was introduced

in [10]. More recently, a hexapolarized antenna operating at 377 MHz was fabricated and its channel characteristics measured in a multipath setting [34].

Beyond the noted prior work, there has been little additional investigation of (de)polarization in three dimensional space [4]. For instance, and to the best of the authors' knowledge, there has been little empirical data illustrating this phenomenon. Thus one contribution of the work herein is to present such data. But first we provide analytical frameworks by which 3D depolarization can be studied.

2.1.3 3D Depolarization: Analytical Frameworks

In this section, we consider two approaches by which to frame the 3D depolarization problem. This first is to extend well-known 2D channel matrix results to three dimensions. The second, extends the Stokes vector to three dimensions. We will later use these two frameworks and empirical data to demonstrate the significance of considering the third polarization.

2.1.3.1 Channel matrix framework

For wireless communications, a channel state matrix can be used to represent how a signal propagates from a transmitter to a receiver. The channel for n transmit and m receive antennas can be represented by the following matrix with complex coefficients of the form [35]:

$$\mathbf{A}_{m,n} = \begin{bmatrix} a_{11} & a_{12} & a_{13} & \dots & a_{1n} \\ a_{21} & a_{22} & a_{23} & \dots & a_{2n} \\ \dots & \dots & \dots & \dots & \dots \\ a_{m1} & a_{m2} & a_{m3} & \dots & a_{mn} \end{bmatrix} \tag{11}$$

where a_{ij} represents the complex gain in the path from transmitter j to receiver i. The received electric field for when linearly polarized antennas (vertical and horizontal) are transmitting can be found from using a 2D channel matrix as follows ($\mathbf{A}_{2D}$ is the case where $m = 2, n = 2$):

$$\mathbf{E}_{RX} = \mathbf{A}_{2D}\mathbf{E}_{TX}, \tag{12}$$

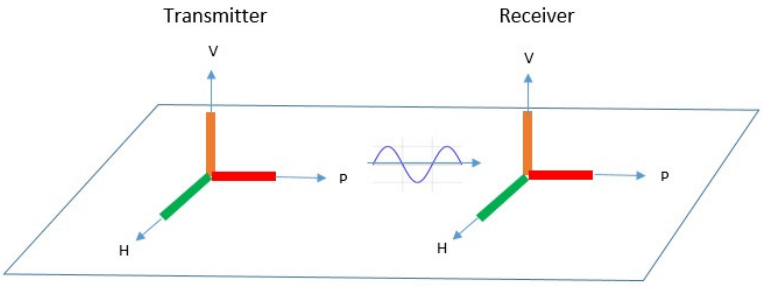

Figure 2.1: 3D linear polarization framework: vertical (V), horizontal (H), and parallel (P)

which we can write more explicitly as

$$\begin{bmatrix} E_{V_{RX}} \\ E_{H_{RX}} \end{bmatrix} = \begin{bmatrix} a_{VV} & a_{VH} \\ a_{HV} & a_{HH} \end{bmatrix} \begin{bmatrix} E_{V_{TX}} \\ E_{H_{TX}} \end{bmatrix}. \tag{13}$$

A_{2D} is the case where $m = 2, n = 2$.

For the three dimensional formulation, we extend the 2×2 channel matrix of Eq. (13) to the following 3×3 formulation by adding the third dimension 'P' that is orthogonal to both a linear vertical polarization (V) and a linear horizontal polarization (H) and that is nominally *parallel* with the LOS between a transmitter and a receiver (Fig. 2.1). The resulting formulation can be written as

$$\begin{bmatrix} E_{V_{RX}} \\ E_{H_{RX}} \\ E_{P_{RX}} \end{bmatrix} = \begin{bmatrix} a_{VV} & a_{VH} & a_{VP} \\ a_{HV} & a_{HH} & a_{HP} \\ a_{PV} & a_{PH} & a_{PP} \end{bmatrix} \begin{bmatrix} E_{V_{TX}} \\ E_{H_{TX}} \\ E_{P_{TX}} \end{bmatrix}, \tag{14}$$

or compactly as $\mathbf{E}_{RX} = \mathbf{A}_{3D}\mathbf{E}_{TX}$. In other work, this third dimension has been designated 'D' for *diagonal* [32], but there is no standardized notation to date.

2.1.3.2 Stokes parameter framework

The Stokes vectors provide a convenient framework of representing how an electromagnetic wave is affected by insertion of a reflector, polarizers, and retarders. They form a complete set which characterize any plane electromagnetic wave. We first consider 2D representation of Stoke vector which is appropriate when the electric field remains in a fixed plane. Stoke parameters can be

described as follows [36],

$$\mathbf{S}_{2D} = \begin{bmatrix} s_0 \\ s_1 \\ s_2 \\ s_3 \end{bmatrix} = \begin{bmatrix} \langle |E_V|^2 \rangle + \langle |E_H|^2 \rangle \\ \langle |E_V|^2 \rangle - \langle |E_H|^2 \rangle \\ \langle E_V E_H^* \rangle + \langle E_H E_V^* \rangle \\ -i(\langle E_V E_H^* \rangle - \langle E_H E_V^* \rangle) \end{bmatrix}. \tag{15}$$

The first parameter of Stokes vector, s_0, is the intensity of electromagnetic wave. The other three parameters, s_1, s_2, and s_3 describe the polarization state of the wave. As examples, for a given field intensity I, the Stokes vectors for linear vertical, horizontal, and 45° polarization are:

$$\mathbf{S}_V = \begin{bmatrix} I \\ I \\ 0 \\ 0 \end{bmatrix}, \ \mathbf{S}_H = \begin{bmatrix} I \\ -I \\ 0 \\ 0 \end{bmatrix} \ \& \ \mathbf{S}_{45^\circ} = \begin{bmatrix} I \\ 0 \\ I \\ 0 \end{bmatrix} \tag{16}$$

.

2D Stokes parameters can be geometrically represented in Poincare sphere. For example, pure linear polarizations lie on the equator of the sphere. Any inner point of the sphere refers to a partially polarized wave, and its origin represents unpolarized wave ($\mathbf{S}_{2D} = \Big[I, 0, 0, 0\Big]^T$) [37].

However, since the nature of wave propagation in presence of multipath or in near-field electromagnetic radiation is 3D, 2D framework is insufficient for modeling electromagnetic waves.

The generalized Stokes parameters in 3D have been defined as follows [38].

$$\mathbf{S}_{3D} = \begin{bmatrix} q_0 \\ q_1 \\ q_2 \\ q_3 \\ q_4 \\ q_5 \\ q_6 \\ q_7 \\ q_8 \end{bmatrix} = \begin{bmatrix} \langle|E_V|^2\rangle + \langle|E_H|^2\rangle + \langle|E_P|^2\rangle \\ \sqrt{3/2}(\langle E_V E_H^*\rangle + \langle E_H E_V^*\rangle) \\ \sqrt{3/2}(\langle E_V E_P^*\rangle + \langle E_P E_V^*\rangle) \\ i\sqrt{3/2}(\langle E_V E_H^*\rangle - \langle E_H E_V^*\rangle) \\ \sqrt{3/2}(\langle|E_V|^2\rangle - \langle|E_H|^2\rangle) \\ \sqrt{3/2}(\langle E_H E_P^*\rangle + \langle E_P E_H^*\rangle) \\ i\sqrt{3/2}(\langle E_V E_P^*\rangle - \langle E_P E_V^*\rangle) \\ i\sqrt{3/2}(\langle E_H E_P^*\rangle - \langle E_P E_H^*\rangle) \\ \sqrt{1/2}(\langle|E_V|^2\rangle + \langle|E_H|^2\rangle - 2\langle|E_P|^2\rangle) \end{bmatrix} \tag{17}$$

Unlike 2D representation where the Poincare sphere can be utilized, there is no geometrical representation for 3D Stokes parameters. However, some analogies can be made between 2D and 3D Stokes parameters. q_0, which is intensity of wave, is analogous to s_0 in 2D formalism. q_1 and q_3 act like s_2 and s_3, respectively. Furthermore, the pair of (q_2, q_6) and (q_5, q_7) can be compared to (s_2, s_3) in different plane coordinates. And also q_4 is analogous to s_1 [37].

The Stokes parameters of three linear polarizations we are considering for the three dimensional environment (V, H, and P) are found from Eq. (34) as:

$$\mathbf{S}_V^t = \left[I, 0, 0, 0, \sqrt{3/2}I, 0, 0, 0, \sqrt{1/2}I\right],$$
$$\mathbf{S}_H^t = \left[I, 0, 0, 0, -\sqrt{3/2}I, 0, 0, 0, 0, \sqrt{1/2}I\right]$$
$$\mathbf{S}_P^t = \left[I, 0, 0, 0, 0, 0, 0, 0, 0, -2\sqrt{1/2}I\right]$$

2.1.4 Experimental Results

We now present empirical data illustrating the depolarization effect in three dimensions. Two different scenarios are considered (an idealized case and a multipath case) along with analyses of the measurements.

2.1.4.1 Methodology

S_{21} measurements were conducted, using a vector network analyzer (Agilent 8722ES), between two linearly-polarized, monopole antennas. The antennas were placed approximately 1 m apart in one of two compact chambers. The first chamber presented an anechoic (i.e., idealized) environment. The second chamber had highly reflected walls and contained a variety of reflective obstructions. As illustrated in Fig. 2.1, the two antennas were aligned to one of three orientations: (1) vertical (V), (2) horizontally orthogonal to wave propagation (H), and (3) coinciding and parallel to the transmitter to receiver propagation direction (P). Each antenna was oriented to one of these three positions thus yielding nine S_{21} measurements in total: $VV, HV, PV, HH, VH, PH, VP, HP$, and PP.

For each of the nine polarization configuration, S_{21} sweeps were made between 2.40 GHz and 2.48 GHz (bandwidth of 80 MHz). The S_{21} measurements were used directly to create a 3×3 channel matrix, $\mathbf{A}_{3D}$ described in Eq. (14), in which each element represents the complex gain between transmitter and receiver. For instance, a_{VH} is path gain between port H of transmitter and port V of receiver.

2.1.4.2 Idealized case

We first illustrate our test methodology with an idealized case where the testing was conducted in a compact anechoic chamber (Fig. 2.2). As would be expected, VV and HH copolarization (copol) performance exhibits nearly flat behavior in this environment. Also, as expected, the cross polarization discrimination (XPD) between orthogonal polarizations is high. For illustration purposes, Fig. 2.3 shows the copol measurement (VV) and the XPD measurements (HV and PV) for case when the transmit antenna was oriented vertically. We see from this data the XPD exceeds 15 dB as would be expected for such an idealized environment.

For this environment, we would also expect little to no multipath and thus the propagation is effectively modeled in just two dimensions (i.e., planar propagation). Our data for when the transmit antenna was oriented in the P (parallel) direction confirms this expectation (Fig. 2.4). Here both the copol (PP) and crosspol (VP and HP) measurements are comparable and significantly lower (> 10 dB) than the VV or HH copol measurements. The lack of multipath in

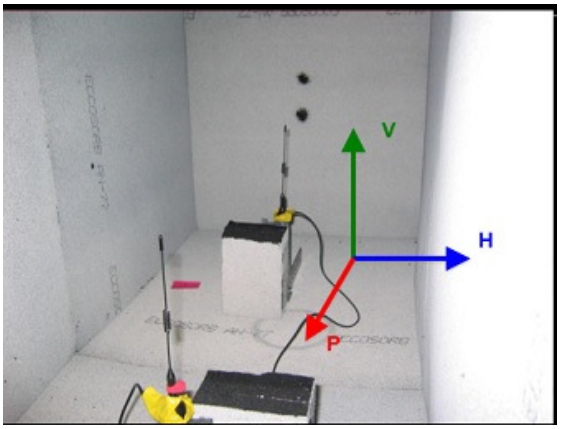

Figure 2.2: Measurement set-up for ideal case (anechoic chamber)

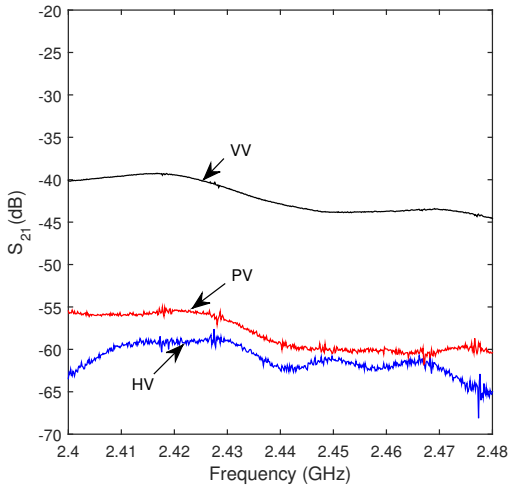

Figure 2.3: Copol and crosspol S_{21} in dB for V polarized transmit antenna (anechoic chamber)

this scenario results in little signal received when the transmission is in the P direction and thus a 2D formulation is more than adequate for this case.

To illustrate the idealized case further, we utilize our data to determine the optimal orientation for the receive antenna for a vertical transmit antenna. Depolarization can occur both in azimuth (i.e., toward the H polarization) or in elevation (i.e., toward the P direction). The depolarization is determined directly from the S_{21} measurements as follows.

$$\theta_{az} = tan^{-1}(S_{HV}/S_{VV}) \;\&\; \theta_{el} = tan^{-1}(S_{PV}/S_{VV}) \tag{18}$$

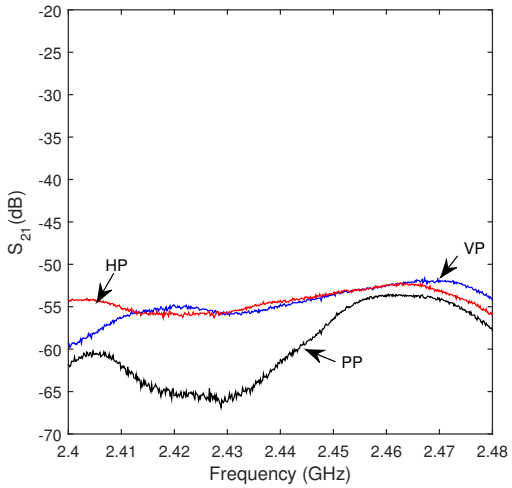

Figure 2.4: S_{21} in dB for P polarized transmit antenna (anechoic chamber)

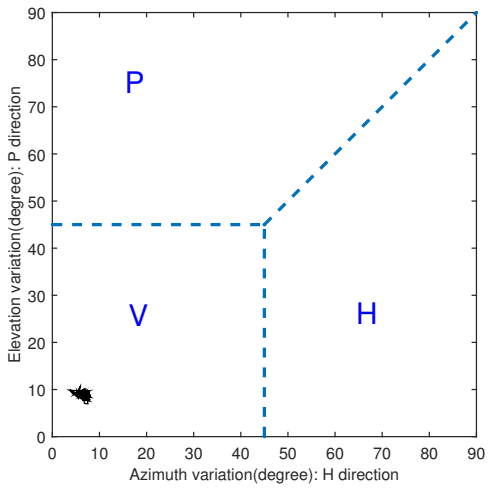

Figure 2.5: Depolarization of vertically transmitted signal in azimuth and elevation (idealized chamber)

Recall that our S_{21} measurements are a function of frequency (2.40-2.48 GHz). Thus we may see variation over frequency in the amount of rotation in azimuth and elevation directions as shown in Fig. 2.5.

In an idealized chamber, the electric field does not experience significant depolarization and its orientation almost remains unchanged for different frequencies. When the transmitter is aligned vertically, the best receive antenna angle, relative to vertical, is only off $3° - 8°$ in

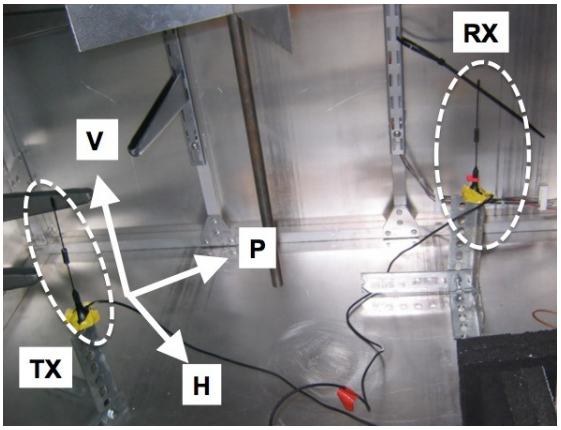

Figure 2.6: Measurement set-up for multipath case (compact reverberation chamber)

azimuth and $7^\circ - 10^\circ$ in elevation. Similar lack of depolarization is seen when the transmit antenna is set to linear horizontal. So, as would be expected for an idealized environment, the best nominal orientation for receiver antenna is to be copolarized with the transmitter regardless of transmitter polarization.

2.1.4.3 Multipath case

The second scenario is one where channel measurements were made inside a highly reflective and cluttered environment (Fig. 2.6) which we contend emulates the environment that may be seen by many M2M/IoT systems.

Fig. 2.7 shows copolar and crosspolar S_{21} data when transmitter is vertically polarized. In this test scenario, the data are (1) no longer clearly distinguished in terms of mean S_{21} measurements and (2) all measurements are highly variable illustrating significant multipath fading. Thus, this environment not only introduces multipath but depolarizes the transmitted wave in three dimensional space, which is noted by the significant S_{PV} data. We see the three dimensional effect distinctly in Fig. 2.8 for the case where the transmit antenna is P polarized. This configuration exhibits measurement results not unlike that seen in Fig. 2.7, for vertical transmit polarization, indicating that transmitting in the P direction is no worse/better than choosing to do so in the V or H directions.

As in Fig. 2.5, we now present in Fig. 2.9 the depolarization noted over frequency if the transmit antenna is oriented in the vertical position. For this highly reflective environment, it is

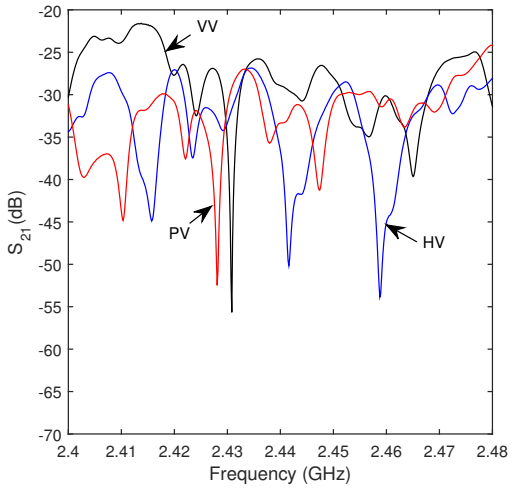

Figure 2.7: Copol and crosspol S_{21} in dB for V polarized transmit antenna (cluttered chamber)

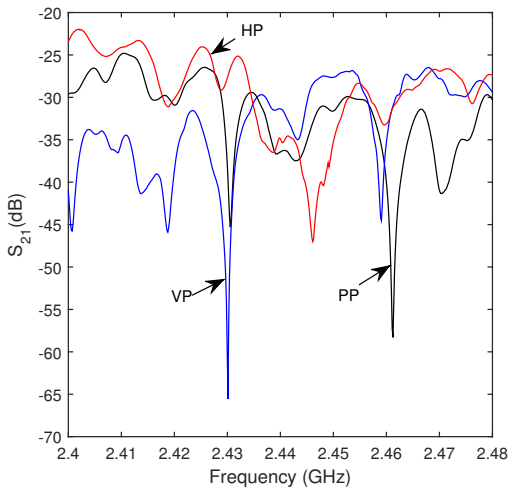

Figure 2.8: S_{21} in dB for P polarized transmit antenna (cluttered chamber)

difficult to argue what is the 'right' orientation in three dimensions to set the receive antennas as that is clearly a function of frequency. This result should motivate the pursuit of antennas that are designed to operate in three dimensions as opposed to more common planar designs.

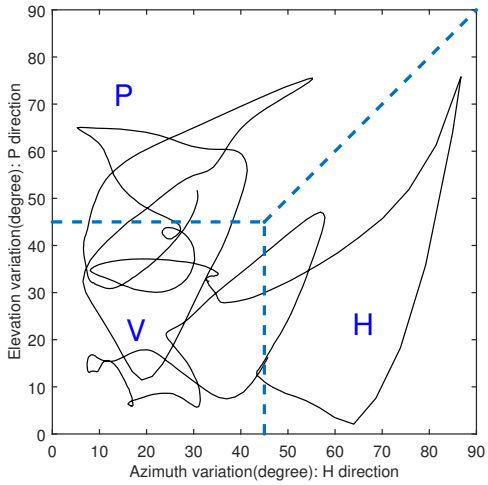

Figure 2.9: Depolarization of vertically transmitted signal in azimuth and elevation (cluttered chamber)

2.1.5 Summary Metrics

In this section we utilize our prior formulations of Section II to provide summary metrics for depolarization. In particular, we consider cross-polarization discrimination and degree of polarization. These metrics allow us to provide global performance metrics for the two environments in which our testing was conducted.

2.1.5.1 XPD

Cross-polarization discriminator (XPD) is defined as the ratio of the average power received in the copolarized channel to the average power received in the crosspolarized channels [39, 40]. XPD has been formalized in a 2D framework, using the channel matrix Eq. (13), as follows.

$$XPD_V = \frac{\langle a_{VV} a_{VV}^* \rangle}{\langle a_{HV} a_{HV}^* \rangle} \tag{19}$$

$$XPD_H = \frac{\langle a_{HH} a_{HH}^* \rangle}{\langle a_{VH} a_{VH}^* \rangle}$$

Where, for our data, $\langle ... \rangle$ denotes the average over frequencies 2.40 GHz - 2.48 GHz. However, to the best of our knowledge, XPD has not been presented in 3D framework. As such, we extend

Table 2.1: Cross polar discrimination in 3D framework

Case	XPD_V	XPD_H	XPD_P
Idealized	17.15 dB	15.1 dB	-3.46 dB
Multipath	4.34 dB	2.94 dB	-1.76 dB

Eq. (48), using our 3D channel matrix Eq. (14), as follows.

$$XPD_V = \frac{\sqrt{2}\langle a_{VV} a_{VV}^* \rangle}{\sqrt{\langle a_{HV} a_{HV}^* \rangle^2 + \langle a_{PV} a_{PV}^* \rangle^2}} \tag{20}$$

$$XPD_H = \frac{\sqrt{2}\langle a_{HH} a_{HH}^* \rangle}{\sqrt{\langle a_{VH} a_{VH}^* \rangle^2 + \langle a_{PH} a_{PH}^* \rangle^2}}$$

$$XPD_P = \frac{\sqrt{2}\langle a_{PP} a_{PP}^* \rangle}{\sqrt{\langle a_{VP} a_{VP}^* \rangle^2 + \langle a_{HP} a_{HP}^* \rangle^2}}$$

Note that the purpose of the $\sqrt{2}$ factor in the numerator is to normalize the sum of the two denominator components.

Lower cross-polar discrimination indicates more depolarization in a propagation environment. A multi-polarized antenna can provide maximum diversity when copolar and crosspolar branches provide same power at the receiver (i.e., when $XPD = 0$ dB) [41]. Large values of XPD in the idealized chamber is an indicator of dominance of co-polar components and shows that a single copolar channel will provide the same performance as a multi-polarized channel. But low XPD in the multipath chamber demonstrates a good reason to use multi-polarized antennas in such environments.

We can see from Table 5.4 that there is low XPD in all three directions for the multipath channel, thus indicating that all three polarizations can be utilized effectively to increase system capacity. We also note that XPD_P is low for the idealized case but recall from Fig. 2.4 that S_{PP} was also very low and thus it is unlikely one can leverage effectively this third branch.

2.1.5.2 Summary of Results: Degree of polarization

To evaluate the depolarization in an environment quantitatively, the degree of polarization (DOP) metric can be used. A fully polarized wave has a $DOP = 1$ and a completely unpolarized wave has $DOP = 0$. Using the Stokes parameters of Eq. (28), DOP is formalized in

Table 2.2: Degree of polarization

Framework	Idealized	Multipath
2D (m_2)	0.9998	0.88
3D (m_3)	0.99	0.43

a 2D framework by using Eq. (30) of [42].

$$m_2 = \frac{\sqrt{s_1^2 + s_2^2 + s_3^2}}{s_0} \tag{21}$$

Degree of polarization in 3D framework can be calculated by using the elements of Eq. (34), i.e., $\mathbf{S}_{3D}$ and using Eq. (21) of [42].

$$m_3 = \frac{\sqrt{\sum_{i=1}^{8} q_i^2}}{\sqrt{2} q_0} \tag{22}$$

From measured S_{21} parameters, the channel matrix ($\mathbf{A}_{2D}$, $\mathbf{A}_{3D}$) are composed. The received electric field, E_{RX}, in 2D and 3D is calculated from Eq. (12) and Eq. (14), respectively, for each of the frequencies measured. Then a 3D polarization matrix, Φ_3, leveraging prior formulations [43], is developed.

$$\Phi_3 = \begin{bmatrix} \langle E_{H_{RX}} E_{H_{RX}}^* \rangle & \langle E_{H_{RX}} E_{V_{RX}}^* \rangle & \langle E_{H_{RX}} E_{P_{RX}}^* \rangle \\ \langle E_{V_{RX}} E_{H_{RX}}^* \rangle & \langle E_{V_{RX}} E_{V_{RX}}^* \rangle & \langle E_{V_{RX}} E_{P_{RX}}^* \rangle \\ \langle E_{P_{RX}} E_{H_{RX}}^* \rangle & \langle E_{P_{RX}} E_{V_{RX}}^* \rangle & \langle E_{P_{RX}} E_{P_{RX}}^* \rangle \end{bmatrix} \tag{23}$$

Where, again, brackets denote averaging over frequency. Using the elements of Φ_3 matrix, Stokes parameters are computed for Eq. (28) and Eq. (34). Results of the DOP based on our measured data are presented in Table 2.2.

In an idealized case DOP shows the same value for both 2D and 3D framework. Having degree of polarization close to 1 in idealized chamber indicates that received wave is almost fully polarized. On the other hand, results of cluttered chamber shows completely different DOP values for two frameworks which indicates inaccuracy of considering its polarization state in a 2D basis. In this case, the transmitted signal has converted from a fully polarized at the transmitter to a partially polarized wave with $DOP = 0.43$ at the receiver. This index can be

applied for evaluating whether it is reasonable to use 3D antenna in an environment by knowing the fact that 3D antenna imposes cost increase and power division among branches.

2.1.6 Conclusion

In this work, we present analytical frameworks to study depolarization in three dimensions. We apply these frameworks to channel data collected in multipath environments and illustrate that commonly utilized two dimensional formulations do not sufficiently capture the effects of depolarization.

Work on the topic of 3D depolarization is limited but with the advent of M2M and other IoT systems, many deployed as mesh networks in highly complex environments, we contend that further exploration of this topic is warranted. Specifically, we expect that additional channel characterization and modeling will be conducted and new tripolar antenna designs to be developed.

2.2 A 3D Stokes Framework for Wireless Depolarized Channels

2.2.1 Abstract

In severe multipath channels, depolarization of wireless signals has been shown to be a three dimensional effect. This work herein presents and applies a 3D Stokes vector framework for such depolarization. Empirical data is used to illustrate the capabilities of this framework (specifically, polarization purity indices and direction of propagation) to describe depolarization behavior for three different wireless channels[2].

2.2.2 Introduction

Wireless communication is becoming evermore pervasive with the advent of machine-to-machine (M2M) and other Internet of Things (IoT) systems. This pervasiveness leads to systems being deployed in environments that are less than ideal for wireless communications (e.g., about and/or within industrial machinery). Such environments can consist of a variety of surfaces that block and/or reflect the wireless signals thus introducing non-line-of-sight (NLOS) and/or multipath conditions, respectively. These conditions can cause not only fading in a channel but also depolarize the transmitted signal [4]. For point-to-point wireless communication systems with a strong line of sight (LOS), it is reasonable to state that there are only two relevant polarizations (e.g., vertical/horizontal linear or left/right hand circular polarization) which lie in the 2D plane normal to the direction of propagation. However, cluttered environments can lead to depolarization in a third dimension [10]. Thus, we contend and show herein, one should consider a 3D polarization framework versus a 2D one.

Electromagnetic wave polarization characterization in two dimensions is well-studied. However, the description of electromagnetic waves in three dimensions, where in general there is no specific propagation direction, is still an open question which needs careful consideration [44,45]. A well-defined polarization model will build a basis for understanding the input-to-output polarization behavior in wireless channels. Cross-polarization discrimination (XPD) has been used for polarization characterization [40], but this metric is not capable of fully interpreting po-

[2]Golmohamadi, M.and Frolik, J.. Submitted on January 20, 2019. A 3D Stokes Framework for Wireless Depolarized Channels. Progress In Electromagnetics Research (PIER) Letters.

larization properties of electromagnetic waves. Thus, in this work we consider a Stokes vector framework. A 2D Stokes vector framework has been used to model polarization behavior in multipath channels before [46], but employing a 3D framework has received little attention. The 3D framework was been applied for analyzing propagation within reverberation chambers [47]. Herein, we extend this initial contribution by characterizing frequency-dependant polarization effects and the propagation direction in 3D and apply this framework to empirical data.

In this paper, we present, in Section 2.2.3, analytical frameworks by which 2D and 3D depolarization are described using a spectral polarization matrix. Further, we present and analyze empirical data, in Section 2.2.4, for three different environments finding their polarization indices and also their variations of propagation direction. The contributions of this work are summarized in Section 2.2.5.

2.2.3 Polarization framework

In this section, we review the 2D polarization framework and then extend it to the third dimension. At a fixed point in space, the electric field of an electromagnetic wave outlines a polarization ellipse perpendicular to the propagation direction. In an ideal environment (i.e., anechoic chamber), the polarization ellipse remains in a fixed plane and maintains its shape, whereas in a multipath environment not only the shape of polarization ellipse changes but also its plane and consequently direction of propagation vary over time/frequency/space. In the latter case, as our data will show, a 2D representation is no longer sufficient.

2.2.3.1 2D Framework

A 2D coherency matrix, or polarization matrix, contains all information about autocorrelation and cross-correlation of the electric field components that are assumed to be contained in the x, y plane.

In this work, we consider the matrix elements in the space-frequency domain and call it the *spectral polarization matrix* which can be written as [48]

$$\Phi_{2D} = \begin{bmatrix} \langle E_x(r,f)E_x(r,f)^* \rangle & \langle E_x(r,f)\langle E_y(r,f)^* \rangle \\ \langle E_y(r,f)E_x^*(r,f) \rangle & \langle E_y(r,f)E_y(r,f)^* \rangle \end{bmatrix} \tag{24}$$

where, E_x and E_y are orthogonal components of the electric field vector at frequency f and position r and the asterisk denotes complex conjugation. The operator $\langle\ \rangle$ indicates that averaging of the signal has to be performed over the ensemble that characterizes the statistical properties of the field. Henceforth, we omit the explicit dependence on r and f. The spectral polarization matrix is non-negative definite Hermitian and consequently it is diagonalizable.

Any 2×2 diagonal representation of the spectral polarization matrix can be written as the sum of fully polarized $\rho_p = diag\{1, 0\}$ and completely unpolarized $\rho_{2u} = \frac{1}{2}diag\{1, 1\}$ matrices [49], that is

$$\hat{\Phi}_{2D} = (\lambda_1 - \lambda_2)\rho_p + 2\lambda_2\rho_{2u} \tag{25}$$

where, λ_1 and λ_2 are eigenvalues of both matrix Φ_{2D} and matrix $\hat{\Phi}_{2D}$. The degree of polarization in a 2D framework, P, is a metric to measure depolarization extent in an environment and is defined as the ratio of the intensity of the fully polarized part of the field to the total intensity of the field [44]. P can also be obtained from Stokes parameters that will be described shortly.

$$P = \frac{Tr((\lambda_1 - \lambda_2)\rho_p))}{Tr(\hat{\Phi}_{2D})} = \frac{\lambda_1 - \lambda_2}{\lambda_1 + \lambda_2} = \frac{\sqrt{\sum_{i=1}^{3}\langle s_i\rangle^2}}{\langle s_0\rangle} \tag{26}$$

where, Tr denotes the trace operation. Furthermore, the 2×2 identity matrix (σ_0) and the three Pauli spin matrices ($\sigma_1, \sigma_2, \sigma_3$) form a basis in which the spectral polarization matrix can be expanded as follows [50].

$$\Phi_{2D} = \frac{1}{2}\sum_{j=0}^{3}\langle s_j\rangle\sigma_j \tag{27}$$

In this expansion, the coefficients, s_j, are the Stokes parameters. These parameters provide a convenient framework of representing polarization state of a wave and form a complete set that characterize any fixed-plane electromagnetic wave. The 2D Stokes vector, $\mathbf{S}_{2D}$, is defined as follows [37],

$$\mathbf{S}_{2D} = \begin{bmatrix} s_0 \\ s_1 \\ s_2 \\ s_3 \end{bmatrix} = \begin{bmatrix} |E_x|^2 + |E_y|^2 \\ |E_x|^2 - |E_y|^2 \\ E_xE_y^* + E_yE_x^* \\ -i(E_xE_y^* - E_yE_x^*) \end{bmatrix}. \tag{28}$$

The first parameter of Stokes vector, s_0, is the intensity of the electromagnetic wave. The other three parameters, s_1, s_2, and s_3 describe the polarization state of the wave.

2D Stokes parameters can be geometrically represented in Poincare sphere. For example, pure linear polarizations lie on the equator of the sphere, where vertical and horizontal polarizations are on diametrically opposite sides of the sphere. Any inner point of the sphere corresponds to a partially polarized wave. The origin represents a completely unpolarized wave that has the following characteristics: $\mathbf{S}_{2D} = \Big[I, 0, 0, 0\Big]]^T$ (where I is the intensity of the field) and $P = 0$ (i.e., λ_1=λ_2).

2.2.3.2 3D Framework

In the presence of severe multipath, the polarization state of electromagnetic waves can not be fully realized within a 2D framework (as we demonstrate in Section 3). Therefore we now present the 3D spectral polarization matrix to describe wireless depolarization more generally [42].

$$\Phi_{3D} = \begin{bmatrix} \langle E_x E_x^* \rangle & \langle E_x E_y^* \rangle & \langle E_x E_z^* \rangle \\ \langle E_y E_x^* \rangle & \langle E_y E_y^* \rangle & \langle E_y E_z^* \rangle \\ \langle E_z E_x^* \rangle & \langle E_z E_y^* \rangle & \langle E_z E_z^* \rangle \end{bmatrix} \tag{29}$$

where the electric field vector has three orthogonal components along x, y, z axes. Unlike the 2D framework, Φ_{3D} cannot be described as the sum of only two components of a fully polarized and a fully unpolarized wave, as we had in Eq. (2). However, prior work [44] has shown that the diagonal representation of Φ_{3D} can be decomposed into three parts instead. Namely, fully polarized component $\rho_p = diag\{1, 0, 0\}$, fully 2D unpolarized $\rho_{2u} = \frac{1}{2} diag\{1, 1, 0\}$ and fully 3D unpolarized components $\rho_{3u} = \frac{1}{3} diag\{1, 1, 1\}$.

The diagonal representation of the 3D spectral polarization matrix can be presented as

$$\hat{\Phi}_{3D} = (\lambda_1 - \lambda_2)\rho_p + 2(\lambda_2 - \lambda_3)\rho_{2u} + 3\lambda_3\rho_{3u} \tag{30}$$

where, λ_1, λ_2 and λ_3 are eigenvalues of the 3D spectral polarization matrix, Φ_{3D}. Subsequent work [23] proposed two polarization indices, P_1 and P_2, such that P_1 defines stability of polarization ellipse and P_2 represents stability of propagation direction or stability of polarization

plane. P_1 is the ratio of the intensity of the fully polarized part of the field to the total intensity and P_2 is the ratio of components that have a fixed propagation direction (fully polarized and 2D unpolarized parts) to the total density of the field

$$P_1 = \frac{Tr((\lambda_1 - \lambda_2)\rho_p)}{Tr(\hat{\Phi}_{3D})} = \frac{\lambda_1 - \lambda_2}{\lambda_1 + \lambda_2 + \lambda_3} \tag{31}$$

$$P_2 = \frac{Tr((\lambda_1 - \lambda_2)\rho_p + (\lambda_2 - \lambda_3)\rho_{2u})}{Tr(\hat{\Phi}_{3D})} = \frac{\lambda_1 + \lambda_2 - 2\lambda_3}{\lambda_1 + \lambda_2 + \lambda_3} \tag{32}$$

In the 3D framework, the 3×3 identity matrix (ω_0) and eight Gell-Mann matrices ($\omega_1 ... \omega_8$) form a basis for the 3D spectral polarization matrix such that [37]

$$\Phi_{3D} = \frac{1}{3}\sum_{j=0}^{8}\langle\Lambda_j\rangle\omega_j \tag{33}$$

where, the nine real coefficients Λ_j are the generalized Stokes parameters of the 3D Stokes vector ($\mathbf{S}_{3D}$) [37]

$$\mathbf{S}_{3D} = \begin{bmatrix} \Lambda_0 \\ \Lambda_1 \\ \Lambda_2 \\ \Lambda_3 \\ \Lambda_4 \\ \Lambda_5 \\ \Lambda_6 \\ \Lambda_7 \\ \Lambda_8 \end{bmatrix} = \begin{bmatrix} |E_x|^2 + |E_y|^2 + |E_z|^2 \\ 3/2(E_x E_y^* + E_y E_x^*) \\ i3/2(E_x E_y^* - E_y E_x^*) \\ 3/2(|E_x|^2 - |E_y|^2) \\ 3/2(E_x E_z^* + E_z E_x^*) \\ i3/2(E_x E_z^* - E_z E_x^*) \\ 3/2(E_y E_z^* + E_z E_y^*) \\ i3/2(E_y E_z^* - E_z E_y^*) \\ \sqrt{3/4}(|E_x|^2 + |E_y|^2 - 2|E_z|^2) \end{bmatrix} \tag{34}$$

Some analogies can be made between 2D and 3D Stokes parameters. Λ_0, which is the intensity of the wave, is analogous to s_0 in the 2D framework. Λ_1, Λ_2, and Λ_3 in the 3D formulation are analogous to s_2, s_3, and s_1, respectively, in 2D. Furthermore, the pair of (Λ_4, Λ_5) and (Λ_6, Λ_7) can be compared to (s_2, s_3) in different plane coordinates. Furthermore, it has been shown that the direction of propagation ($\mathbf{V}$) can be defined from 3D Stokes parameters as follows [48]

$$\mathbf{V} = (-\Lambda_7, \Lambda_5, \Lambda_2),\ \phi = \arctan\frac{\Lambda_5}{-\Lambda_7},\ \theta = \arccos\frac{\Lambda_2}{|\mathbf{V}|} \tag{35}$$

from which we find the azimuth (ϕ) and elevation (θ) angles of the vector $\mathbf{V}$ and will apply them to our empirical cases presented in Section 3. The generalized degree of polarization in 3D framework, P_3, is dependent on two purity indices, P_1 and P_2, and can be calculated from 3D Stokes parameters [23].

$$P_3 = \frac{\sqrt{\sum_{i=1}^{8}\langle\Lambda_i\rangle^2}}{\sqrt{3}\langle\Lambda_0\rangle} = \sqrt{\frac{1}{4}(3P_1^2 + P_2^2)} \tag{36}$$

The value of P_3 for a fully polarized wave is 1 and for a 2D unpolarized wave, which has a well-defined propagation direction, is equal to 0.5. P_3 is 0 for a wave with completely random direction of propagation.

2.2.4 Experimental Results

Leveraging the formulation presented in Section 2.2.3, we now characterize the three distinct environments using polarization indices and arrival directions obtained from the 3D Stokes framework. To the best of the authors' knowledge, applying this 3D framework to data collected over frequency and space and to compare/contrast wireless environments has not been presented to date.

2.2.4.1 Methodology

The three surrogate environments represented an ideal (no multipath) environment, an office setting, and a highly reflective factory setting. To emulate an ideal setting, the testing was conducted in a compact anechoic chamber. The second environment was a non-line-of-sight condition within a lab. A compact (0.9 $m\times$ 0.9 $m\times$ 0.3 m) reverberation chamber was utilized to create the highly reflective scenario. A vector network analyzer was used to measure S_{21} (i.e., path loss) between the a vertically polarized transmit antenna and one orthogonal element of the receive array having three mutually orthogonal elements. S_{21} measurements were made at 551 frequencies between 2.40 GHz and 2.48 GHz. To emulate the random placement of the transmitting device, the transmit antenna was mounted on a linear track that allowed positioning

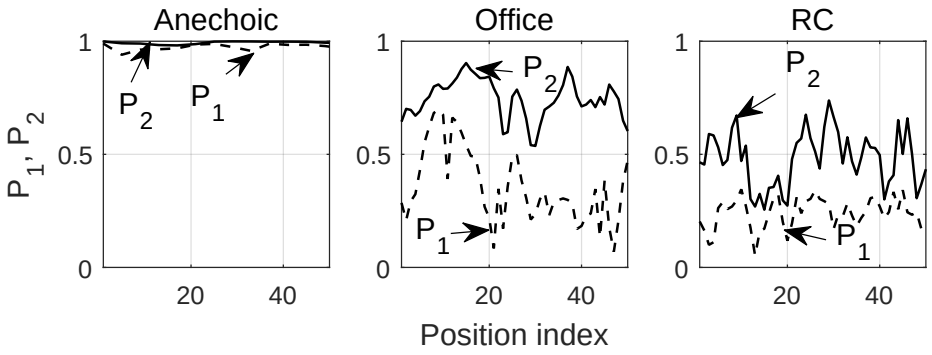

Figure 2.10: Polarization indices for the three demonstration environments. Left: Ideal surrogate. Center: Office surrogate. Right: Factory surrogate, reverberation chamber (RC).

Table 2.3: Degree of polarization

Framework	$mean(P_1)$	$mean(P_2)$	$mean(P_3)$
Anechoic	0.97	0.99	0.97
Office	0.36	0.74	0.49
RC	0.24	0.48	0.40

to one of 50 repeatable locations in 1 *cm* (i.e., $< \lambda/10$) increments.

2.2.4.2 Summary of Results

To obtain the results presented herein, we created spectral polarization matrices for each of the 50 locations by averaging over the 551 S_{21} measurements. Using this approach we find clear distinctions between the resulting parameters for the three different environments.

Fig. 2.10 shows the two purity indices, P_1 and P_2, calculated along 50 positions in the three environments. We clearly see the non-ideal environments depolarize the signal. Significantly, P_2 is much less than unity indicating that the depolarization is indeed three dimensional. The mean value of purity indices over 50 positions and generalized degree of polarization are presented in Table 2.2. In the anechoic chamber where there is no multipath components, the shape and plane of polarization ellipse remains constant over frequency variations and resulting in values very close to 1 for P_1, P_2, and P_3 parameters. In the reverberation, by contrast, P_1 very low indication the polarization ellipse changes significantly over frequency. Furthermore, P_2 is very low, an indication that plane of polarization rotates randomly along frequency. In addition, P_3

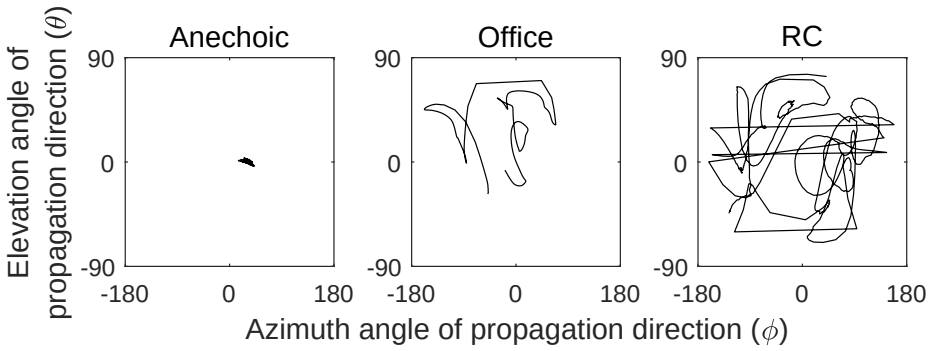

Figure 2.11: Azimuth and elevation angles of direction of propagation over frequency band of 2.40-2.48 GHz at one position.

is less than 0.5 (the one obtained for fully 2D unpolarized wave) that again confirms 3D nature of electromagnetic wave propagation in the chamber. The indices for the office indicate this is the intermediate case. In this scenario, on average, 26% $(1 - P_2)$ of the total intensity of the wave behaves completely randomly along frequency and is spread uniformly in 3D sphere. This percentage is attributed to the part of the 3D polarization matrix with equal eigenvalues.

The direction of propagation was calculated from Stokes parameters, using equation Eq. (35), for the measured frequencies in the band from 2.40 to 2.48 GHz. The results are presented Fig. 2.11. Since there is little depolarization in the anechoic chamber, the received direction is in original transmitted plane and the depolarization angle is approximately zero. In addition, as direction of propagation is almost fixed over the frequency, this confirms the result presented for $P_2 \approx 1$ in Table 2.3. However, in the office setup, the rotation of polarization plane along frequency band is evident. This rotation becomes even more prominent in reverberation chamber which indicates that this environment is more frequency-dependent than the office, as the data in Table 2.3 confirms. The rotations in the latter two cases is an indicator that the receiver's polarization should include all three planes in order to compensate for such depolarization effects. Recently, tripolar antennas have been developed in order to mitigate such severe multipath and depolarized channels [31, 51].

2.2.5 Conclusion

In this work, we presented a Stokes vector-based analytical framework to study depolarization in three dimensions. We applied this framework to empirical data in order to compare and contrast depolarization seen in three distinct environments. For environments with significant multipath, our calculated parameters show that depolarization is indeed a three dimensional effect. As wireless IoT systems become more pervasive and are deployed in evermore cluttered environments, these results can help determine if antenna systems that are tripolar are warranted. If so, then employing 3D polarization diversity in these scenarios would considerably improve link reliability as compared to the traditional dual polarization, 2D diversity approaches.

3 On Random and Multidimensional Channel Effects in Cluttered Environments

Foreword

This chapter is presented as published in "2017 IEEE Antennas and Wireless Propagation Letters" [12]. In this work, several experiments are conducted to investigate depolarization in three dimensions. The results show that polarization states of the received signals are highly variable and dependent on very small changes in frequency and placement. These random behavior of the depolarization prove that employing tripolar antennas in cluttered settings can enhance link reliability significantly, even if the environment is almost static and antenna's positions change minimally.

3.1 Abstract

Machine-to-machine (M2M) devices have the potential to be placed in environments that are less than ideal for wireless propagation, such as factory floors or within metallic enclosures. In this work, we illustrate that such environments not only produce the expected multipath but can also depolarize the signal across all three spatial dimensions. Furthermore, we show that these effects are multidimensional in that they are highly sensitive to extremely small changes in user placement and frequency of operation. That is, these channels exhibit randomness based on a user's action. These effects motivate new channel characterization approaches and metrics along with the development of tripolar antenna designs. The work concludes by presenting the efficacy of such a prototype antenna [3].

3.2 Introduction

Machine-to-machine (M2M) systems are those envisioned to not only report aggregated data to an end user but to also exchange data among devices to better and autonomously operate a larger system. For example, a M2M system may monitor and/or manage large machinery on a factory

[3] Frolik, J. and Golmohamadi, M.. 2017. On Random and Multidimensional Channel Effects in Cluttered Environments. IEEE Antennas and Wireless Propagation Letters, 16, pp.1863-1866.

floor, coordinate appliance activity throughout a home to reduce peak power loads, or track locations of shipping containers at docks. Given this breadth of potential M2M applications, it is clear that the environments in which they will be deployed can vary greatly in terms of wireless propagation conditions (multipath, line-of-sight (LoS), and non-LoS). Furthermore, as we illustrate herein, these effects, which include severe frequency-selective and depolarization effects in three dimensions, will be highly dependent on the placement of the device in the environment. This dependency, on what may be considered user-caused randomness, motivates this study.

For M2M systems to be low cost and easily deployed, there will likely be little prior knowledge about the propagation environment or control over device placement thus suggesting a strong need for the device to adapt to channel randomness. In this work, we provide examples of the aforementioned channel effects. For example, we show that these channels can take on characteristics that are statistically more severe than the worst-case assumed for mobile communications. Furthermore, we illustrate the use of a prototype tripolar antenna to mitigate the depolarization in three dimensions caused by such channels. Recognition of these severe effects and utilization of new channel analysis methods, we contend, will allow M2M designers to create more reliable networks.

Although polarization diversity in two dimensions has been long considered [8, 9], leveraging all three spatial dimensions has received limited attention [4, 10]. Furthermore, the consideration of depolarization along with channel loss, to the best of our knowledge, has yet to be explored. Thus another contribution of this work is to suggest means for characterizing these random effects.

3.3 Experimental Results

We first present empirical data illustrating that the channel effects in severe multipath environments are highly sensitive in multiple dimensions, specifically, to extremely small changes in frequency, the polarization utilized, and the device's position.

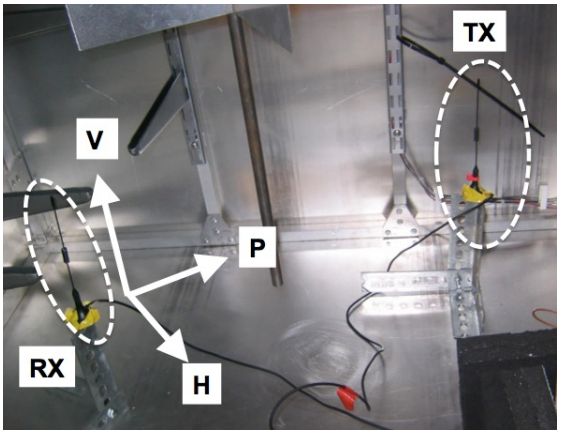

Figure 3.1: Measurement setup in a compact reverberation chamber with transmit (TX) and receive (RX) antennas. Arrows indicate directions for the three receive antenna linear polarizations: V, H, and P.

3.3.1 Methodology

S_{21} measurements were conducted, using a vector network analyzer (Agilent 8722ES), between two linearly-polarized, monopole antennas. The antennas were placed approximately 1 m apart in a compact (0.9 m $\times$ 0.9 m $\times$ 0.3 m) reverberation chamber capable of creating a variety of channel conditions ranging from the benign (i.e., high-K, Rician) to the severe (i.e., two-ray, hyper-Rayleigh) [52]. As reverberation chambers have been shown to emulate channel characteristics similar to industrial sites [53], we contend our test environment will similarly emulate conditions that may be seen by M2M systems. Testing was conducted with the transmit antenna oriented with vertical polarization. The receive antenna was oriented to one of three, mutually orthogonal, orientations (as illustrated in Fig. 6.1): (1) vertical (V), (2) horizontally orthogonal to wave propagation (H), and (3) coinciding and parallel to the transmitter to receiver propagation direction (P). For each of the three polarization configurations (i.e., VV, HV, and PV), S_{21} sweeps were made between 2.40 GHz and 2.48 GHz (bandwidth of 80 MHz).

3.3.2 Frequency and Polarization Dependency

Fig. 3.2 shows copolar and crosspolar S_{21} data for our initial test position. Here we see the data indicate that (1) the three measurements are highly variable illustrating significant multipath effects and (2) there is little to no cross polarization discrimination (XPD) in that the median

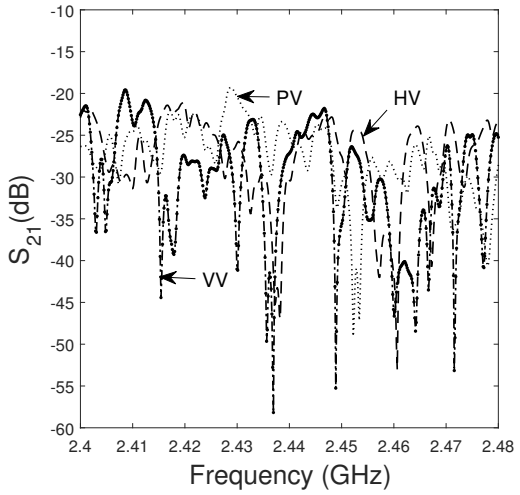

Figure 3.2: Copol and crosspol S_{21} in dB for V polarized transmit antenna.

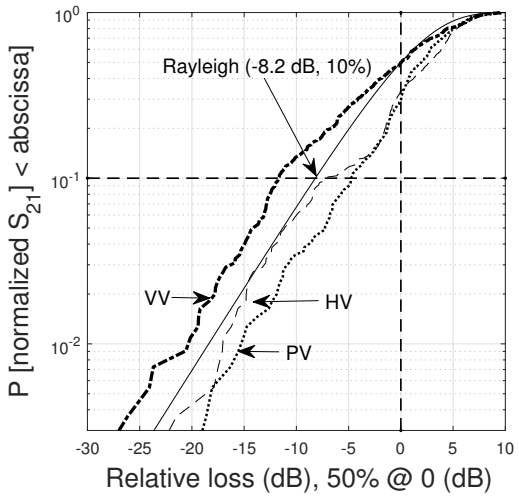

Figure 3.3: CDF of S_{21} data presented in Fig. 3.2. Curves are normalized to median S_{VV} value of -29.04 dB.

value for S_{VV} (-29.0 dB) is within 3 dB of the S_{HV} and S_{PV} values (-26.4 dB and -27.1 dB, respectively). Thus, this environment not only introduces multipath but depolarizes the transmitted wave in three dimensional space, which is noted by the non-inconsequential S_{PV} data.

Statistically, across frequency, we find that the VV case not only exhibits more severe multipath effects than the other two receive antenna polarization scenarios but also effects more

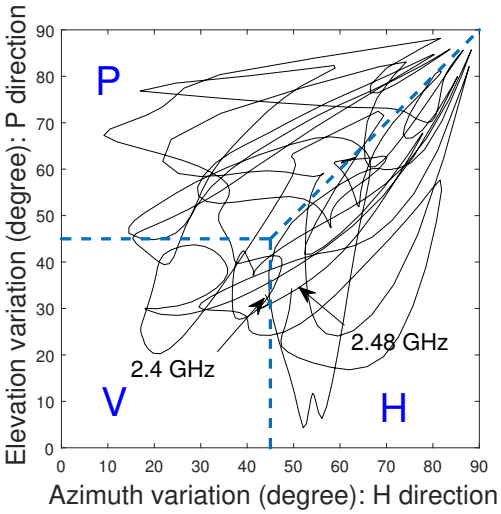

Figure 3.4: Depolarization of vertically transmitted signal in azimuth and elevation.

severe than Rayleigh (Fig. 3.3), as indicated by the VV curve being rotated clock-wise relative to the theoretical Rayleigh curve.

To further illustrate the significance of the depolarization caused by this environment, we utilize the data to determine the optimal orientation for the receive antenna. Depolarization can occur both in azimuth (i.e., toward the H polarization) or in elevation (i.e., toward the P direction). Recall that our S_{21} measurements are a function of frequency (2.40-2.48 GHz), thus we may see variations in the amount of these rotations over frequency. Fig. 3.4 illustrates this effect where the depolarization angles are determined directly from the S_{21} measurements as follows.

$$\theta_{az} = tan^{-1}(|S_{HV}|/|S_{VV}|) \;\&$$

$$\theta_{el} = tan^{-1}(|S_{PV}|/|S_{VV}|) \tag{37}$$

3.3.3 Placement Dependency

One source of user-caused randomness in M2M systems is that associate with the placement of the wireless devices. Fig. 3.5 shows copolar and crosspolar S_{21} data for the same conditions noted for the data presented in § II.B with the exception that the receive antenna has shifted in location by 1 cm (i.e., $< \lambda/10$). Statistically (as seen in Fig. 3.6), we find, in comparison to our

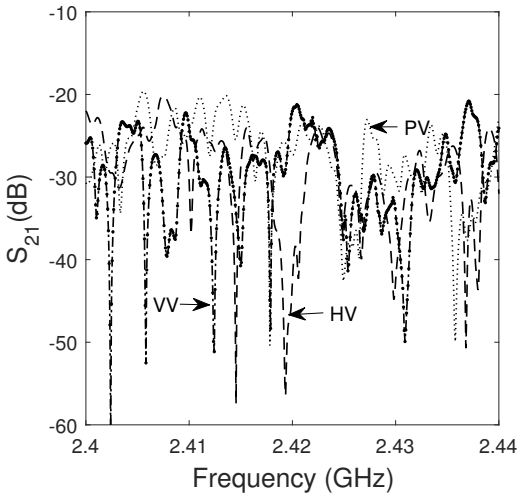

Figure 3.5: Copol and crosspol S_{21} in dB for V polarized transmit antenna with 1 cm shift in receive antenna position.

initial test position, that the S_{VV} case has improved while another case (S_{HV}) has degraded. For both of these positions, a receive antenna oriented in the P statistically provides the best performance of the three orthogonal orientation. However, as suspected, another slight change in position could produce a different result. To show this susceptibility in link performance, we plot in Fig. 3.7 - left the copolar (i.e., VV) S_{21} data from Fig. 3.5 against that from Fig. 3.2. The figure illustrates that moving the antenna less than $\lambda/10$, under otherwise fixed test conditions, can result in S_{21} changes of over 30 dB. Over all frequencies, we find the median absolute change to be 3.8 dB. This results is consistent with the low correlation that we find between the two data sets (i.e., $\rho = 0.47$).

This slight change of position not only changes the channel's S_{21} characteristics but also its depolarization impact. We illustrate this in Fig. 3.7 - right where the depolarization in azimuth for this position is plotted against that seen for the first test position (i.e., the x-axis of Fig. 3.4). This figure shows the lack of correlation in depolarization in the azimuth (H) direction (i.e., $\rho = 0.37$) over frequency. The correlation of depolarization in the elevation (i.e., P) direction is similarly low ($\rho = 0.42$).

We have demonstrated thus far that M2M-like environments can yield significant channel changes across the dimensions of polarization, frequency and space. As each of these dimensions

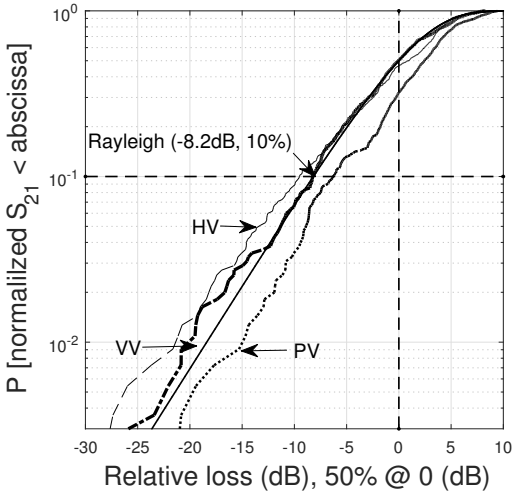

Figure 3.6: CDF of S_{21} data presented in Fig. 3.5. Curves are normalized to median S_{VV} value of -29.04 dB as in Fig. 3.3.

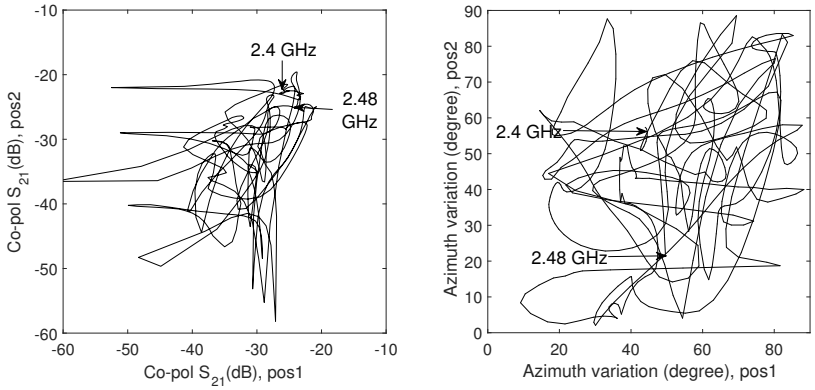

Figure 3.7: Left: Copol (VV) S_{21} vs. VV S_{21} for two test positions separated by $< \lambda/10$ ($\rho = 0.47$). Right:Depolarization correlation (in the azimuth direction) across the 2.4 GHz ISM band between two test positions separated by 1 cm ($\rho = 0.37$).

are non-singular, we can readily conclude that a deterministic approach to ascertaining channel conditions is not a tenable. Thus to categorize an environment using multiple measurements, we leverage a previously suggested metric, the 10% Fade Depth (10%FD) [54]. Calculation of the 10%FD is readily determined from channel measurement data by first finding the median S_{21} value (in dB), next normalizing that data set by the median, and finally sorting the resulting data from low to high. The 10% fade value will be the $N/10^{th}$ value in the resulting data where N is

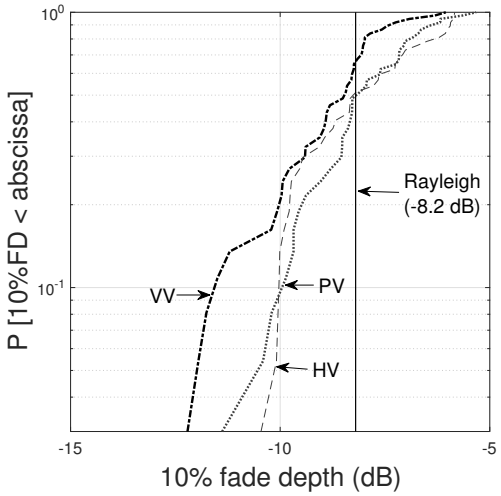

Figure 3.8: 10% fade depth calculated across 37 closely spaced antenna locations and three receive polarizations.

the total number of measurements. Known 10%FD values are -8.2 dB for Rayleigh and -13.1 dB for worst-case (i.e., two-ray) hyper-Rayleigh channels [54]. Using this metric, we analyzed the data collected across 37 closely spaced receive antenna positions and at 551 frequencies between 2.40 and 2.48 GHz. The measurement locations were spaced 1 cm apart in a cross pattern of 25 cm $\times$ 12 cm extent. As illustrated in Fig. 3.8, all three receive antenna polarizations exhibit channel statistics both more benign than Rayleigh (cases to the right of the -8.2 dB Rayleigh line) and worse (cases to the left). For this particular environment and across all locations and frequencies measured, we find over 50% of all measurements exhibit hyper-Rayleigh channel statistics. We also find that cross-polarized links (i.e., HV and PV) are more favorable than the copolar (i.e., VV) configuration for which over 65% exhibit hyper-Rayleigh conditions.

3.3.4 Summary Metric: XPD

Cross-polarization discriminator (XPD) is defined as the ratio of the average power received in the copolarized channel to the average power received in the crosspolarized channels [39]. XPD has been formalized in a 2D framework as follows.

$$XPD_{V:2D} = \frac{\langle S_{VV} S_{VV}^* \rangle}{\langle S_{HV} S_{HV}^* \rangle} \tag{38}$$

Table 3.1: Cross Polar Discrimination (XPD) in 2D and 3D

Scenario	Fig.	V vs. H	V vs. P	V vs. H & P
Antenna Position 1	2	-1.01 dB	-0.88 dB	-0.95 dB
Antenna Position 2	5	-0.25 dB	-1.74 dB	-1.12 dB
Median of all positions	8	0.89 dB	1.63 dB	1.06 dB

Where, for our data, $\langle ... \rangle$ denotes the average calculated over the frequencies of 2.40 GHz to 2.48 GHz. However, to the best of our knowledge, XPD has not been presented in 3D framework. As such, we extend Eq. (48), as follows.

$$XPD_{V:3D} = \frac{\sqrt{2}\langle S_{VV} S_{VV}^* \rangle}{\sqrt{\langle S_{HV} S_{HV}^* \rangle^2 + \langle S_{PV} S_{PV}^* \rangle^2}} \tag{39}$$

Note that the purpose of the $\sqrt{2}$ factor in the numerator is to normalize the sum of the two denominator components.

Lower XPD values indicate more depolarization in a propagation environment. We can see from Table 5.4 that there is low XPD (< 2 dB) between all three directions for our high multipath test environment. Prior work has also shown that such low XPD indicates that diversity techniques can be effective [55] (e.g., effectiveness is maximum when $XPD = 0$ dB [41]). In our case, we see that there is potential to leveraged diversity over three mutually orthogonal polarizations, as indicated by the low XPD seen in the final column of Table 5.4 as calculated using Eq. (39).

3.4 Mitigation with Tripolar Antenna Designs

Given the multipath and three-dimensional depolarization we illustrated in Section 3.3, we now consider a tripolar antenna systems that can mitigate these effects. Earlier studies considered three distinct linear antennas oriented in a mutually orthogonal manner to investigate both diversity [55] and MIMO capacity [10] gains. Subsequently, fully-integrated, tripolar antenna systems were developed for MIMO investigations [32, 56]. For M2M systems, link reliability is arguably more critical than high data rates and thus we consider, as an illustrative example, results obtained from one such prototype integrated antenna system that was designed to operate

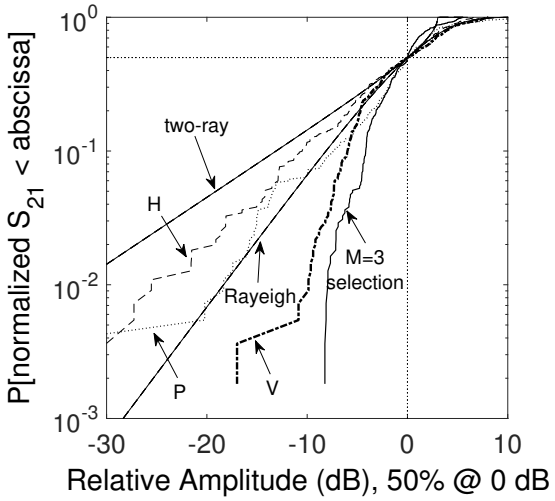

Figure 3.9: Channel statistics for the three orthogonal elements of a prototype tripolar antenna along with M=3 selection diversity results.

from 5.40 to 5.48 GHz [57].

The prototype antenna was placed arbitrarily in our test chamber (Fig. 6.1) to receive the signal from a vertically oriented transmit antenna. The statistics associated with the three measured responses are shown in Fig. 3.9. For this particular placement, one polarization exhibits Rician fading (V), another is approximately Rayleigh (P), and the third is hyper-Rayleigh (H). As shown in § II, for these types of environments, the link statistics can be highly dependent on very small changes in location and/or frequency, thus motivating one to exploit the available diversity enabled by the tripolar design. As such, also shown is the result of implementing arguably the simplest diversity/adaptation technique of selecting the best of the $M = 3$ paths. This technique results in a relatively benign Rician environment ($K \approx 2.5$ dB) even when the conditions seen by the three individual component polarizations are statistically significantly worse. Such adaptation can be readily done *in situ* and with little computation by a M2M device by leveraging the receive signal strength indication (RSSI) feature inherent in modern wireless chipsets.

3.5 Conclusion

In this work, we present channel data collected in an environment that emulates that which may be seen for M2M systems. The work illustrates that channel variations are highly variable and dependent on small dimensional changes in frequency and space and that depolarization occurs across all three spatial dimensions. Because of the sensitivity to device placement by the user, deterministic modeling of these channels is not tenable. We thus illustrate the use of the 10%FD to statistically characterize the environments and a 3D XPD metric to show the three dimensional impact of depolarization. Future work includes developing compact tripolar antenna systems that can be readily integrated in M2M devices and which can adapt to these random channel conditions.

4 Tripolar Antenna Geometry and Fabrication

Foreword

This chapter the development of a tripolar antenna design for M2M application. 3D-printing offers a low-cost and low-to-medium-volume manufacturing technology and therefore is a good option for fabrication of the tripolar antenna. A constraint faced by 3D printing in regards to the deposition of the conductive material is build angle. Section 4.1 is presented in "2017 11^{th} European Conference on Antennas and Propagation (EuCAP)" [58]. In this section, the performance of a tripolar antenna system that conforms to the 3D build angle constraint of 45° is evaluated. The data showed that this design provide the same diversity gain as a tripolar antenna design with one vertically polarized element and thus the geometric constraints of 3D printing do not prevent the fabrication of an effective tripolar antenna system. Section 4.2 that presents the paper submitted to "2019 IEEE Antennas and Wireless Propagation Letters". This paper is built on the results obtained in the first part of this chapter. It discusses fabrication of the tripolar antenna using 3D printing technology. The antenna fabrication is done in University of South Florida. My contribution in latter work was to testing antennas in multipath environments.

4.1 Characterization of a Geometrically Constrained Tripolar Antenna Under M2M Channel Conditions

4.1.1 Abstract

Historically, antenna designs have been dictated by specific performance requirements for gain, beammwidth, return loss, etc. without consideration of the environment the antenna is being deployed in. Herein, we consider an over-the-air (OTA) approach for characterizing antenna performance for a wireless device arbitrarily deployed in a cluttered environment, e.g., a machine-to-machine (M2M) installation. We then explore antenna system geometries that can be cofabricated with the device's enclosure using 3D printing technologies. Based on a channel characterization study and fabrication constraints, we propose a tripolar antenna design that is

readily integrated with, for example, a wireless sensor [4].

4.1.2 Introduction

Machine-to-machine (M2M) systems promise to form a significant portion of future wireless systems and will push deployments into evermore cluttered environments (e.g., factory floors) that are likely to produce non-line-of-sight (NLOS) and/or severe multipath conditions. These environments can also depolarize the transmitted signal in all three spatial dimensions [30]. Recent work has shown that tripolar antenna systems offer a compact approach to mitigate these type of propagation environments [59], particularly, if diversity schemes (e.g., polarization selectivity) are also pursued. Fabrication of tripolar antenna with mutually well-isolated (<-15 dB) orthogonal branches has been considered before [31, 32, 56]. However, to the best of our knowledge, mass production of such antennas has not been pursued.

Thus, in addition to designing antennas which can improve system reliability and reduce transmit power requirements, a consideration of this paper is reducing the cost of antenna integration. Planar antennas for consumer wireless devices often come in the form of surface mount chips that are bonded to a printed circuit board, or simply adhesive-backed conductive strips that are attached to cases. However, volumetric three-dimensional antenna systems, such as proposed herein, require more complex manufacturing approaches. The use of multi-material 3D-printing, that combines the deposition of thermoplastic substrates and conductive traces, is one possibility for low cost, low- to medium-volume manufacturing as illustrated in [60, 61]. Demonstrating the suitability of a 3D printing approach for the proposed tripolar antennas is one goal of this work. A constraint faced by 3D printing in regards to the deposition of the conductive material is build angle (in our case, the limit is 45°). Some work has been done aiming for conformal printing of electronics and antennas [62, 63], but physical adjustments are often necessary during fabrication to complete the ink deposition. Our efforts hope to alleviate these extra steps.

Because of the 3D build angle constraint of 45°, we compare herein the performance of a

[4] Golmohamadi, M., Ramirez, R., Hewgill, B., Jamison, J., Frolik, J. and Weller, T.. 2017, March. Characterization of a geometrically constrained tripolar antenna under M2M channel conditions. In Antennas and Propagation (EUCAP), 2017 11th European Conference on (pp. 2998-3002). IEEE.

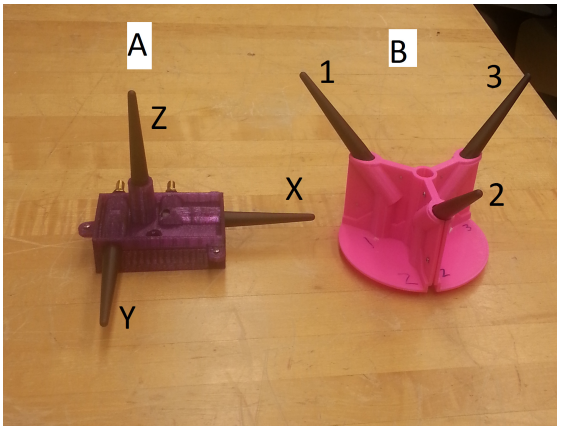

Figure 4.1: Antenna array surrogates. Left: Cartesian-based $Array_A$. Right: "Out-of-plane" $Array_B$

surrogate tripolar antenna system that conforms to this build angle against a tripolar antenna system based on Cartesian coordinates. Our Cartesian-based antenna system, $Array_A$ can be seen on the left of Fig. 4.1. It can be noted that the Z element is at an angle of 90° and thus could not be 3D printed based on our working constraint. Our 3D "out-of-plane" surrogate, $Array_B$, can be seen on the right. Each of the three elements of this array (i.e., 1, 2, and 3) are at an angle of 45° and thus could be 3D printed. We compare these arrays in two distinct environments. One environment emulates a highly reflective environment that could be experienced by a M2M system operating in a factory or within a large machine. The second environment considers a working laboratory that could also emulate a NLOS office environment.

We organize this paper as follows. In Section 2, we present the two tripolar antenna systems that are used in this work and discuss our test and analysis methodologies. In Section 3, the performance of both antennas over multiple cases of over-the-air (OTA) testing in the two different deployment scenarios are compared. We find that in both environments the performance of the two antenna arrays over many test cases are statistically equivalent. In Section 4, a proposed design for a 3D fabricated tripolar "out-of-plane" antenna array is presented that could be integrated with a commercial wireless sensor product. Section V concludes the work and outlines future efforts related to antenna system integration and test.

4.1.3 Methodology

In this section we discuss the the two antenna geometries, along with the channel measurement and analysis approaches.

4.1.3.1 Antenna Arrays

Two tripolar antenna arrays (Fig. 4.1) have been considered in this work. $Array_A$, seen in Fig. 4.1-left, is composed of three mutually orthogonal monopole antennas placed along X, Y, Z axes of the Cartesian coordinate system (where Z corresponds to vertical polarization). $Array_B$, seen in Fig. 4.1-right), utilizes the same monopoles but these are oriented 45° from the horizontal plane and uniformly separated radially by 120°. These elements are approaching mutual orthogonality with a minimum separation angle of 75°. When deployed, Element *2* of $Array_B$ lies in the YZ plane of $Array_A$. Elements *1* and *3* are 30° with respect to the XZ plane.

Mutual coupling between all the three elements for each antenna arrays was measured in an anechoic environment. While these arrays were fabricated for demonstration purposes and have elements that are not truly orthogonal, the mutual coupling is <-29 dB between any two array elements.

4.1.3.2 Test Setup

Unlike mobile communication systems where the user and/or the environment are moving/dynamic, a M2M device could experience static channel conditions once placed in the environment. However, for severe multipath and depolarizing environments, link propagation loss is highly dependent on placement and frequency of operation. As shown herein, 30 dB variations can occur with movements of as little as $\lambda/10$ and frequency shifts of <150 kHz for center frequencies in the 2.4 GHz band (i.e., <0.01% proportional shift).

As noted, link measurements were conducted in two surrogate environments, one comparable to a highly reflective factory setting, the other comparable to an office setting. A compact (0.9 $m\times$ 0.9 $m\times$ 0.3 m) reverberation chamber (Fig. 4.2) was utilized to create the highly reflective scenario. The second was a NLOS condition within a lab (Fig. 5.2). An Anritsu MS2036A vector

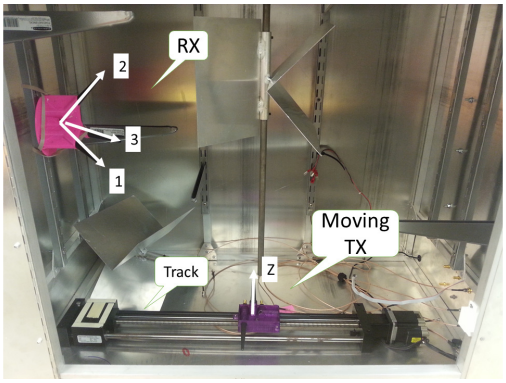

Figure 4.2: Test setup inside highly reflective, compact reverberation chamber used to emulate "factory" conditions.

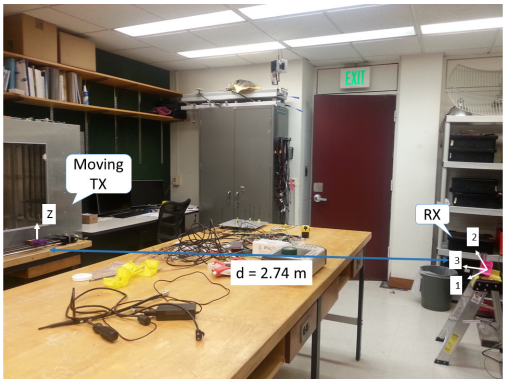

Figure 4.3: Test setup for NLOS "office" conditions.

network analyzer was used to measure S_{21} (i.e., path loss) between the a vertically polarized (i.e., Z-oriented) transmit antenna and one element of the receive tripolar array. Measurements were made at 551 frequencies in the range of 2.40 GHz to 2.48 GHz. To emulate the random placement of the transmitting device, the transmit antenna was mounted on a LabView controlled linear track that allowed positioning to one of 50 repeatable locations in 1 cm (i.e., $< \lambda/10$) increments.

To analyze antenna array performance, we consider the S_{21} statistics. As illustrated in (Fig. 4.4), S_{21} data for the reverberation chamber (Fig. 4.2) shows significant frequency-selective multipath, of up to 30 dB in some instances, for this particular position of the transmit antenna, irrespective of which receive array element is considered. Note that the receive arrays were wall mounted in the chamber.

Fig. 4.5 shows the cumulative distribution of the S_{21} data presented in Fig. 4.4. We find for

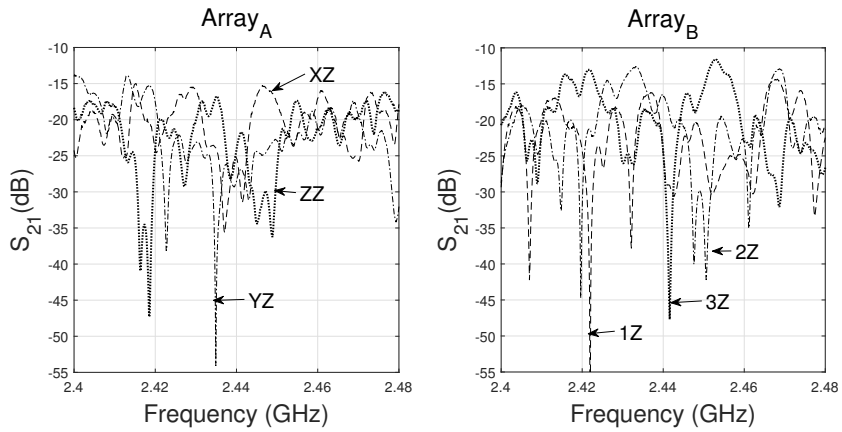

Figure 4.4: Sample S_{21} reverberation chamber data for one location of a vertically polarized (Z direction) transmit antenna with arrays used at the receive side. Left: $Array_A$, Right: $Array_B$.

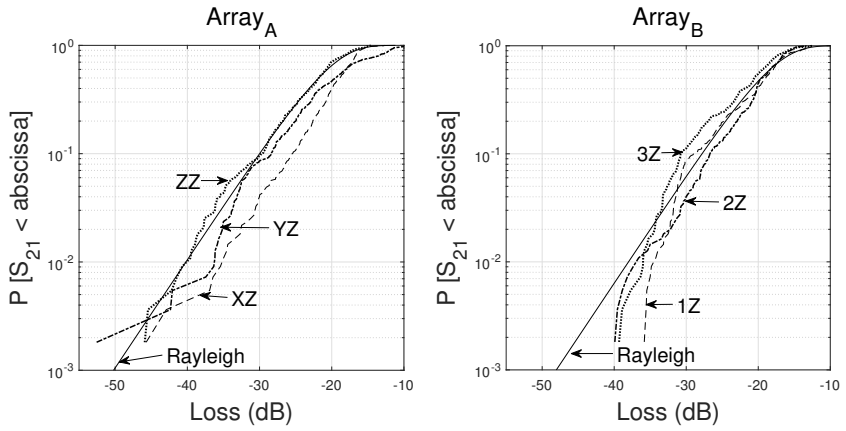

Figure 4.5: CDF of S_{21} reverberation chamber data shown in Fig. 4.4. Left: $Array_A$, Right: $Array_B$.

$Array_A$ that the copolar (i.e., ZZ) configuration is not necessarily the best even though the range is short ($\sim 1m$) and there is a direct line-of-site (LOS) condition. At this particular position, ZZ reveals link characteristics worse than what are observed for cross-pol links (i.e., XZ and YZ). When $Array_B$ is used at the receiver, there are not strictly copol or crosspol elements. That being said, the performance of $Array_B$ in the reverberation chamber is comparable to that of $Array_A$ in the nominal sense (e.g., median loss in both cases is $\sim$25 dB). However, the multipath

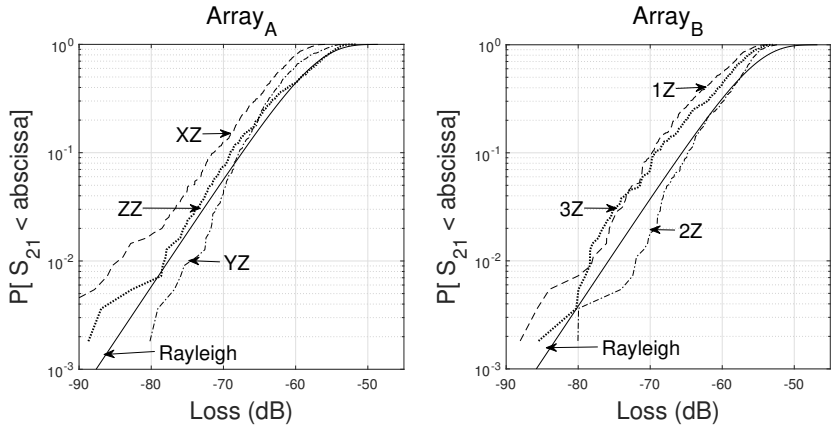

Figure 4.6: CDF of S_{21} data inside office at one TX position. Left: $Array_A$. Right: $Array_B$.

effects experienced by $Array_B$ are seen to be more benign (i.e., all curves fall below the Rayleigh reference line). Note that these same measurements conducted in an anechoic environment do clearly show the advantage of a copolar (i.e., ZZ) configuration over the other five (i.e., XZ and YZ for $Array_A$ and $1Z$, $2Z$ and $3Z$ for $Array_B$) measured links.

We conducted a similar measurement in our lab (Fig. 5.2) to emulate a NLOS office setup. In this case, the antennas were separated by $\sim 2.7m$. The analysis of this data is presented in Fig. 4.6. In comparison to the reverberation chamber data (Fig. 4.5), we see the curves are in absolute value at a lower value indicating a greater large-scale (i.e., nominal) path loss as expected for the increased distance and NLOS conditions. We also note that all the curves follow a shape similar to the Rayleigh reference, as also would be expected for this NLOS environment. However, and most significantly, the copolarized link (i.e., ZZ) is not better than an explicitly crosspolarized case (i.e., YZ). On the whole, for this particular position of the transmit antenna, element $2Z$ of $Array_B$ provides the best link performance for over 99% of the measured frequencies. However, as we will discuss next, slightly different positioning of either the transmit antenna or receive antenna array could yield completely different results.

4.1.4 Summary and Impact of Selection Diversity

The previous section illustrated the test methodology and presented illustrative data for a single position in each of the considered environments. We contend that placement of M2M devices in the environment will be dictated by what is expedient for the installer and will not necessarily be dictated by link quality considerations. As such, we consider in this section the performance of each link over multiple spatial considerations. This testing was enabled by moving the vertical transmit antenna to one of 50 closely spaced (1 cm) positions along the aforementioned linear track.

Furthermore, we consider the scenario where the M2M device would implement arguably the simplest of diversity techniques, selection diversity, in which the device would choose the "best" of the tripolar elements. That is, the device would choose the element which results in the strongest signal, which could be determined using the device's received signal strength indicator (RSSI). We show that this approach improves the overall channel statistics by reducing the probability of deep fades and consequently the margins needed in link budgets to maintain a desired quality of service (QoS).

4.1.4.1 Reverberation Chamber Results

Fig. 4.7 shows the summarized results of measurements taken in the reverberation chamber. In total, we are presenting the results of over 27,000 measurements (50 positions $\times$ 551 frequencies). We show the copol curve (i.e., ZZ) for reference but it should be noted that the other five links exhibited comparable CDF curves (i.e., within $\sim$2 dB).

In Fig. 4.7 we also show the CDF when $M = 3$ selection diversity is implemented for each of the arrays. In both cases, the 1% link margin is improved by over 13 dB in this environment. That is, for a QoS of 99% link reliability, the margin or, equivalently, transmit power could be reduced by over 13 dB if $M = 3$ selection diversity is used versus just any one of the single elements. As in [64], we determine diversity gain as the ratio relative to the strongest individual branch (i.e., element) of a particular array. This result further illustrates that the performance of the "out-of-plane" $Array_B$ design is not significantly different from an antenna designed to be copolar with the transmit antenna. In this environment, the 1% link margin gain is 13.6 dB

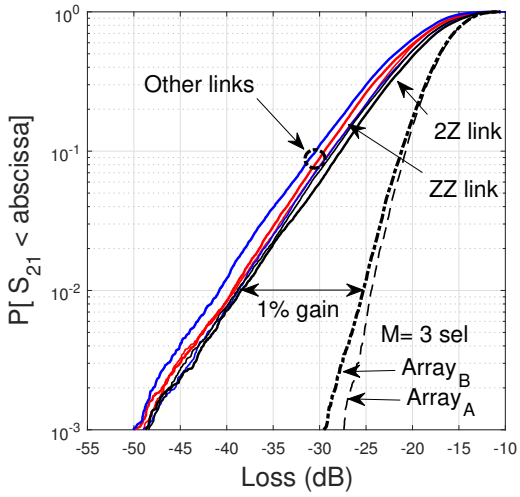

Figure 4.7: $M = 3$ selection diversity in reverberation chamber is shown to increase 1% link margins by over 13 dB for both arrays with $Array_A$ showing slightly better performance.

for $Array_B$ versus 14.4 dB for $Array_A$.

4.1.4.2 NLOS Lab Results

Fig. 4.8 presents results of the extensive measurements conducted under our NLOS lab condition. In contrast to the reverberation chamber results (Fig. 4.7), we find that element YZ of $Array_A$ and $3Z$ of $Array_B$ are found to be the "strongest individual branches" and have comparable performance. This result illustrates the need for M2M antennas that are adaptable to the channel conditions created by the application's setting. When $M = 3$ selection diversity is employed, we find further evidence that in "real-world" environments these two arrays will perform equivalently (i.e., 1% diversity gain is ∼13.3 dB for both).

4.1.5 Proposed Antenna

The results presented thus far indicate that statistically, for the two environments considered, a tripolar receive antenna array that is rotated 45° relative to a vertical transmit antenna performs is no worse than a tripolar array that has one element copolar. This result thus enables us to propose a tripolar design that can be arbitrarily oriented in space and readily fabricated using 3D printing methods. Fig. 4.9 shows the proposed tripolar antenna geometry, with all

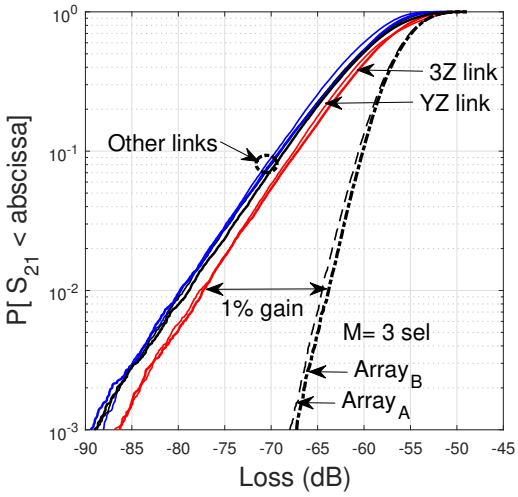

Figure 4.8: $M = 3$ selection diversity under NLOS lab conditions is shown to increase 1% link margins by also over 13 dB for both arrays with $Array_B$ showing slightly better performance.

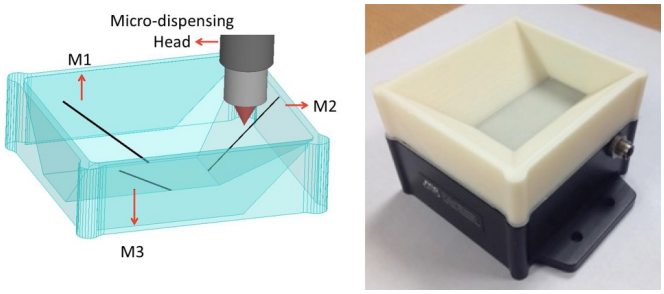

Figure 4.9: Proposed antenna geometry (left), fabricated ABS substrate (right).

three elements perpendicular to each other and rotated 45° with respect to the Z axis. This orientation is important because most 3D printing tools, including the micro-dispensing system used for this work, are incapable of depositing conductive pastes or inks in the Z-direction (normal to the printing platform). Accordingly, manufacturing a configuration such as $Array_A$ using 3D printing would require an additional step to physically rotate the part during the printing process.

Fused deposition modeling and micro-dispensing are the fabrication techniques proposed to produce the substrate and conductive layers, respectively. The dielectric sections are fabricated with a ceramic tip heated at 235° C; allowing printing of 250 μm thick ABS layers.

Since the resulting substrate is a relatively non-flat and uneven 3D surface, a laser displace-

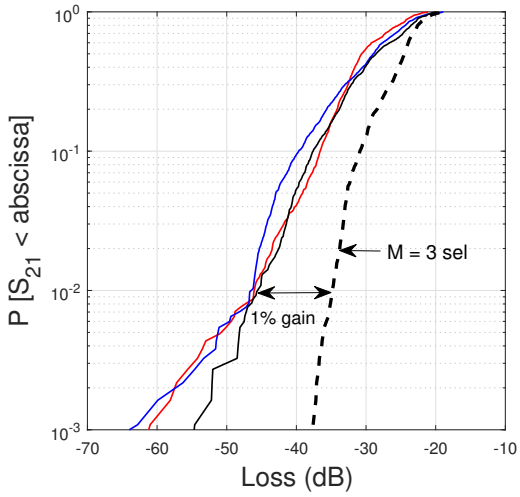

Figure 4.10: Initial results from a prototype 3D printed antenna. Measurements from a single position in a multipath environment show comparable individual links and that $M = 3$ selection diversity improves the 1% link margin >11 dB.

ment sensor is necessary for conformal printing. A grid map is performed to scan the surface along a defined pattern with a resolution of not less than 0.2 mm. The data collected from this scan is triangulated into a mesh for collision detection. The micro-dispensing head is then used to deposit the silver paste (DuPont CB028) to pattern the antenna elements; the height of the generated mesh will be adjusted to conform approximately to the surface with a clearance gap between the nozzle and the target surface of 100 μ m. All three processes are realized using an nScrypt Tabletop 3Dn printer.

Fig. 4.10 presents initial results from a prototype 3D printed antenna array of the design illustrated in Fig. 4.9. S_{21} link measurements were made in our compact reverberation chamber at 1840 points between 2.40 and 2.48 GHz between each array element and a transmit antenna. The individual links have comparable characteristics with median losses ranging from approximately 28.5 to 30 dB. Thus, just as was seen earlier, this scenario results in no particular single element being "best". However, employing selection diversity among the three elements improves the 1% link margin by over 11 dB; again showing the importance of arrays being adaptive in such environments.

4.1.6 Conclusion

Herein we present the results of over-the-air testing conducted to demonstrate the efficacy of a tripolar receive antenna array that is not copolar with with its vertically-oriented transmit counterpart. The investigation showed that over two distinct environments, this antenna performed no worse than a tripolar antenna in which one element was vertically polarized. The two environments we chosen to represent a highly reflective industrial environment and an NLOS office environment. For each environment, the transmit antenna was moved, in small increments, to 50 different locations and S_{21} channel data was collected at 551 frequencies in the 2.4 GHz ISM band.

The results of this investigation demonstrate that the geometric constraints of multi-material 3D printing do not prevent the fabrication of an effective tripolar antenna system that can be an integral part of the wireless device's packaging. We presented a preliminary design and data for such an antenna system. Future work includes integration of a compact, tripolar antenna system with commercial wireless sensor hardware and implementing algorithms that leverage the wireless chipset's RSSI measurement to configure the tripolar array either using selection diversity, whose efficacy was demonstrated herein, and/or limited phasing of the three constituent array elements.

4.2 Additive Manufactured, On-Package 2.4 GHz Tripolar Antenna Systems for Harsh Wireless Channels

4.2.1 Abstract

Two distinct and compact, 3D printed tripolar antenna systems operating at 2.4 GHz are presented. Both antennas are designed for integration with commercial wireless nodes with the purpose of mitigating multipath and depolarization channel effects that might be present in many machine-to-machine (M2M) deployments. The antennas are fabricated as a single-piece, utilizing fused deposition modeling for dielectric parts and micro-dispensing of silver paste for conductive layers. Over the air testing demonstrates that by leveraging the diversity provided by the three mutually orthogonal monopoles, a 1% channel improvement of up to 14 dB can be achieved in a highly-reflective, fading environment. This improvement leads to better bit error rate (BER) performance (as is also shown). Additionally, RSSI measurements show significant improvement when the prototype antenna system is integrated with a commercially-available wireless sensor. Implications of tripolar antenna integration on M2M systems include reduction in energy use, longer wireless communication link distances, and/or greater link reliability[5].

4.2.2 Introduction

The Internet of Things (IoT) or Industrial Internet, generally refers to systems of electro-mechanical machines and devices interconnected to one another through embedded wireless sensors and actuators; a network that enables continuous machine-to-machine (M2M) communication is often realized autonomously without the need of any human intervention [65]. The M2M communications market is predicted to grow to a value by 2022 anywhere from US $28B to $200B [66, 67]; which is why energy-efficient, small size, reliable and low-cost wireless sensor nodes are of great interest for industrial, commercial and aerospace applications. The devices that comprise the M2M networks will in most cases be expected to undergo alterations in physical temperature, pressure, moisture, etc.; and will be deployed in settings that are harsh for wireless

[5]Ramirez, R.A., Golmohamadi, M., Jamison, Frolik, J., and Weller, T.M.. To be submitted. Additive Manufactured, On-Package 2.4 GHz Tripolar Antenna System for Harsh Wireless Channels. IEEE Antennas and Wireless Propagation Letters. **note it has been reviewed twice and has been rejected. It is now in revision**.

communications (e.g., non-line-of-sight (NLOS) and with severe multipath), environments that can weaken and depolarize a transmitted signal across all three spatial dimensions [12,30,68]. In such environments, several copies of the transmitted signal will show up at the receiver, such that each copy corresponds to a distinct multipath component with a distinct delay. The amplitude of these summed signals can experience fast variations over time, space, and/or frequency due to constructive and destructive combining [11].

To mitigate such fading effects, diversity-combining of independently fading signal paths can be applied which leverages different frequencies and/or antenna elements [11]. For M2M systems that involve multiple devices, coordinating the best frequency to use is not a viable diversity approach, for it is possible that an appropriate frequency for one particular device to device link may exhibit deep fades in another. Employing multiple antennas (i.e., spatial diversity) requires elements to be located sufficiently far from each other ($\sim \lambda/2$) to guarantee uncorrelated fading effects [69]. This constraint makes spatial diversity an undesirable approach for applications (e.g., low-cost IoT systems) where the size of the antenna system is a crucial design parameter.

As noted, multi-element antenna diversity can improve link reliability thus allowing for the reduction of the transmitted RF power (to save energy), but at the cost of a bulkier node design. To address this problem, in [70], a cooperative spatial diversity technique was incorporated in sensor nodes to improve link reliability. The approach utilizes several compact transmitter nodes to send a message to a single destination. The trade off in this approach is added complexity in node computation and network communications. An alternative method described in [71] employs frequency diversity to improve link quality, however it required two radios separated by 65 cm for each node and therefore is not suitable for compact installations. In the work presented herein, we leverage polarization diversity as a means to provide a compact and relatively uncomplicated approach for improving communication link quality in M2M systems.

Cross-polarized antenna systems, through their perpendicular/orthogonal elements, provide signal paths that are weakly correlated, while keeping antenna elements colocated. Recently, two dimensional polarization diversity has been exploited in sensor node design. For example, a dual-polarized, 2.4 GHz patch antenna was proposed for integration into a wireless node in order to mitigate body shadowing effect in wearable communication systems. Implementing selection diversity improved the 1% outage probability by providing gain of 9.5 dB [72,73].

In the presence of reflectors and retarders, an environment can lead to depolarization in all three spatial dimensions [10]. In recognition of 3D depolarization, there has been some efforts in designing antennas to leverage the extra degree of freedom [74]. For example, use of colocated antenna elements with three (one loop and two coplanar dipoles) and four elements (one loop and three mutually orthogonal dipoles) led to channel capacities greater than a single element antenna [31]. Tripolarized antennas have also been shown to achieve channel capacities comparable to three spatially separated single polarized antennas in a MIMO system [32].

A tripolar antenna meant to be integrated on a sensor node was previously presented by the authors in [51] where pieces of the antenna package were printed separately and post-assembled manually into a 3D form-factor, a drawback that reduce attractiveness for low- to middle-scale production. A subsequent design, fabricated as a single piece, was introduced in [75] and will be further analyzed in this work (i.e., the square antenna seen in Fig. 4.11). However, to the best of our knowledge, full characterization and integration of a tripolar antenna into a wireless node has not been reported.

This paper presents two tripolar antennas that were 3D printed in a single-piece construction and intended for communication channels that experience significant multipath and depolarization. The antenna systems are integrated into the packaging of sensor nodes using an additive manufacturing approach that combines fused deposition modeling (FDM) of the plastic case and micro-dispensing of conductive pastes to realize the antenna elements; both methods combined have been proven to perform efficiently up to mm-wave frequencies [76–79]. We present the performance of these two antenna designs using both traditional antenna characterization measures (S_{11}, patterns) and through over-the-air (OTA) testing in a harsh communications environment. The proposed tripolar antenna systems achieve a return loss greater than 15 dB at 2.4 GHz and, when tested in a highly variable multipath environment, a 1% channel improvement of up to 14 dB by leveraging the diversity provided by the system's three mutually orthogonal elements. This improvement is shown herein to correspond directly to improved bit error rate (BER) improvement or could allow nodes to communicate either at lower transmit power (saving energy) or over greater distances.

The content of this paper is organized as follows. In Section 4.2.3, the designs of two tripolar antenna systems are discussed. Antenna characteristics, propagation measurements in anechoic

and reverberation environments along with improvements gained in BER and in signal quality are presented in Section 4.2.4, 4.2.5, and 4.2.6, respectively.

4.2.3 Antenna Systems Design and Fabrication

The multipolar antenna systems presented herein were custom designed to fit and replace covers of two commercial wireless sensor node packages; packages with different dimensions and geometries were selected to show the versatility of the additive manufacturing technology. These nodes are generally produced on a low to medium volume scale, making the FDM fabrication approach a valid low cost and robust alternative.

Fig. 4.11 (left) and Fig. 4.12 show the dimensions, geometry and angular arrangement of the first proposed, 'square' tripolar system having total height of 21 mm, length of 65 mm, and width of 60 mm. The system is seen integrated on top of a 2.4 GHz sensor node in Fig. 4.11 (right).

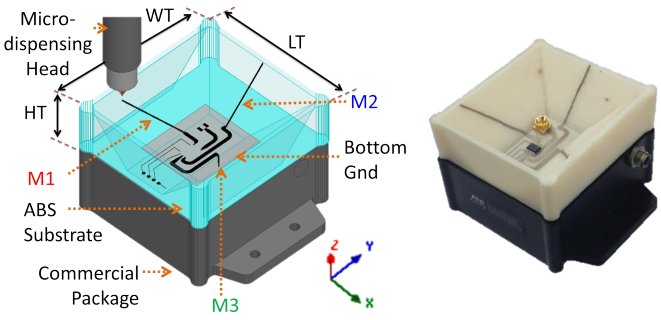

Figure 4.11: Square antenna design (left), and fabricated prototype on top of a commercial wireless node (right).

Similarly, Fig. 4.13, shows the dimensions of a second 2.4 GHz, 'circular' tripolar antenna, designed to be placed on top of a cylindrical node; with total height of 11 mm, bottom diameter of 33 mm and top diameter of 40 mm.

The antenna designs are based off three mutually orthogonal $\lambda/4$ monopoles operating at 2.4 GHz; each radiating element is directly printed over 45° sloped substrate walls, a value that represents the maximum printing angle supported by most additive manufacturing systems, including the one used for this work [80]. The complete process is realized in a single-piece construction and avoids the need for physical part rotations to achieve orthogonality between

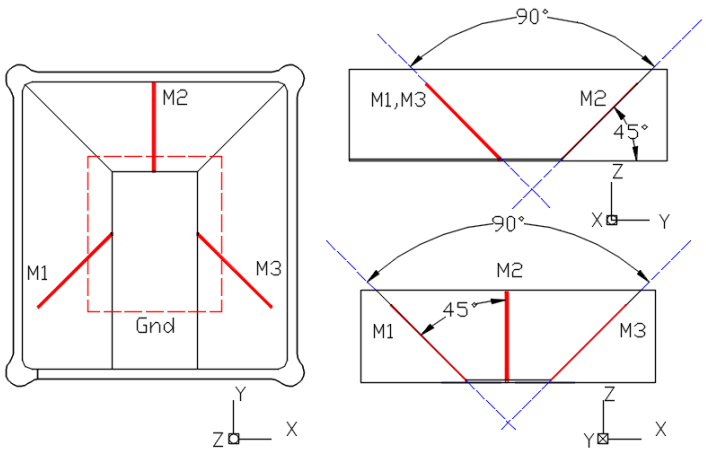

Figure 4.12: Square antenna geometry and angular arrangement between elements.

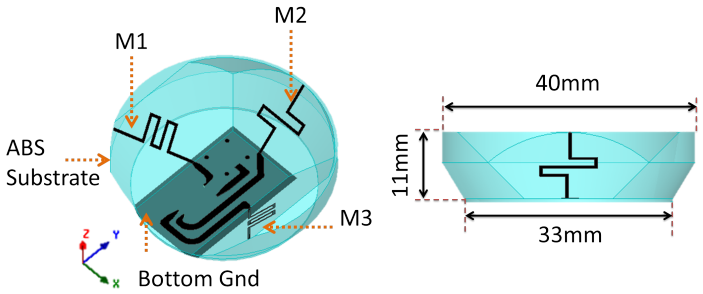

Figure 4.13: Circular tripolar antenna design.

X, Y, and Z antenna elements. Each monopole is fed with a 50 Ω microstrip line, printed over a 500 μm thick flat substrate. The lines are subsequently connected to an externally controlled SP3T integrated circuit (Analog-Devices HMC245AQS1) that is used to switch between the individual polarization states without any specific phasing arrangement between them. The SP3T switch and SMP connector were manually placed and fixed onto the 500 um thick ABS substrate with a two-part dielectric epoxy. Interconnection was achieved through dispensing of DuPont CB028 silver paste with a subsequent drying stage at 90°C for 60 minutes.

The processes used for the fabrication of both antenna devices are FDM and micro-dispensing. FDM utilizes acrylonitrile butadiene styrene (ABS) with measured properties at 1 GHz of $\epsilon_r \sim 2.6$ and $tan(\delta) \sim 0.0058$, to create the three-dimensional dielectric substrate. The ABS filament is extruded through a ceramic 125 μm inner diameter tip at 235°C and patterned layer by

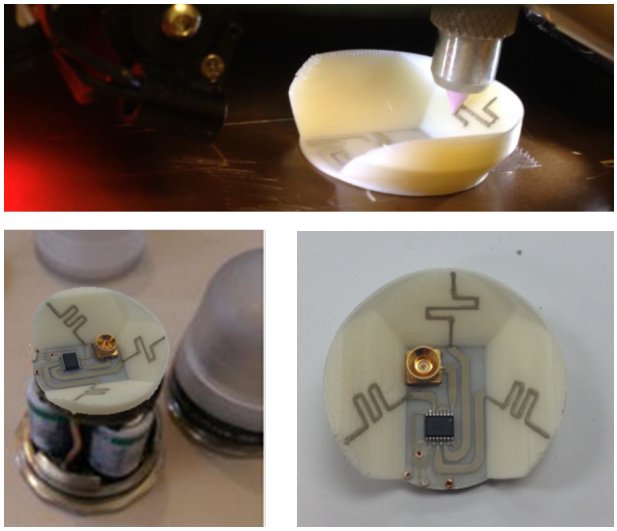

Figure 4.14: Microdispensing head on a sloped wall (top), fabricated circular antenna prototype (bottom right) on a commercial wireless node (bottom left).

layer onto a metallic bed pre-heated at 110°C. The 3D surface is then laser-scanned to create a topography mesh that will guide the micro-dispensing head to conform to the surface while depositing the conductive parts, as shown in Fig. 4.11 (left) and Fig. 4.14 (top). DuPont CB028 is the material used for the conductive traces; a silver paste which possesses a conductivity of ∼16 S/m once it undergoes a 90°C drying stage for 60 minutes. All three processes are realized using an nScrypt Tabletop 3Dn printer (FDM head, laser displacement sensor and micro-dispensing head). Fig. 4.11 (right) and Fig. 4.14 (bottom) show the fabricated square and circular antenna prototypes placed on top of the commercial sensor node packages, respectively. Coaxial SMP connectors were used on both prototypes for the RF output signal; the connector and the 3-way switch are manually placed and connected.

4.2.4 Antenna Characteristics

In order to demonstrate radiation characteristics and the advantages of implementing polarization diversity, the performance of each antenna is tested in both anechoic and reflective environments. This testing allows the determination of the antenna radiation patterns and cumulative distribution functions of fading statistics, respectively. Along with these results, the transmission and reflection coefficients for the antenna ports are shown in this section.

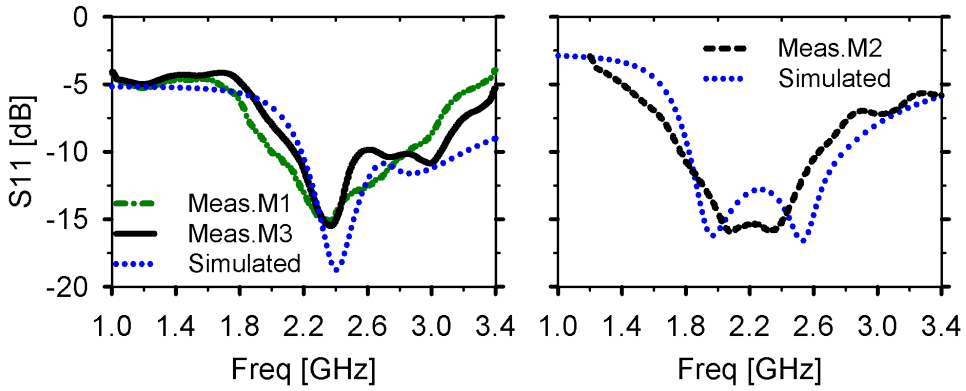

Figure 4.15: Square antenna simulated and measured reflection coefficient: M1-M3 (left), M2 (right).

4.2.4.1 Network Properties and Performance in Anechoic Environments

The measured and simulated input reflection coefficients of the square antenna for monopoles M1 and M3, both of which are rotated 45° with respect to the Z and X axes, are shown in Fig. 4.15 (left). Similarly, Fig. 4.15 (right) shows the reflection coefficient for monopole M2, which is rotated 45° with respect to the Z axis. The return loss is greater than 15 dB at 2.4 GHz on all elements, with a worst case 10 dB bandwidth extending from 2.1 GHz up to 2.8 GHz (i.e., 700 MHz).

Fig. 4.16 (a) and (b) show the measured and simulated radiation gain patterns at 2.4 GHz for monopoles M1, M3 and M2, respectively. The data correspond to the antenna azimuth plane against a vertically oriented transmitter horn antenna. That is, the X-Y plane follows the reference axes shown in Fig. 4.11 and Fig. 4.12. Fig. 4.16 (c-e) show the simulated 3D gain pattern when each individual monopole is selected. From each pattern, one will note that a null is aligned along the monopole axis, ensuring pattern orthogonality and reasonable decoupling/independence between the three elements. Fig. 4.16 (b) also shows the simulated cross-polarization pattern for monopole M2 on the square system with a maximum cross polarization discrimination of 35 dB; similar values are achieved for the other elements.

Fig. 4.17 (left) presents the simulated coupling between each monopole for the square antenna system, where a maximum mutual coupling level of -15.7 dB is seen at 2.4 GHz. To further evaluate the antenna diversity performance, envelope correlation coefficients (ECCs) are

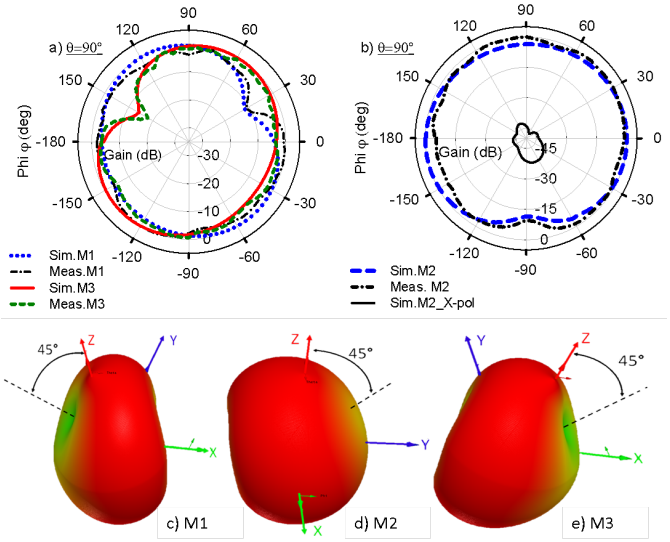

Figure 4.16: Square Antenna - Simulated and measured normalized gain pattern (X-Y cut) : M1-M3 (a), M2 (b), and simulated 3D gain pattern for each polarization M1(c)-M2(d)-M3(e).

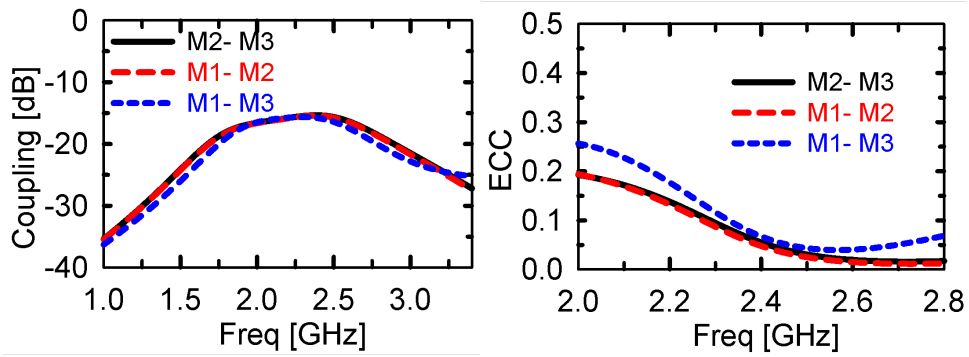

Figure 4.17: Square antenna - Simulated coupling between elements (left), envelope correlation coefficients (right).

computed between each element from simulated far field radiation patterns [81]. ECC values up to a threshold limit of 0.5 are often considered as acceptable [82, 83], while values of zero and one would suggest complete uncorrelation or overlapping radiation patterns, respectively. The proposed square antenna demonstrates low correlation between all polarizations, with a maximum ECC value of 0.05 in the ISM band of 2.4-2.5 GHz, as shown in Fig. 4.17 (right).

Similarly, Fig. 4.18 (a) and (b) illustrate the measured and simulated radiation gain patterns of the circular antenna system at 2.4 GHz for monopoles M1, M3 and M2, respectively. The data correspond to the antenna azimuth plane against a vertically oriented transmitter horn antenna,

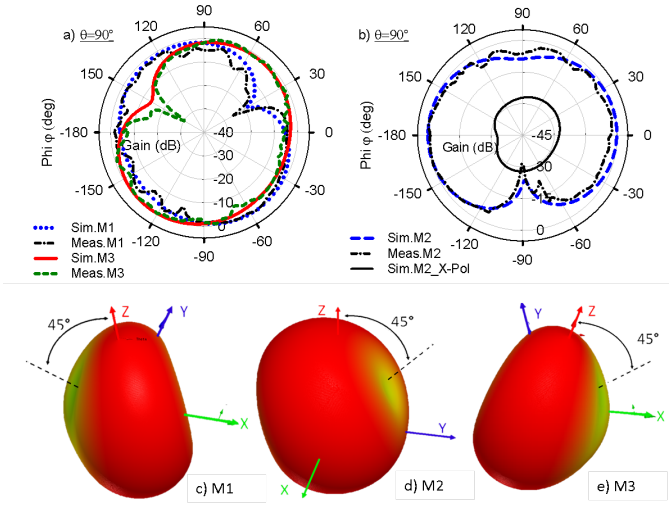

Figure 4.18: Circular antenna - Simulated and measured normalized gain pattern (X-Y cut) : M1-M3 (a), M2 (b), and simulated 3D gain pattern for each polarization M1(c)-M2(d)-M3(e).

and show good agreement between measured and simulated traces. Fig. 4.18 (c-e) show the simulated 3D gain pattern when each individual monopole is selected; as in the previous design, it is seen how each radiation null is aligned in the direction of the corresponding monopole, ensuring pattern orthogonality and reducing the mutual coupling between arms. Some ripples observed on the X-Y plane measured radiation patterns can be attributed to the presence of the SMP connector on the top surface; its placement may be switched to the bottom surface in order to reduce scattering. Fig. 4.18 (b) also shows the simulated cross-polarization pattern for monopole M2 on the circular system with a maximum cross polarization discrimination of 25.8 dB, and again similar values are achieved for the other elements.

A return loss greater than 20 dB at 2.4 GHz is achieved for all three monopoles, with a worst case 10 dB bandwidth from 2.19 GHz to 2.56 GHz (i.e., 370 MHz). Slightly higher correlation coefficients are observed for the circular system as compared to the square system, with a maximum ECC value within the 2.4-2.5 GHz ISM band of 0.159. The increase can be attributed to non-orthogonal field components created by meandered traces on each monopole. Similarly, the simulated coupling between elements on the circular antenna system shows a maximum level of -13.5 dB at 2.4 GHz.

4.2.4.2 Antenna Performance in Multipath Environments

The anechoic chamber results presented in Section 4.2.4.1 represent those expected in terms of functionality for an array of monopoles (albeit that our design has these oriented mutually orthogonal in three dimensions). However, in terms of performance of the antenna system for its intended application (i.e., IoT devices in cluttered environments), a more representative test environment is required. For this, we employed a compact (0.9 m $\times$ 0.9 m $\times$ 0.3 m) reverberation chamber (Fig. 4.19), capable of emulating channel conditions ranging from benign (i.e., Rician, high K) to very severe (i.e., two-ray, hyper-Rayleigh) [84]. As reverberation chambers have been shown to emulate channel characteristics similar to industrial sites [53], we contend our test environment will similarly emulate conditions that may be seen by M2M systems.

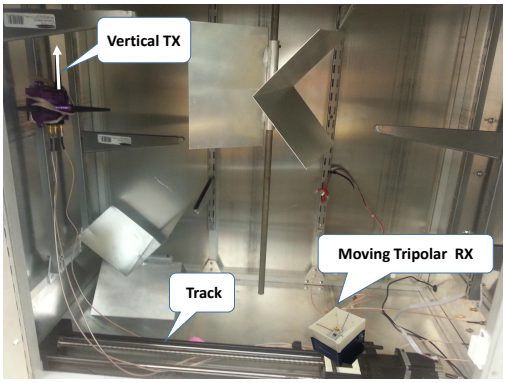

Figure 4.19: Test setup inside highly reflective, compact reverberation chamber.

Figs. 4.20 (left) and (right) show the reflection (S_{11}) coefficient for the monopoles M3 'square' and M2 'circular', respectively, inside an aluminum reverberation chamber (solid line) for a fixed stirrer position. Although the measured return loss is strongly affected by the antenna placement and conditions inside the chamber, the impedance match is still preserved at 2.4 GHz, moreover the overall frequency response follows the trend of the anechoic coefficient shown with the dashed line [85].

Chamber testing was conducted by placing each individual tripolar array mounted on a LabView controlled linear track that allowed positioning to one of 50 repeatable locations in 1 cm (i.e., $< \lambda/10$) increments. An Anritsu MS2036A vector network analyzer was then used to measure S_{21} (i.e., path loss) between a vertically polarized (i.e., Z-oriented) transmit antenna

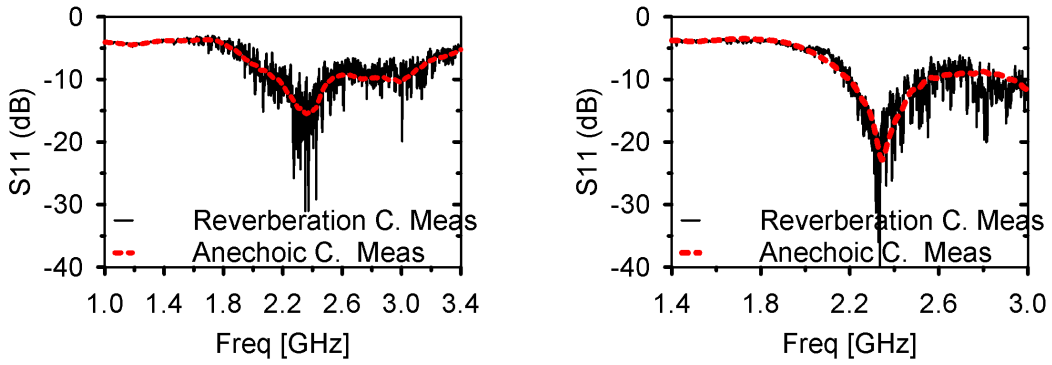

Figure 4.20: S_{11} data in reverberation chamber for square antenna (left) and circular antenna (right).

and one element of the receive tripolar array.

Measurements (Fig. 4.21 (left)) and (Fig. 4.22 (left)) were made at 551 frequencies in the range of 2.40 GHz to 2.48 GHz and at 50 positions inside the chamber. For the 'square' antenna, the individual links have comparable characteristics with median losses ranging from approximately 39.7 to 40.3 dB. Thus, over 25,000 test conditions, we found that no single element (M1, M2, or M3) exhibit any superior performance over the other two.

Also implemented was $M = 3$ selection diversity where the best (i.e., lowest link loss) path was selected for each frequency. The resulting cumulative distribution function (CDF) is seen in Fig. 4.21 (right). This diversity technique yields 1% link improvement of 11 dB. The value is significant in that it could be traded for reducing transmit power by an order of magnitude, thereby saving node energy and extending battery life or be leveraged to reduce the link outage probability and/or BER (as we demonstrate later).

The results obtained from the circular antenna shows that the individual links have comparable characteristics with median S_{21} ranging from approximately -36 to -37.5 dB. Employing selection diversity among the three elements improves the 1% link margin by 14 dB (Fig. 4.22 (right)), again, a significant improvement in overall link characteristics.

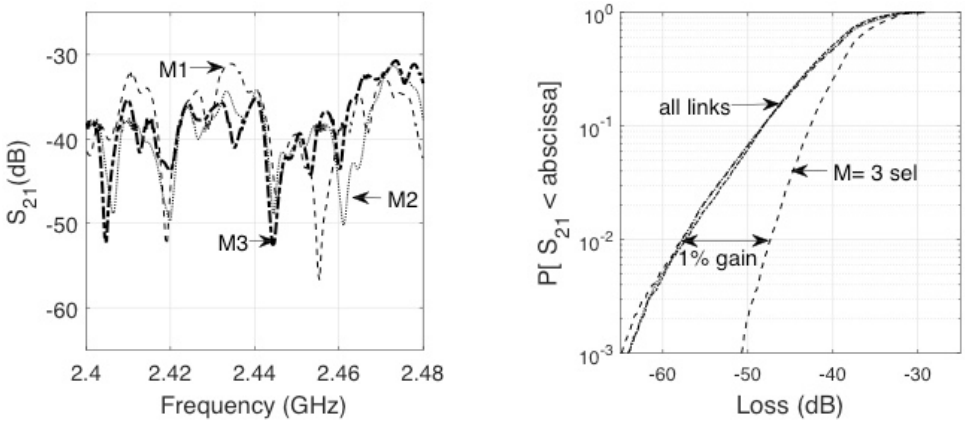

Figure 4.21: Square antenna results. Link loss, i.e., S_{21}, for three mutually orthogonal receive elements when transmit element is vertically polarized (left). CDF plots of S_{21} data for individual elements and when $M = 3$ selection diversity is leveraged. 1% link improvement is found to be $\sim$11 dB (right).

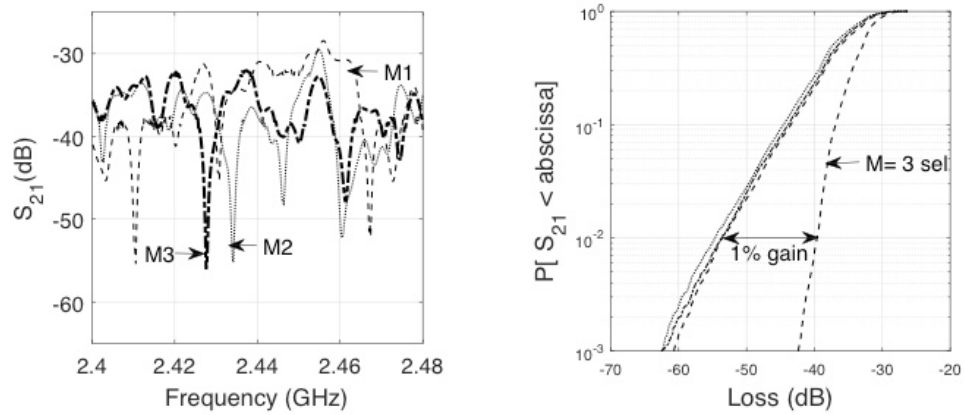

Figure 4.22: Circular antenna results. Link loss, i.e., S_{21}, for three mutually orthogonal receive elements when transmit element is vertically polarized (left). CDF plots of S_{21} data for individual elements and when $M = 3$ selection diversity is leveraged. 1% link improvement is found to be $\sim$14 dB (right).

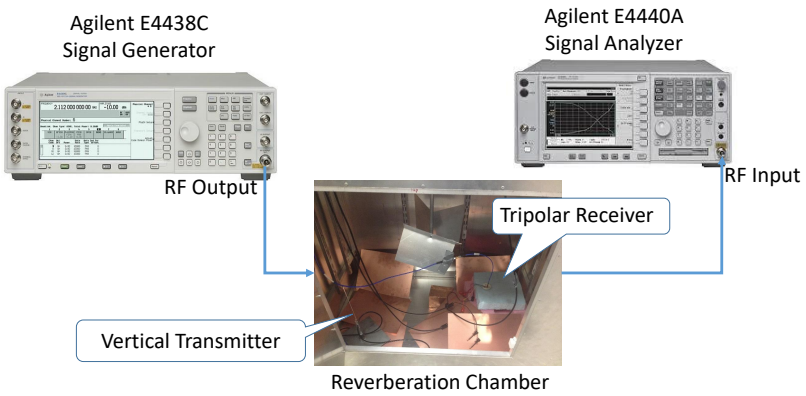

Figure 4.23: Test setup for BER measurements.

4.2.5 BER Measurements

Transmission over a link in a wireless network is prone to error due to noise and multipath effects. Bit error rate (BER) is often used to evaluate the link quality. BER has also been employed as a performance metric for routing protocols in wireless sensor networks [86, 87].

To understand how the tripolar antenna system might improve BER in very harsh environments, over-the-air BER measurements were performed in the reverberation chamber. The measurement setup for obtaining the BER is shown in Fig. 4.23. Unlike the previous S_{21} over-the-air measurements that were taken at 50 locations and 551 distinct frequencies, the BER measurements were conducted for one configuration of transmit and receive antenna array and at 16 channels with bandwidths of 375 kHz in the range of 2.4 GHz to 2.48 GHz. A vector signal generator (Agilent E4438C) was used to generate BPSK modulated signals with symbol rate of 250 kb/s. To receive and demodulate the signals, a vector signal analyzer (Agilent E4440A) was employed.

In order to measure the BER, the received bits were compared with transmitted bits. These measurements were made 1000 times. The BER graphs at $E_b/N_0 = 20$ dB for three antenna links over channel frequency, which are presented in Fig. 4.24, indicate frequency selectivity of the channel. Theoretical BER values for Rayleigh channel and Rician channels with two different K values are plotted in order to see qualitative effects. The lowest BER among three links is selected at each frequency and shown in Fig. 4.24. The data are summarized in Table 4.1. We

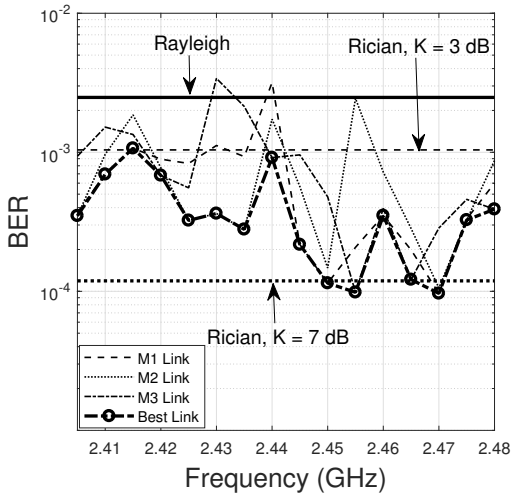

Figure 4.24: BER of three links and the best link of the square tripolar antenna.

Table 4.1: Statistics of BER of square tripolar antenna

Link	**Min**	**Mean**	**Max**
M1	9.6×10^{-5}	7.0×10^{-4}	3.2×10^{-3}
M2	1.1×10^{-4}	7.6×10^{-4}	2.4×10^{-3}
M3	9.8×10^{-5}	9.2×10^{-4}	3.4×10^{-3}
Best	9.6×10^{-5}	4.0×10^{-4}	1.1×10^{-3}

find that employing diversity methods for this particular measurement scenario decreased the average BER by 42% compared to leveraging just any single element.

The same BER measurement protocol was repeated for the circular antenna, the results of which are presented in Table 4.2. In this case, the average BER decreased by 44% when employing this tripolar antenna. It should be noted that the nominal $E_b/N_0 = 20$ is a relatively robust channel and that greater improvement can be expected at lower E_b/N_0 values.

4.2.6 Sensor Node Integration

The S_{21} measurements (Section 4.2.4) and BER data (Section 4.2.5) have shown experimentally that the prototype tripolar antennas provide an effective means of mitigating frequency and space dependent multipath effects in highly reflective communication environments. In this section, we

Table 4.2: Statistics of BER of circular antenna links

Link	**Min**	**Mean**	**Max**
M1	1.1×10^{-4}	1.8×10^{-3}	4.7×10^{-3}
M2	2.0×10^{-4}	1.9×10^{-3}	6.2×10^{-3}
M3	1.0×10^{-4}	1.9×10^{-3}	6.5×10^{-3}
Best	1.0×10^{-4}	1.0×10^{-3}	3.8×10^{-3}

demonstrate results of integrating our prototype antenna system with a commercially available wireless sensor node (Fig. 4.11 (right)). Specifically, we leverage the ability of the node's wireless chipset to provide its received signal strength indicator (RSSI) measurement. We use RSSI to infer path loss, akin to our S_{21} data, as it provides a relative dB value of the received signal strength.

As noted at the onset of this work, the prototype antenna systems were physically designed to be integrated with commercial wireless sensor nodes. The nodes in mind during the development were the LORD Sensing G-Link2 for the square antenna and the LORD Sensing G-Link-200-8G for the circular design. In our demonstration, RSSI data is captured using the square antenna, integrated with firmware from a LORD Sensing WSDA-Base-104 gateway/basestation. The firmware was developed and the experiment was run using a Silicon Labs Mighty Gecko EFR32MG development board. This board is designed to operate at 2.4 GHz with a maximum power of 13 dBm. A test script was then written using LORD Sensing's open source MSCL library. The script successively pings the node 50 times, saves the average RSSI value, repeats the process for each antenna element, and then repeats the process for each channel frequency (LORD Sensing wireless networks use 16 channels between 2.40 and 2.48 GHz).

The integrated system was placed in the reverberation chamber, connected to the SL board with the basestation firmware, and a link is established with a LORD Sensing G-Link2 with the line-of-sight blocked (Fig. 4.25). Applying selection diversity using this tripolar antenna improves the RSSI measurements substantially (Fig. 4.26), with the supporting statistics displayed in Table III. From Table III it can be seen that selection diversity between the three antenna elements improves the median RSSI 10 dB from the "worse" performing antenna element (M2). Selection diversity also provides "flatter" (i.e., more consistent) performance across the channels

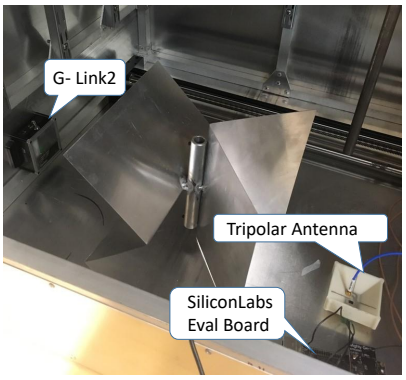

Figure 4.25: The set-up for the RSSI experiments. The LORD G-Link2 is present on the left of the chamber, while the tripolar is on the right, with the LOS component blocked.

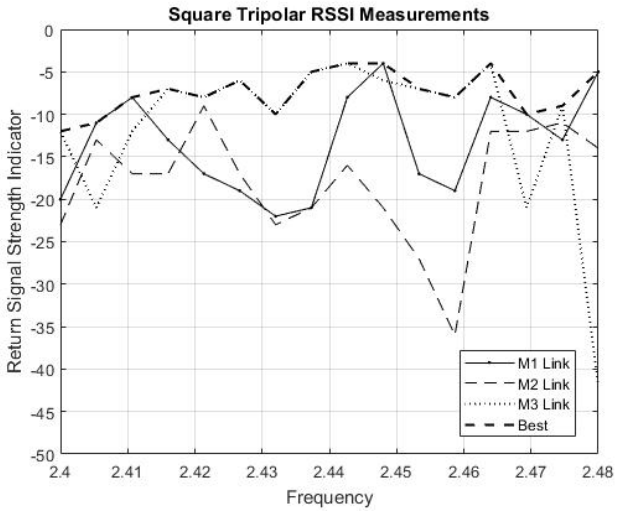

Figure 4.26: RSSI data captured within the reverberation chamber. The measurements taken at each antenna element are displayed, along with the 'best' scenario that could be attained with selection diversity.

(Fig. 4.26) as there is between 3 to 6 dB decrease in standard deviation when compared to the individual elements.

4.2.7 Conclusion

Two distinct 3D printed tripolar antennas have been developed and characterized for operation at 2.4 GHz. Each antenna is fabricated through additive manufacturing techniques to match the geometries of commercial wireless node packages. The antenna systems are designed to

Table 4.3: RSSI Data (Square Antenna System)

Link	**Median**	**Standard deviation**
M1	-13 dB	5.93 dB
M2	-17 dB	6.94 dB
M3	-8 dB	9.66 dB
Best	-7.5 dB	2.59 dB

mitigate harsh channel conditions by implementing polarization diversity between three mutually orthogonal ($\sim \lambda/4$) monopoles. Performance was demonstrated under ideal and high multipath conditions, showing return loss values greater than 15 dB at the frequency of interest. Over the air testing demonstrated a 1% channel improvement of up to 14 dB across over 500 locations in a multipath environment and 44% reduction in BER at a representative location. Additionally, full integration with commercial hardware was performed resulting in the antenna array's capability for providing more consistent conditions over all selectable communication frequencies/channels. Future work includes developing on-chip mm-Wave multipolar antenna systems fabricated with additive manufacturing and laser machining to diminish depolarization effects present in wireless chip-to-chip communication channels.

5 Geometry-based Stochastic Channel Model and Quad Polarization Diversity

Foreword

This chapter evaluates circular polarization performance and hybrid polarization diversity (a diversity technique that chooses the best signal among both linear and circular polarizations) in indoor channels. Section 5.1 presents the paper submitted to "2018 IEEE Transaction on Antennas and Propagation". A geometrical stochastic channel model (GBSCM) is proposed for indoor radio channel with ability of incorporating different polarization types (e.g., linear, circular, elliptical). To date, these evaluations have been largely through experiments and ray-tracing simulation tools and have primarily focused on linearly polarized systems. Two metrics of 1% link margins and cross-polarization discrimination (XPD) are obtained from both simulated and empirical data and show comparable results (within 1 dB). Section 5.2 presents the paper submitted to "2018 IEEE Antennas and Wireless Propagation Letters". In this paper, we report effects of using quad-polarization diversity antenna systems in harsh multipath environments to mitigate deep fading. The antenna is designed and fabricated by our collaborator at Dublin Institute of Technology. The results demonstrate that choosing between four different polarizations, while using simple low-cost omnidirectional antennas leads to substantial benefit in high-multipath environments.

5.1 A Geometric Scattering Model for Circularly Polarized Indoor Channels

5.1.1 Abstract

Wireless systems are being deployed in evermore complex environments, ones that can introduce multipath resulting in not only severe frequency selective fading but also signal depolarization. Polarization diversity is a known technique to mitigate such fades. To date, primarily linear polarization (LP) systems have been used for indoor communications, but recently circular polarized systems have received attention. As such we are motivated in this work to better under-

stand how both linear and circular systems perform in depolarizing environments. In this work, we present a 3D geometry-based stochastic channel model (GBSCM) for dual-polarized systems to evaluate circular and linear polarization in cluttered settings. Using a Poisson distribution, the model generates a number of multipath scatterers. Measurements have been conducted at 2.4 GHz to validate the model. Leveraging parameters extracted from measured data, linear and circular polarization conditions are simulated for both line-of-sight (LOS) and non-LOS (NLOS) conditions. Cross-polar discrimination (XPD) and 1% link margins are considered as performance metrics. These metrics applied to both simulated and empirical data are both within 1 dB of each other [6].

5.1.2 Introduction

Machine-to-machine (M2M) communication promises to form a significant portion of future wireless systems and will push deployments into evermore cluttered environments that are likely to produce non-line-of-sight (NLOS) and/or severe multipath conditions (e.g., factory floors). For linearly polarized (LP) links, these environments are known to change polarization plane of the transmitted wave, so the best orientation for the receive antenna is not always evident [12]. In this work, we investigate circular polarized (CP) antennas in these environments.

Other works has shown the benefit of CP-CP systems (i.e., a link where both antennas are circularly polarized) over LP-LP systems.

For instance, CP-CP links were shown to reduce delay spread in LOS indoor channels at frequencies of 1.3 and 4 GHz [88]. The simulated model presented in [89] confirmed these results and showed a reduction of delay spread by half when using circular polarization at 10 GHz. The same result has been seen at 60 GHz [90]. Finally, lower BER was observed for circular polarization in LOS conditions at 60 GHz using both experimental data [90] and simulation data [91]. Furthermore, LP-CP links were found to perform better than LP-LP when there was LOS in an outdoor environment, whereas the superiority became insignificant with obstructed LOS path and abundant number of scatterers [92]. In a system with dual-linearly polarized receiver, higher diversity gain was achieved by replacing a LP transmitter with a CP

[6] Golmohamadi, M.and Frolik, J.. Submitted on December 28, 2018. A geometric scattering model for circularly polarized indoor channels. IEEE Transactions on Antennas and Propagation.

transmitter [93].

The aforementioned works have compared CP-CP and CP-LP links with LP-LP links in different environments using either empirical data or ray-tracing simulation. Alternatives are geometric-based stochastic channel models (GBSCM) that characterize a channel independent of antenna aspects, and thus, are suitable candidates for developing multi-polarized channels. These models are simplified ray-tracing approaches in which scatterers are specified by spatial distributions which are described using parameters that are extracted from experimental measurements [24].

There are precedents for the modeling of indoor radio channels using geometry-based techniques. A 2D elliptical model was introduced for personal communication systems in [29]. The elliptical model was extended to a 3D spheroidal channel model for simulating indoor radio channels. Closed form distributions of angle-of-arrival (AOA) and time-of-arrival (TOA) showed good agreement with the distributions of empirical data in an indoor setup [3]. Furthermore, geometrical reference models have been developed for multi-polarized mobile to mobile (M2M) and fixed to mobile (F2M) channels to calculate cross-polarization discrimination (XPD) in three dimensions [28]. However, these works only considered linear polarization systems.

Here, we develop a GBSCM for indoor channels which is able to evaluate different polarization types (linear, circular, elliptical). Specifically, we combine the techniques proposed in [3] and [28] and develop a new approach that incorporates antenna polarization types within the channel model in order to describe propagation characteristics of CP waves in indoor radio channels. Note throughout this paper, we use CP and LP for CP-CP and LP-LP links respectively. Finally, we use the proposed geometrical channel model to study depolarization effects of CP and LP systems by computing XPD and also 1% link reliability margins as metrics. To best of our knowledge, non-linear polarized systems has not been considered to date. To summarize, the proposed geometrical channel model

- accounts for channel depolarization as a result of reflection effects;
- is able to estimate the impact of different polarization diversity types on mitigating fading in indoor channels.

The content of this paper is organized as follows. In Section 5.1.3, the CP polarization and

depolarization mechanisms are presented. The geometrical model is explained in Section 5.1.4. Model validation and measurement setup are addressed in Section 5.3.1. The results are discussed in Sections 5.3.2 and 5.3.3. Conclusions and avenues for future work are summarized in Section 5.3.4.

5.1.3 Wave Depolarization

In this section, we review relevant foundation for analyzing depolarization. Polarization can be explained such that at a fixed point in space, the electric field of an electromagnetic wave outlines an ellipse in a plane perpendicular to the propagation direction [23].

When horizontal and vertical components are in phase, the polarization is linear. In case of $\pi/2$ radians phase difference between equally weighted orthogonal polarization components, the ellipse transforms to a circle which represents circular polarization. In particular, the unit vectors of right hand circular polarized wave (RHCP) and left hand circular polarized wave (LHCP) are given by:

$$RHCP = \frac{\sqrt{2}}{2}(\hat{H} - j\hat{V}) \tag{40}$$

$$LHCP = \frac{\sqrt{2}}{2}(\hat{H} + j\hat{V}) \tag{41}$$

where, $\hat{H}$ and $\hat{V}$ are unit vectors of horizontally and vertically polarized waves, respectively.

Depolarization is defined as coupling of a wave into an orthogonal polarized wave due to reflection, scattering, or diffraction. In an ideal environment (i.e., free space), both the propagation direction and the polarization ellipse remain constant at each point in space, leading to zero depolarization. Whereas in a multipath environment, these two parameters randomly change over time/frequency/space and cause depolarization [30].

For simplicity, we only consider depolarization effects due to reflection off a smooth surface. This assumption roots from the fact that in indoor radio channels at frequency of 2.4 GHz, surfaces can be mostly considered smooth in the sense of Rayleigh criterion [94]. Because the electromagnetic wave is transverse, the field incident onto the interface can be decomposed into two polarization components, one parallel polarization with the electric field vector inside the plane of incidence (a plane that contains incident and reflected waves), and the other one per-

pendicular polarization, normal to that plane [95]. Magnitude and phase of reflection coefficient of them are different. Decomposition of incident waves into these two polarization modes is described in Appendix A.

5.1.4 Model Development

In this section, the geometry of the model and the distribution of scatterers will be discussed.

5.2 Physical Propagation Process

The 3D spheroidal geometry used in this paper has been previously proposed for indoor channel characterization (Fig. 5.14(a)) [3]. That work assumed that scatterers are distributed uniformly inside the volume with uniform phase distribution. Furthermore, the scatterers were treated as perfect conductors such that reflection coefficients of parallel and perpendicular polarizations were identical and unity in magnitude. However, in this paper, we have developed a model that takes polarization differences into account and calculates phase shifts of multipath components due to both reflection phenomenon and path length. This allows us to compare CP systems with LP ones. Because reflection induces a phase difference between the two orthogonal polarization components that sometimes better suppresses multipath components in CP systems compared to LP systems.

A horizontal cross-section of proposed 3D spheroidal model is presented in Fig. 5.14(b). The geometry has been divided into several sub-regions such that each sub-region is representative of a tap in tapped delay line channel model. These divisions let us to include bandwidths of measurements in the model by varying width of the sub-region.

Receive and transmit antennas are placed on spheroid's foci. A random scatterer pattern for use in our model is established as follows:

- The interval $[0, \tau_{max}]$ is divided into N consecutive sub-intervals of length $\Delta\tau = \frac{\tau_{max}}{N}$. $\Delta\tau$ is the time resolution of the system, which is equal to inverse of system's bandwidth. Bandwidth limits time resolution so that echoes at τ and $(\tau + \Delta\tau)$ arrive effectively at the same time [5]. τ_{max} is the the maximum excess delay spread of the channel.

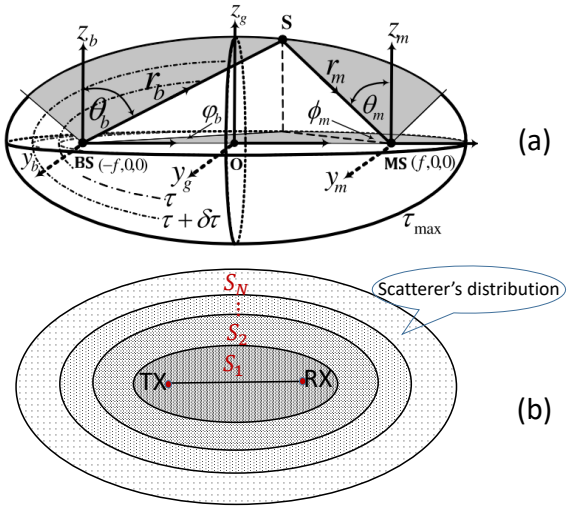

Figure 5.1: (a) Spheroid models geometry for indoor channels [3]. (b) Horizontal cross-section of proposed geometry, scatters are distributed in sub-regions $S_1 - S_N$ with different densities.

- The scatterers are distributed uniformly inside sub-regions. The most outer sub-region produces the maximum excess delay spread of the channel (τ_{max}).

5.3 Dual-polarized Channel

A multipath channel with one polarization channel can be described as a linear filter, Eq. (62), with a complex baseband impulse response for a stationary user [29]

$$h(t) = \sum_{n=1}^{N} \alpha_n \delta(t - \tau_n) \tag{42}$$

where, α_n represents complex amplitude of n^{th} component, τ_n is the relative delay of each component compared to the first arriving one, and N shows the number of taps in a tapped delay line channel model. The complex amplitude α_n is sum of all multipath signals received within the n^{th} tap or sub-region. The frequency transfer function is given by the Fourier transform of $h(t)$ [96]. This can be calculated to be

$$H(f) = \sum_{n=1}^{N} \alpha_n exp[-j2\pi f \tau_n] \tag{43}$$

To characterize a dual-polarized channel, losses due to interaction with scatterers for all polarization channels, namely, $\gamma^n_{VV}, \gamma^n_{HV}, \gamma^n_{VH}$, and γ^n_{HH} are included in the model. For instance, γ^n_{VV} defines induced loss at n^{th} sub-region for vertical to vertical polarized links. Derivation of these four polarization functions for a single scatterer in the space is described in Appendix A.

$$H(f) = \sum_{n=1}^{N} \vec{E_t}^{\,H} \begin{bmatrix} \gamma^n_{VV} & \gamma^n_{VH} \\ \gamma^n_{HV} & \gamma^n_{HH} \end{bmatrix} exp[-j2\pi f \tau_n] \vec{E_r} \tag{44}$$

where, $\vec{E_r}$ is the electric field vector of the receive antenna and $\vec{E_t^H}$ is Hermitian transpose of electric field vector of the transmit antenna. Throughout this paper, we also assume all the polarization mixing is due to the channel effects, i.e., we neglect polarization leakage of antennas. However, the model is capable to consider these effects.

5.3.1 Model Validation

In this section, we first present the test setup for conducting measurements and afterwards describe extraction of model's parameters from measurements.

5.3.1.1 Test Setup

Link measurements were conducted in both NLOS and LOS conditions within a lab environment, with tables, chairs and closets (Fig. 5.2). To emulate the NLOS setting, LOS path was blocked by a large table. An Anritsu MS2036A vector network analyzer was used to measure S_{21} (i.e., path loss) between two dual-polarized patch antennas. CP an LP link measurements were made at 551 frequencies in the range of 2.40 GHz to 2.48 GHz (bandwidth of 80 MHz). To measure co-pol and cross-pol LP links, the transmitting antenna was configured to radiate vertically polarized waves and the receiving antenna was configured to both vertically and horizontally polarized radiations. To generate CP links, a 90 degree splitter was used to provide $\pi/2$ phase shift between two linear orthogonal polarized branches of patch antenna. LOS distance between antennas was set about 2 m. To emulate the random placement of the transmitting device, the receive antenna was moved to one of 20 repeatable locations in 1 cm (i.e., $< \lambda/10$) increments in direction orthogonal to the wave propagation. The environment was kept static during measurements.

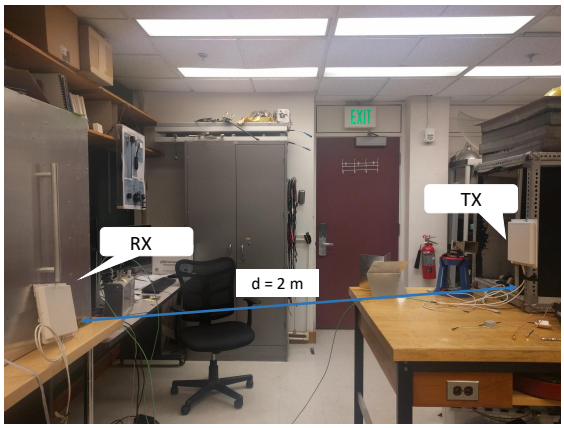

Figure 5.2: Test setup for LOS "office" conditions.

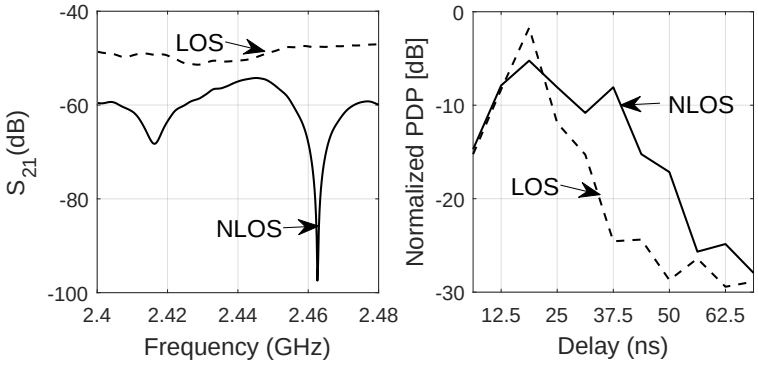

Figure 5.3: Left: Copol S_{21} in dB for vertically polarized transmit antenna. Right: PDP of measured S_{21}.

Fig. 5.3 shows frequency responses and the corresponding normalized power delay profile (PDP) at one position for LOS and NLOS conditions. For the LOS scenario, the frequency response is almost flat over the whole bandwidth. Furthermore, PDP falls off very quickly which indicates that first arriving rays carry a significant portion of the received power. However, in NLOS situation, channel shows a frequency-selective behavior. The deep fading seen in this scenario corresponds to multipath and the large excess delay spread in comparison with LOS condition.

The model's parameters are maximum excess delay spread, width and number of sub-regions. We used PDP of measured data to estimate these parameters. The channel impulse response

Table 5.1: Measured excess delay and number of sub-regions

Set-up	**Maximum excess delay**	N
LOS-VV	23 nsec	2
NLOS-VV	49 nsec	4

was made by taking the IFFT of the measured frequency data. The PDP then was derived from the impulse channel response and was normalized such that the area under PDP was equal to unity. Maximum excess delay spread of the channel was estimated by counting all components that were within 15 dB of the strongest multipath component. Average value of excess delay over 20 positions for LOS and NLOS environments are presented in Table 5.7. The number of sub-regions, N, was estimated using ratio of maximum excess delay to the time resolution of the measurement. Time resolution of our measurement was $\Delta\tau = \frac{1}{80MHz} = 12.5$ nsec.

$$N = \frac{\tau_{max}}{\Delta_\tau} \tag{45}$$

Maximum excess delay of 23 nsec for LOS condition resulted in two sub-regions. While larger excess delay of NLOS environment led to four sub-regions for this case.

Prior works have shown that the Poisson distribution is a good fit for number of scatterers [97, 98]. So we assume that scatterers are randomly distributed inside each sub-region by following spatial Poisson process with rate or expected value of λ_n such that probability of finding k scatterers in n^{th} sub-region (S_n) is given by

$$P(k \in S_n) = \frac{\lambda_n^k e^{-\lambda_n}}{k!} \tag{46}$$

To find average number of scatterers in each sub-region, the total number of scatterers is multiplied by the ratio of sub-region's power (or power of corresponding tap in PDP) to the total received power [99].

$$\lambda_n = \Lambda \frac{P(\tau_n)}{P_{tot}}, i = 1, 2, ..., N. \tag{47}$$

where, Λ is the expected value of total number of scatterers. $P(\tau_n)$ and P_{tot} are power of n^{th}

Table 5.2: Model parameters used in simulation

Set-up	λ_1	λ_2	λ_3	λ_4
LOS-VV	18	2	-	-
NLOS-VV	16	2	1	1

tap in PDP and total received power, respectively.

Since reported values for number of multipath components in a channel are dependent on measurement bandwidth and receiver sensitivity, it is challenging to find an accurate estimation for number of scatterers in indoor settings. However, a meaningful range for number of multipath components can be derived from various studies in which they have used different measurement parameters. Statistical analysis of the data taken in factory buildings with time resolution of 7.8 nsec showed a range from 9 to 36 for average number of multipath components [27]. Indoor data with measurement bandwidth of 500 KHz and short TR-RX distances have resulted in a range of 5 to 20 for number of significant multipath components [100]. Owing to having so many multipath components in our lab setup, the average of total number of multipath components (Λ) is chosen to be 20.

Employing the method described in Eq. (47), the average number of scatterers in all sub-regions are estimated for LOS and NLOS environments. These values are presented in Table 5.2 and illustrated in Fig. 5.4. For both LOS and NLOS cases, most scatterers are distributed in the first sub-region. These scatterers are sources of multipath components that arrive within first 12.5 nsec. In LOS case, since the first arriving echo contains the strong LOS signal, density of scatterers in the first sub-region is larger than NLOS case.

Horizontal cross-section of geometrical representations of both LOS and NLOS environments are shown in Fig. 5.4.

5.3.2 Diversity Gain Results

This section presents some comparisons between the simulation results and empirical data obtained from the measurement setup. The scatterer distribution parameters are presented in Tables 5.7 and 5.2. In addition, reflection coefficients ϵ_r of the scatterers should be defined. Reflection coefficients were measured for common building materials at 2.4 GHz [101]. The measured range for ϵ_r was mostly between 2 and 7. For instance, numbers of 2.7, 3 and 2.4 were

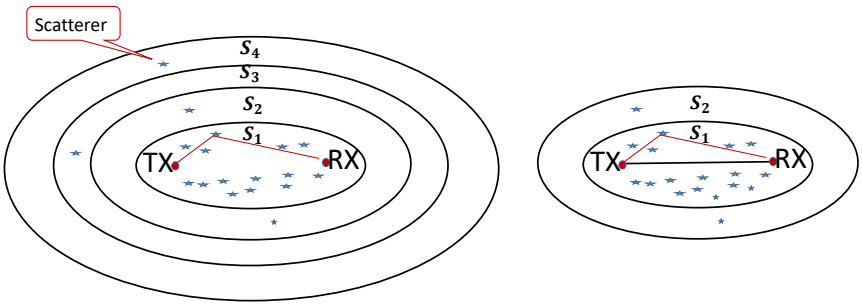

Figure 5.4: Left: NLOS scatterer's distribution geometry. Right: LOS scatterer's distribution geometry.

estimated for reflection coefficients of wood, linoleum, and drywall which exist in our indoor office environment [101]. Thus, we set the reflection coefficient ϵ_r to be 3 in our simulation.

5.3.2.1 NLOS

Fig. 5.5 shows the summarized results of measurements taken in lab when there was no LOS. We show the linear copol curve (i.e., $Copol, LP$) exhibits better performance compared to cross polarized linear link (i.e., $Xpol, LP$). However, CP shows comparable CDF curves for both copol and cross polarized links. In Fig. 5.5 we also show the CDF when $M = 2$ selection diversity is implemented for each of polarization systems. We consider the selection diversity, in which the device would choose the "best" of the receive antenna elements. That is, the device would choose the element which results in the strongest signal. In both systems, the 1% link margin was improved by 7.7 dB. That is, for 99% link reliability, the margin or, equivalently, transmit power could be reduced by over 7.7 dB if $M = 2$ selection diversity is used versus just any one of the single elements. The simulated received links were attained from our 3D geometrical model.

The CDF plots of the simulated links for five hundred realizations are shown in Fig. 5.6. All curves are normalized to median of $Copol, LP$. Again, circular polarized links showed comparable CDF curves, while linear ones provide more distinction between copol and cross-pol links. In terms of diversity gain, the simulated data showed 1% diversity gains of 7.4 dB and 8.6 dB for LP and CP systems, respectively.

A summary of measured and simulated diversity gains for both NLOS scenario are presented

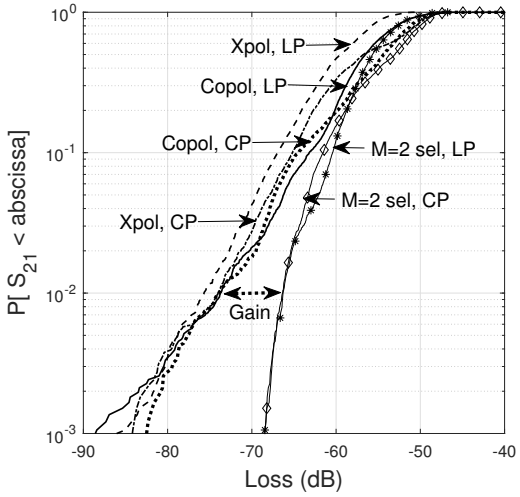

Figure 5.5: Measured S_{21} data of LP and CP links in NLOS case.

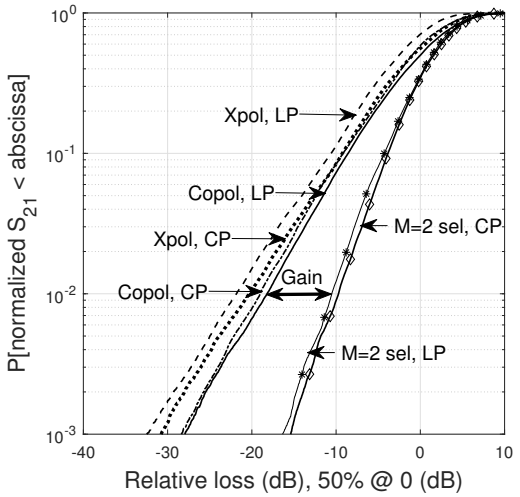

Figure 5.6: Synthesized S_{21} data of LP and CP links in NLOS case. Curves are normalized to median of $Copol, LP$.

Table 5.3: 1% Diversity Gain

Case	$gain_{data}$	$gain_{sim}$	Δ
NLOS-LP	7.7 dB	7.4 dB	0.3 dB
NLOS-CP	7.7 dB	8.6 dB	0.9 dB

in Table 5.3. The difference between measured and simulated diversity gain results are shown to be within 1 dB.

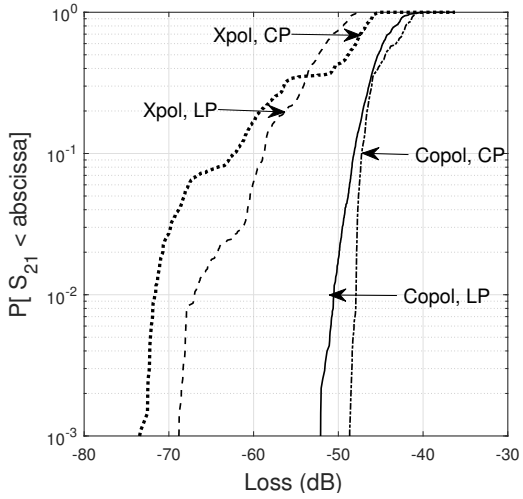

Figure 5.7: Measured S_{21} data of LP and CP links in LOS case.

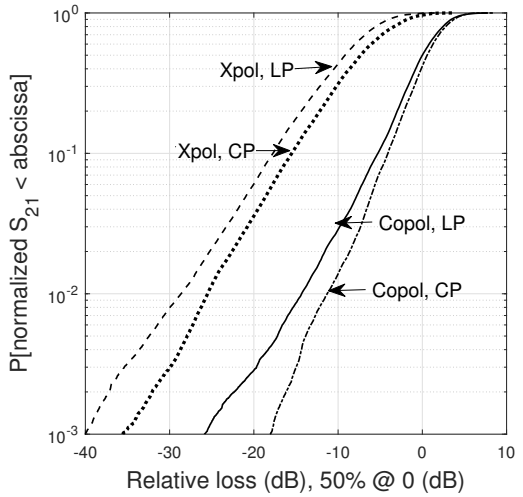

Figure 5.8: Synthesized S_{21} data of LP and CP links in LOS case. Curves are normalized to median of $Copol, LP$.

5.3.2.2 LOS

Measured data in presence of LOS showed that $Copol, CP$ links perform better than $Copol, LP$ links and provide 2.6 dB improvement of 1% link margin compared to LP link (Fig. 5.7). 3 dB enhancement of 1% link margin of $Copol, CP$ in the simulation verified the experimental result presented in Fig. 5.8.

Table 5.4: Cross polar discrimination

Case	XPD_{data}	XPD_{sim}	Δ
LOS-LP	7.30 dB	8.00 dB	0.70 dB
NLOS-LP	3.00 dB	2.64 dB	0.36 dB
LOS-CP	6.16 dB	6.90 dB	0.74 dB
NLOS-CP	0.69 dB	0.54 dB	0.15 dB

5.3.3 XPD results

Cross-polarization discrimination (XPD), which is the percentage amount of a transmitted wave that decouples into an orthogonal polarized wave, is defined as the ratio of the average power received in the co-polarized channel to the average power received in the cross-polarized channels. XPD has been formalized as follows [39, 40].

$$XPD = \frac{\langle P_{copol} \rangle}{\langle P_{xpol} \rangle} \tag{48}$$

where, for our data, $\langle ... \rangle$ denotes the average over frequencies 2.4 GHz - 2.48 GHz. Lower cross-polar discrimination indicates that antenna's rotation, which results in polarization mismatch between the transmitter and the receiver, affects the received signal strength less.

Table 5.4 presents the median of measured and simulated XPD. The results show that power imbalance between orthogonal circularly polarized waves is less than orthogonal linearly polarized waves. In the NLOS case, XPD of CP polarized waves is 0.69 dB for the empirical data and 0.54 dB for simulated data. While LP shows larger XPD in both measurements and simulation, namely 3 dB and 2.64 dB. In the LOS scenario, XPD values of CP system are also less than LP system. These results confirm that CP systems are less sensitive to antenna rotation.

5.3.4 Conclusion

We have presented a 3D geometry-based stochastic model for indoor channels capable of evaluating circular and linear dual-polarized systems. The proposed geometrical model uses spatial distributions of scatterers in a shell-like 3D spheroid to build the multipath channel. The model's parameters are obtained from measurements taken, for this work, inside an office. Analysis of the

propagation characteristics of the data has shown similarity between measured and simulated diversity gains for NLOS setting. In NLOS scenario, CP did not show significant improvement in terms of diversity gain compared to LP. However, XPD results of measurements and simulation showed less power imbalance in CP systems in comparison with LP systems. This fact causes CP systems to be less sensitive where orientation of the receive antenna changes dramatically relative to the transmit antenna. Both the experimental and simulated data proved superiority of CP polarization in the presence of LOS.

The contributions of this paper is both in geometrical model development and also in the mathematical description of channel depolarization for all types of polarized systems. It is worth mentioning that real measurements accredits this model to regenerates realistic multipath channels, and may thus be used for meaningful system analyses in indoor environments. Performance of hybrid polarized systems (e.g, LP-CP) in cluttered environments has not yet been well studied. This model can provide a practical tool for more extensive future studies in this topic.

Appendix A: Reflection from a single scatterer

Here we consider the reflection equations for a single scatterer placed in an arbitrary point in space. Assuming an incident wave has both vertical and horizontal polarizations, first, these polarizations are decomposed into perpendicular and parallel components relative to incident plane of each scatterer. Reflection coefficients for a dielectric with a reflective index of ϵ_r for perpendicular and parallel polarizations are well known and given by [102]

$$r_{\perp} = \frac{cos\theta_i - \sqrt{\epsilon_r - sin^2\theta_i}}{cos\theta_i + \sqrt{\epsilon_r - sin^2\theta_i}} \tag{49}$$

$$r_{\parallel} = \frac{-\epsilon_r cos\theta_i + \sqrt{\epsilon_r - sin^2\theta_i}}{\epsilon_r cos\theta_i + \sqrt{\epsilon_r - sin^2\theta_i}} \tag{50}$$

where, θ_i is the incident angle. Unit vectors of parallel and perpendicular polarization are then deduced from cross product of vectors. The perpendicular polarization is normal to the incident plane and consequently orthogonal to incident and reflected vectors. So, unit vector of cross product of incident and reflected vectors gives direction of perpendicular polarization as given

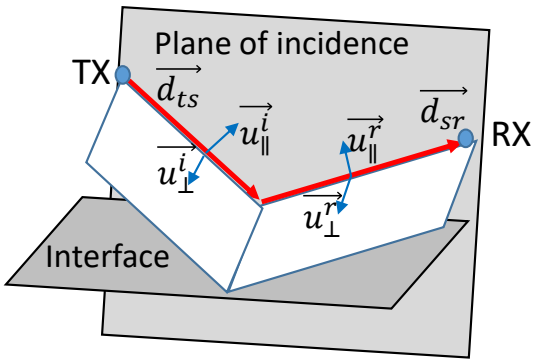

Figure 5.9: Reflection from a single scatterer

by:

$$\vec{u_{\perp}} = \frac{\vec{d_{ts}} \times \vec{d_{sr}}}{|\vec{d_{ts}} \times \vec{d_{sr}}|} \tag{51}$$

where, $\vec{d_{ts}}$ is the distance vector from transmitter to the scatterer and similarly, $\vec{d_{sr}}$ is the distance vector from scatterer to the receiver. $\vec{u_{\perp}}$ is the unit vector of perpendicular polarization for a given scatterer plane.

In a similar way, unit vectors of parallel polarization can be expressed as

$$\vec{u_{\parallel}^{i}} = \frac{\vec{u_{\perp}} \times \vec{d_{ts}}}{|\vec{u_{\perp}} \times \vec{d_{ts}}|} \tag{52}$$

$$\vec{u_{\parallel}^{r}} = \frac{\vec{d_{sr}} \times \vec{u_{\perp}}}{|\vec{u_{\perp}} \times \vec{d_{sr}}|} \tag{53}$$

where, $\vec{u_{\parallel}^{i}}$ and $\vec{u_{\parallel}^{r}}$ are unit vectors of incident and reflected parallel polarization. Vectors used in (51) and (52) are illustrated in Fig. 5.9.

Due to different reflection coefficients of parallel and perpendicular polarizations, the transmitted wave should be decomposed into these two polarizations for each scatterer plane. It can

be done using unit vectors obtained in (51) and (52)

$$\vec{V_{t\perp}} = (\vec{u_{\perp}} \cdot \vec{V_t})\vec{u_{\perp}} \tag{54}$$

$$\vec{V_{t\parallel}} = (\vec{u_{t\parallel}^{i}} \cdot \vec{V_t})\vec{u_{\parallel}^{i}} \tag{55}$$

$$\vec{H_{t\perp}} = (\vec{u_{\perp}} \cdot \vec{H_t})\vec{u_{\perp}} \tag{56}$$

$$\vec{H_{t\parallel}} = (\vec{u_{\parallel}^{i}} \cdot \vec{H_t})\vec{u_{\parallel}^{i}} \tag{57}$$

where, $\cdot$ represents inner product, $\vec{V_{t\perp}}$ and $\vec{V_{t\parallel}}$ are projections of vertical polarization into parallel and perpendicular polarizations, respectively. $\vec{H_{t\perp}}$ and $\vec{H_{t\parallel}}$ can be described in a similar way. From (54), the amplitudes of the vertical and horizontal polarization components received from a vertically polarized transmitted wave are given by

$$f_{VV} = (r_{\perp}\vec{V_{t\perp}} + r_{\parallel}\vec{V_{t\parallel}}) \cdot \vec{V}\frac{e^{j2\pi f\frac{d_{ref}}{c}}}{d_{ref}} \tag{58}$$

$$f_{HV} = (r_{\perp}\vec{V_{t\perp}} + r_{\parallel}\vec{V_{t\parallel}}) \cdot \vec{H}\frac{e^{j2\pi f\frac{d_{ref}}{c}}}{d_{ref}} \tag{59}$$

In a similar fashion, the polarization components arriving from a horizontally polarized transmitter can be written as

$$f_{VH} = (r_{\perp}\vec{H_{t\perp}} + r_{\parallel}\vec{H_{t\parallel}}) \cdot \vec{V}\frac{e^{j2\pi f\frac{d_{ref}}{c}}}{d_{ref}} \tag{60}$$

$$f_{HH} = (r_{\perp}\vec{H_{t\perp}} + r_{\parallel}\vec{H_{\parallel}}) \cdot \vec{H}\frac{e^{j2\pi f\frac{d_{ref}}{c}}}{d_{ref}} \tag{61}$$

where, $d_{ref} = d_{ts} + d_{sr}$ is the total path length and f is the carrier frequency. c denotes the speed of light.

5.4 Mitigating indoor channels with hybrid polarization diversity

5.4.1 Abstract

In this paper, we evaluate the performance of a reconfigurable, planar antenna design to mitigate frequency-selective, multipath fading. Prior work has shown that the diversity provided by two or three polarizations can significantly improve system performance. The considered antenna enables four distinct polarization, two linear that are mutually orthogonal and two circular that are likewise. Measured 1% diversity gains in a reverberation chamber and in a office were 14 dB and 11.7 dB, respectively. While the linear and circular configurations are not uncorrelated, these gains are ∼4 dB greater than gains obtained by selecting between either two orthogonal polarizations. An empirical, geometry-based stochastic channel (GBSC) model is also presented to facilitate further study of polarization diversity in such environments [7].

5.5 Introduction

Machine-to-machine (M2M) communication promises to form a significant portion of future wireless traffic and will push wireless deployments into even more severe multipath conditions (e.g., indoor industrial settings). For linearly polarized links, these environments are known to change the polarization plane of the transmitted wave, so the best orientation for a receive antenna is not always evident [12].

The work presented herein builds on prior efforts that compared the performance of *circularly* polarized (CP) communication systems with those *linearly* polarized (LP). For instance, circular polarization was shown to reduce delay spread in line-of-sight (LOS) indoor channels at frequencies of 1.3 and 4 GHz [88]. The simulation results presented in [89] confirmed the reduction of delay spread by half when using circular polarization at frequency of 10 GHz. Similar behavior has been seen at 60 GHz [90]. Finally, lower bit error rate (BER) was observed for a circularly polarized system in LOS conditions at 60 GHz using both experimental data [90] and simulation data [103].

In all above works, CP antennas were used at both the transmitter (TX) and the receiver

[7] Golmohamadi, M., Narbudowicz, A. and Frolik, J.. Resubmitted on March 6, 2019. Mitigating indoor channels with quad polarization diversity. IEEE Antennas and Wireless Propagation Letters. **in revision**

(RX) and these systems were compared to those where linear antennas were at both ends of the link. Herein, we refer these systems as CP-CP and LP-LP, respectively, for their TX-RX configuration.

Many CP diversity antennas have been proposed [104–106]. However, those CP antennas were highly-directional and thus designed primarily for LOS communications. Only recently have compact, omnidirectional circularly polarized antennas been proposed [107,108]. Such omnidirectional CP radiation can offer benefits in environments with strong multipath components arriving at various angles with no apparent LOS. This allows for new diversity schemes, i.e., hybrid polarization diversity, where the communication occurs between LP transmitter and CP receiver (LP-CP) or vice-versa (CP-LP).

Herein, we propose for the first time the polarization diversity scheme with $M = 4$, where M denotes the number of available polarization paths to switch between. Contrary to common practice, it is shown that polarization diversity can offer a performance improvement for $M > 2$. The work demonstrates the abilities of a planar, quad-polarization antenna [107] that can be configured to two mutually orthogonal linear polarizations ($+45°$, $-45°$) and two mutually orthogonal circular polarizations (right-hand, left-hand). LP-CP links are compared with LP-LP links in both a highly-reflective reverberation chamber and in an office setting. The link margin improvement is measured for $M = 4$ selection diversity. Our performance metric is the improvement seen in 1% link reliability and we find the gain to be up to 14 dB. The data are used to construct an empirical, geometry-based stochastic channel (GBSC) models for each environment to facilitate further study.

5.6 Test setup

The planar design of the antenna, to be detailed shortly, makes it readily manufacturable at low cost, thus applicable for M2M wireless devices that would deployed in cluttered environments. These devices could be configured as end nodes that communicate with a hub in a star network. It is this scenario that drives our test configurations. The transmitter (hub) used a vertically polarized off-the-shelf antenna, which is the default antenna orientation used in practice as it provides omnidirectional coverage in the azimuth plane. The receiver (end node) employs our

quad-polarization antenna [109]. Each of the four polarizations receive with the same pattern (i.e., omnidirectional in horizontal plane), which allows a fair comparison between LP-LP and LP-CP links. Both transmit and receive antennas operated at 2.55 GHz and that is the center frequency for our collected data.

To compare performances of LP-LP and LP-CP links under multipath conditions, channel measurements were conducted in two surrogate environments, one comparable to a highly reflective factory setting and the other comparable to an office setting. The measurement setup is shown in Fig. 5.10. For the former, a compact (0.9 m $\times$ 0.9 m $\times$ 0.3 m) reverberation chamber was utilized. The second environment was within a lab. Both test environments had non-line-of-sight (NLOS) conditions.

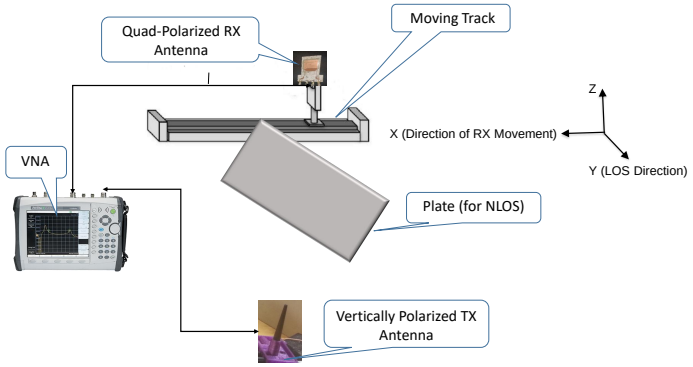

Figure 5.10: Test setup in NLOS condition. A vertically polarized antenna is used for transmitting (TX) and the reconfigurable quad-polarization antenna is used to receive (RX).

An Anritsu MS2036A vector network analyzer was used to measure S_{21} (i.e., path loss) between the vertically polarized transmit antenna and each of the four ports of the quad-polarized ($+45°$, $-45°$, RHCP, LHCP) receive antenna. Measurements were made at 551 frequencies in the range of 2.525 GHz to 2.575 GHz. The distance between antennas was set at 0.8 m for the reflective environment and 1.8 m in the office setting. To emulate the random placement of the devices, the receive antenna was mounted on a LabView controlled linear track that allowed positioning to one of 15 repeatable locations in 1 cm (i.e., $< \lambda/10$) increments. The movement of the positioner was orthogonal to the nominal TX-RX direction to help maintain a nearly constant link length.

The quad-polarization antenna leveraged in this study was previously presented in detail

in [109]. For this study, we are concerned not with traditional antenna measures (e.g., patterns) but how reconfiguring the antenna allows one to mitigate channel fading effects. In this case, the four different polarizations are obtained by using the phase shifts detailed in Table 5.5 to each of antenna's four inputs. The CP configurations are achieved by using a hybrid quadrature coupler (as in [**?**], pp. 343-347) followed by 3 dB Wilkinson power dividers (as in [**?**], pp. 328-333). Fig. 5.11(a) shows the hybrid coupler along with power dividers. The configuration for generating CP polarization is presented in Fig. 5.11(b). Fig. 5.11 clearly shows the planar design of the antenna.

Table 5.5: Phase shifts at antenna ports to generate desired configuration

Polarization	Port 1	Port 2	Port 3	Port 4
+45°	0°	-	0°	-
-45°	-	0°	-	0°
RHCP	90°	0°	90°	0°
LHCP	0°	90°	0°	90°

Figure 5.11: (a) Feed circuitry (hybrid coupler and power divider) used to generate circular polarization. (b) Antenna attached to feed circuitry that provides phasing described in Table 5.5.

5.7 Results

To analyze the diversity performance provided by the $M = 4$ antenna, we leveraged the collected S_{21} data. For each polarization in each environment, we had over 8000 data points ($frequencies \times locations$). For our diversity method, we considered the scenario where the M2M device would implement the simplest technique, selection diversity. In this method, the device chooses the "best" element among the two linear, two circular, or among all four links. In practice, a device would choose the link which results the strongest received signal strength indicator (RSSI) measurement. We show below that this approach improves the overall channel characteristics by reducing the probability of deep fades and consequently the margins needed in link budgets to maintain a desired quality of service (e.g., 99% reliability).

5.8 Experimental Results

Fig. 5.12 shows the cumulative distribution of the S_{21} data taken inside the reverberation chamber. In this environment, we find that all four links are individually statistically similar. Selecting the best link between two linearly polarized receiver branches (i.e., $M = 2$ selection diversity) led to 1% link improvement of 9.4 dB. While choosing the best of the two circularly polarized (i.e., also $M = 2$ selection diversity) resulted in 9.5 dB 1% link enhancement. These results indicate that for this environment there is no clear advantage to employ orthogonal circularly polarized antennas over orthogonal linear antennas. However, when selection diversity was implemented using all four receiver links (i.e., $M = 4$ selection diversity), 14 dB diversity gain was obtained. Thus for a bit more hardware complexity significant gains can be obtained, as illustrated in Fig. 5.11(b). We also find that the median (i.e., 50%) diversity gain to be about 2 dB for both $M = 2$ cases and a significant 4 dB when all four polarizations are leveraged.

Our results illustrate that the M paths considered in this work are not-uncorrelated. For $M = 2$ independent Rayleigh paths, the 1% diversity gain can be found to be 11.2 dB, whereas we are finding gains to be ∼9.5 dB. These empirical results indicate more paths are desirable thus making the presented quad-polarization antenna, even with its inherently non-uncorrelated paths, attractive. Our result are also significant in that the diversity gains obtained for this two-dimensional (i.e., planar), $M = 4$ design are larger than those recently obtained for a three-dimensional and more complicated to manufacture design having $M = 3$ mutually orthogonal elements [58]; i.e., 1% diversity gain 14 dB vs. 11 dB.

For the office NLOS setup, "+45°" and "RHCP" links showed slightly better link quality than "−45°" and "LHCP" links (Fig. 5.13). We see no significance in that these two particular links performed better, as this result is unlikely generalizable across other, but similar, environments. As we had for the the reverberation chamber, $M = 2$ diversity results indicate that CP and LP diversity will provide comparable (within 1 dB) 1% gain improvement (∼8 dB). However, leveraging all four polarization results in a 11.7 dB 1% link enhancement; a further 3 dB improvement. The larger diversity gain seen in the reverberation chamber can be attributed to the more severe multipath conditions and thus the resulting path responses being less correlated. Table 5.6 provides a summary of our 1% and median diversity gain results for both the chamber

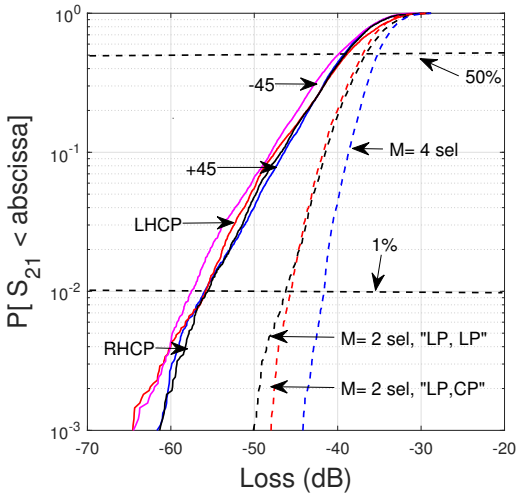

Figure 5.12: CDF plots of all links and selection diversity in reverberation chamber for $M = 2$ and $M = 4$.

and the NLOS office environments.

Table 5.6: Empirical results - 1% & 50% diversity gains

Case	**%**	**LP,** M**=2**	**CP,** M**=2**	M**=4**
Reflective chamber	1%	9.4 dB	9.5 dB	14.0 dB
Reflective chamber	50%	2.1 dB	2.1 dB	3.9 dB
Office-NLOS	1%	7.9 dB	8.7 dB	11.7 dB
Office-NLOS	50%	1.2 dB	1.5 dB	2.2 dB

5.8.0.1 Modeling results

To facilitate further study of polarization diversity in environments such as considered herein, the collected data were used to construct a 3-D geometrical stochastic model that describes wireless channels using ellipsoid sub-regions (Fig. 5.14). In this model, scatterers are randomly distributed within each sub-region S_1 to S_N according to the Poisson distribution. Each sub-region corresponds to a bin of the channel's power delay profile (PDP).

To develop our model, the inverse Fourier transform (IFFT) was calculated from the measured S_{21} data to obtain power delay profiles for both environments. Then, using the PDPs we were

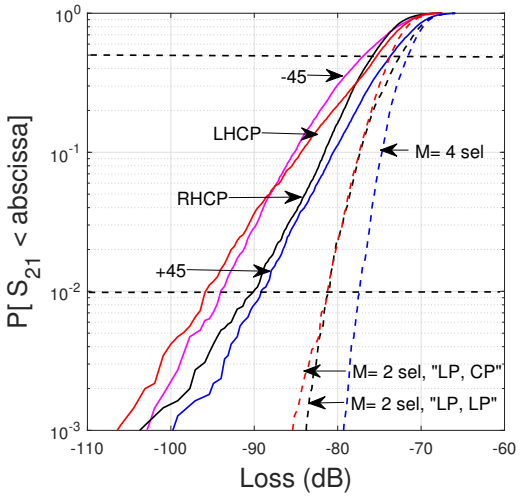

Figure 5.13: CDF plots of all links and selection diversity in NLOS condition in office for $M = 2$ and $M = 4$.

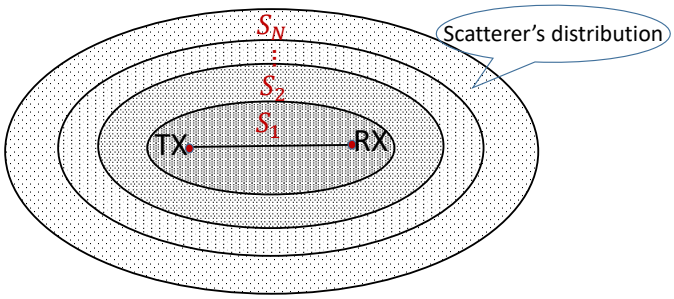

Figure 5.14: Horizontal cross-section of scatterer's distribution, scatterers are distributed uniformly in sub-regions $S_1 - S_N$.

able to determine the number of sub-regions (N) and the expected value of number of scatterers in the i^{th} sub-region (λ_i). The sum of the number of scatterers in all sub-regions (Λ) was set to 20, based on prior work for cluttered environments [99]. As our measurement bandwidth was the 50 MHz, our bin resolution in the PDP was its reciprocal, i.e., 20 nsec. We calculated expected value of the number of scatters in a particular sub-region, by taking average of received power at that sub-region's and divided it by the total PDP power. The calculated parameters for both environments are shown in Table 5.7. Based on our measured data, we found we needed $N = 9$ sub-regions to properly model the reverberation chamber. However, for the NLOS-office environment, due to its smaller excess delay, only $N = 3$ sub-regions were needed.

Table 5.7: Model parameters used in simulations

Set-up	λ_1	λ_2	λ_3	λ_4	λ_5	λ_6	λ_7	λ_8	λ_9	Λ
Reflective chamber	4	4	4	3	2	1	0	1	1	20
Office-NLOS	13	3	4	-	-	-	-	-	-	20

Fig. 5.15(a) presents synthesized S_{21} data based on our model for the reverberation chamber and Fig. 5.15(b) shows its corresponding power delay profile. The geometrical model has captured the frequency selectivity of the channel inside the chamber well as seen by comparing the CDF of Fig. 5.16 to that of Fig. 5.12. Implementing selection diversity in the modeled reverberation chamber showed that the 1% link margin could improve about 13 dB, compared to 14 dB in measured data. Choosing best of the two links for linear polarized and for circular polarized receive antennas resulted in 9.3 and 8.3 dB 1% diversity gains, respectively. This compares closely to 9.4 dB and 9.5 dB obtained empirically.

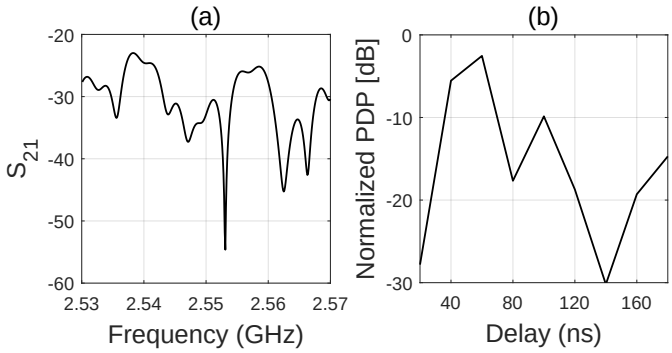

Figure 5.15: (a) Synthesized S_{21} for the modeled reverberation chamber. (b) Power delay profile obtained from the S_{21} result.

The modeled NLOS office case showed 1% link margin improvement for $M = 4$ to be 12.6 dB. Linear $M = 2$ diversity resulted in 9 dB link improvement, while $M = 2$ circular polarization diversity for this modeled environments showed 8.7 dB 1% link enhancement. These results compare favorably and respectively to 11.7 dB, 7.9 dB, and 8.7 dB in the measured data. For median diversity gain, the results obtained for our modeled environment were within 0.5 dB of those from the measured physical environment.

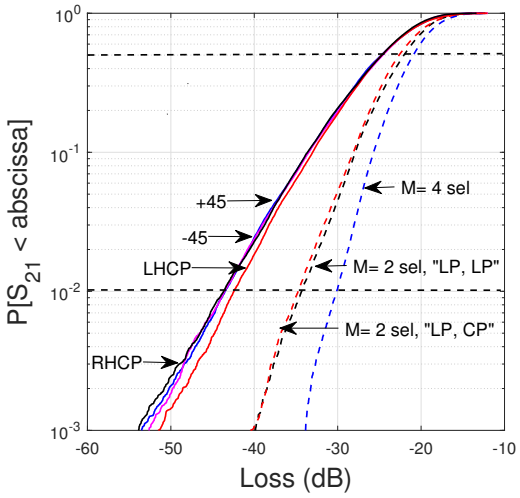

Figure 5.16: Channel statistics from modeled reverberation chamber. The metric of 1% diversity gain are within 1 dB of actual measurements found in Fig. 5.12.

5.9 Conclusion

Polarization diversity is a powerful mitigation technique especially in space-constrained applications with the presence of abundant multipath components. This paper presents a reconfigurable antenna that provides four distinct polarization paths. The planar design of the antenna lends itself to be readily manufactured at low cost and thus could be incorporated in wireless devices intended for highly cluttered environments, such as those expected for machine-to-machine applications. Experimental data demonstrated the proposed antenna offers substantial benefit in high-multipath environments. When one employs selection diversity, the 1% diversity gain in a reverberation is 14 dB and in office NLOS environment it is 11.7 dB. This gain can be traded for greater system reliability, greater transmission distances, or low transmission power to extend device battery life. Furthermore, the technique can be seemingly combined with other diversity schemes and the paper provides a geometry-based stochastic channel model to facilitate such further studies.

6 MM-Wave Channel Measurements and Characterization

Foreword

This chapter discusses channel measurements and characterization at Millimeter-wave band. Section 6.1 presents the paper as published in the "2018 IEEE International Symposium on Antennas and Propagation" [110] and discusses dual-polarized channel measurements at 28 GHz in indoor channels. Section 6.2 presents the paper as published in the "2017 IEEE International Symposium on Antennas and Propagation" [111]. This paper uses a finite-state Markov model to synthesize multipath effects over small-scale movements in harsh environments at 60 GHz.

6.1 28 GHz Channel Measurements in High Multipath, Indoor Environments

6.1.1 Abstract

Millimeter-wave (mmWave) communication systems are being proposed for a variety of short-range applications where large bandwidths are required. This work presents an experimental characterization for a dual-polarized 28 GHz indoor channel. Power delay profiles (PDPs) were measured in an indoor environment to extract site-specific multipath details [8].

6.1.2 Introduction

Millimeter-wave (mmWave) technology is eyed to meet the needs of a variety of forthcoming high bandwidth communication systems. These systems include 5G mobile, in-building, vehicle-to-vehicle, infrastructure-to-vehicle, and wireless data center networks. The mmWave spectrum provides a large bandwidth that can enable multi-Gbps data rate wireless links. The 28 and 38 GHz bands have recently become available through LMDS and LMCS auctions and are currently considered for mobile cellular. This work focuses on the former band for an indoor environment.

The channel models for mmWave systems are still nascent; measurements for indoor settings

[8] Golmohamadi, M., Chowdhury, S., Jamison, J., Kravitz, E. and Frolik, J.. 2018, July. 28 GHz Channel Measurements in High Multipath, Indoor Environments. In 2018 IEEE International Symposium on Antennas and Propagation & USNC/URSI National Radio Science Meeting (pp. 767-768). IEEE.

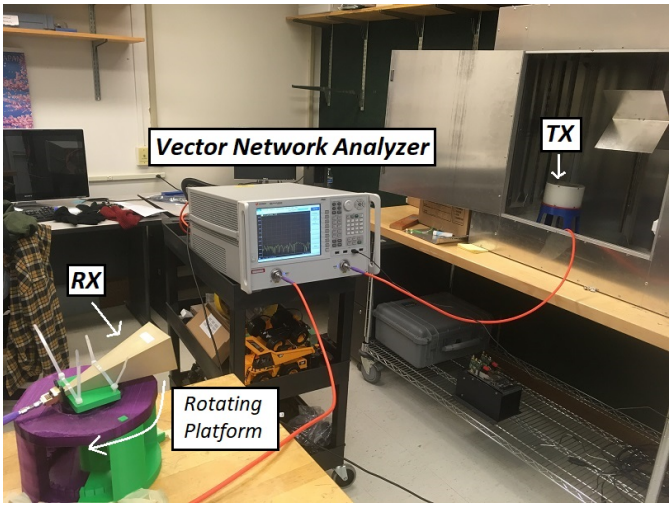

Figure 6.1: The indoor measurement environment considered in this work.

in particular have been limited. It is known that penetration loss of most materials at mmWave frequencies is high [112]. In addition directional antennas and/or adaptive beam-forming have been proposed be employed in order to establish a reliable communication link (vs. omni directional antennas that are prevalent in, e.g., 2.4 GHz systems). Furthermore, many surfaces which are assumed to be smooth in lower frequencies, are considered rough in mmWave band that cause diffused scattering which makes the wave propagation behavior more complicated.

In short, one cannot expect to apply models developed for lower frequencies. As such, this work adds to the nascent work to better understand channels associated indoor 28 GHz systems. In particular,this work presents dual-polarized channel measurements and analysis at 28 GHz in a cluttered environment.

6.1.3 Methodology

S_{21} measurements were conducted, using a vector network analyzer (Keysight Technologies N5227A), between two linearly polarized antennas placed in an office setting. The transmit antenna was a 6-dBi omni-directional antenna and the receive antenna was a directional horn antenna with 25-dBi gain. Half beamwidths (HPBW) of the horn antenna are 10° in azimuth and 9° in elevation. Omni-directional antenna has a HPBW of 10° in elevation. To model small-scale spatial fading characteristics, the transmit antenna was mounted on a LabView controlled

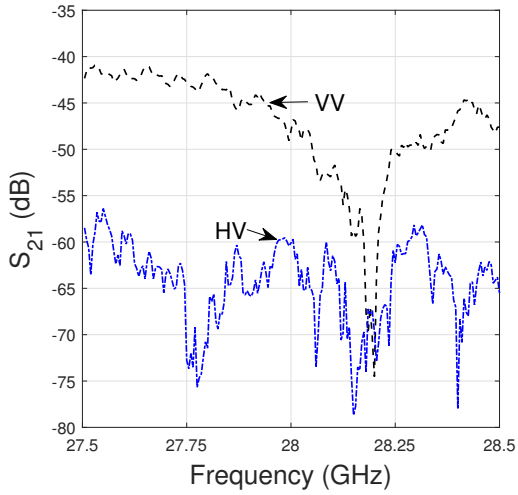

Figure 6.2: Representative copol and crosspol S_{21} data taken using the set-up illustrated in Fig. 6.1.

linear track that allowed positioning to one of 50 repeatable locations in 1 cm (i.e., $< \lambda$) increments. So at each position on the track, 36 azimuth measurements were collected to provide full azimuthal coverage.

Fig. 6.1 displays the measurement set-up used in this work. The omni-directional antenna was placed inside a reverberation chamber previously used for multipath characterization at lower frequencies [84]. The horn antenna was placed, approximately 2 m away, on a platform which could be rotated in 10° (one HPBW) increments from 0° to 360° to resolve angle of arrival (AoA) variations.

6.1.4 Experimental Results

Co-polarized and cross-polarized data were collected at 36 azimuth angles under LOS and NLOS conditions. Measurements were made at 3201 frequencies in the range of 27.5 GHz to 28.5 GHz. Fig. 6.2 shows a representative S_{21} measurement taken using this set-up, with the horn antenna at 0°, pointing directly at the omni-directional antenna. The severity of the small-scale effects present at these high frequencies in a multipath environment are evident in this measurement.

Table 6.1: maximum AoA and corresponding PDP value

Case	**First peak**	**Second peak**	**Third peak**
VV- LOS	$0°, -41\ dB$	$90°, -50\ dB$	$200°, -59‘\ dB$
VV- NLOS	$30°, -61\ dB$	$90°, -50\ dB$	$200°, -60\ dB$
HV - LOS	$10°, -62\ dB$	$20°, -64\ dB$	$210°, -68\ dB$
HV - NLOS	$30°, -78\ dB$	$90°, -74\ dB$	$200°, -70\ dB$

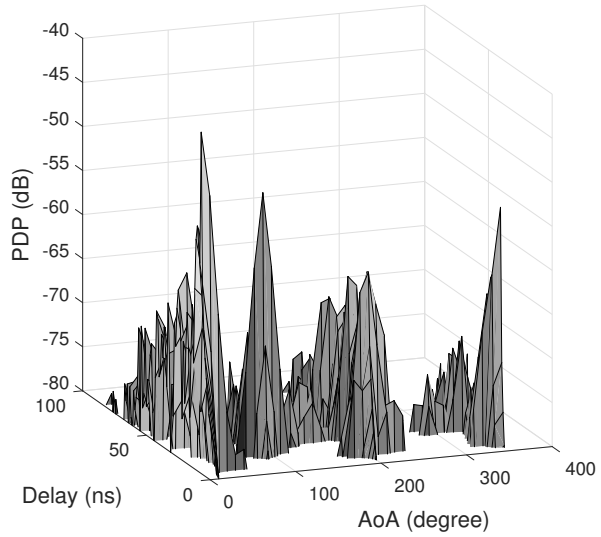

Figure 6.3: Power delay profile in 3D for LOS-VV case.

6.1.4.1 Power Delay Profile

The channel's impulse response was obtained from frequency domain data to calculate power delay profile (PDP). Fig. 6.3 and Fig. 6.4 show 3D plots of PDP over delay and AoA for LOS and NLOS conditions. For LOS case, first maximum AOA ,which is the arrival direction of the strongest multipath component at the receiver, is 0°. The next maximumm AOA is 90° that corresponds to reflected paths from a metal cabinet in the corner of the office. The first PDP peak for NLOS case occurs at 30° which is the result of diffraction from a metal surface used to block LOS path. The next peak corresponds to AoA of 90°. It can be explained by reflection from the cabinet. Table 6.1 presents the maximum AOA and their corresponding PDPs for different scenarios.

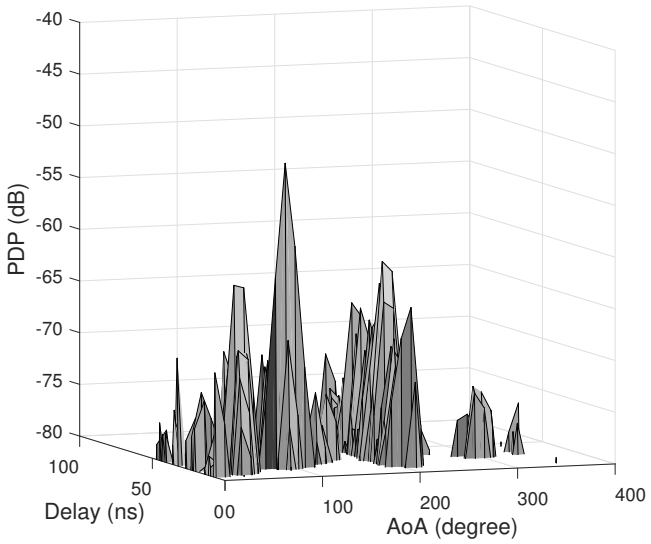

Figure 6.4: Power delay profile in 3D for NLOS-VV case.

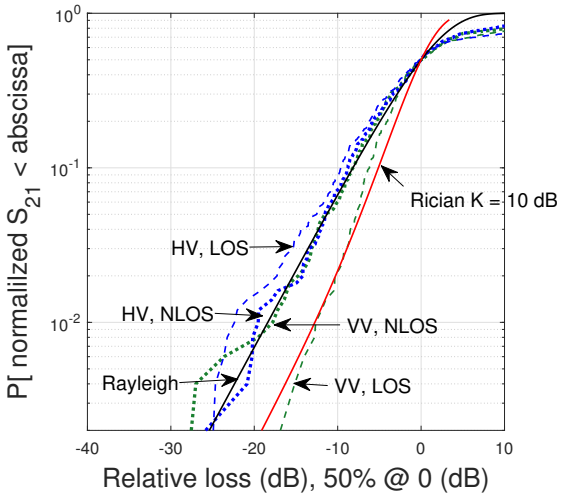

Figure 6.5: CDFs of small-scale fading in LOS and NLOS, for the cross-polarized V- H and co-polarized V- V cases at one location on the track. Rayleigh and Rician distributions are also plotted.

6.1.4.2 Small-Scale Spatial Statistics Results

The synthesized omni-directional PDP was extracted using the method proposed in [113]. Fig. 6.8 presents The empirical cumulative distribution functions (CDFs) of the normalized path loss of

Table 6.2: Cross Polar Discrimination (XPD)

Scenario	XPD
LOS	17.8 dB
NLOS	9.1 dB

omni-directional channel at one location on the track. For the V-V co-polarized data, the curves are best fitted by the the Rician distribution with K-factor of 10 dB in LOS, and the Rayleigh distribution in NLOS. For the V-H cross-polarized data, both the LOS and NLOS CDFs appear to be approximately Rayleigh. The results for cross- polarization discrimination (XPD) is shown in Table 6.2. An XPD factor of 17.8 dB for cross-polarized antennas indicates strong polarization discrimination in LOS environments. A more noticeable de-polarization effect in NLOS is confirmed by the XPD factor of 9.1 dB.

6.1.5 Conclusion

In this study, measurements of a 28 GHz indoor channel are presented and discussed. Maximum AoA is obtained for different scenarios. Furthermore, XPD factor , as a metric for depolarization effects in an environment, is estimated for both LOS and NLOS cases.

6.2 Markov Modeling of Spatial Variations in Multipath

6.2.1 Abstract

Multipath effects over small-scale movements are characterized using a finite-state Markov model. Performance of the model is evaluated by comparing statistical behavior of synthesized data with those were taken at 60 GHz inside a reverberation chamber. The proposed method allows multipath behavior prediction for new environments or frequencies in line-of-sight and non-line-of-sight situations [9].

6.2.2 Introduction

A major requirement in the design of any digital wireless system in terms of selecting modulation schemes, channel equalization techniques, and network concepts is the adequate understanding of the radio channel [25]. Predicting multipath effects by estimating the impulse response and fading rates before designing a specific system is especially of great importance for applications which are subject to operating in harsh propagation environments (e.g., cluttered factories).

Markov models have been used to address temporal variations in Rayleigh fading channels [114]. This approach has especially received attention for vehicle-to-vehicle applications where multipath components experience significant variations over time [115, 116].

However, to the best of our knowledge, Markov models have not been employed to characterize spatial changes of multipath components. So in this work, we propose a channel model based on Markov processes that captures variations of fading characteristics over small-scale movements.

6.2.3 Synthesis Method

A multipath radio channel can be described as a time-varying linear filter. Eqn. (62) presents an alternative to the channel response equation found in [115]; for time variation "t" is replaced

[9] Golmohamadi, M., Chowdhury, S. and Frolik, J.. 2017, July. Markov modeling of spatial variations in multipath. In Antennas and Propagation & USNC/URSI National Radio Science Meeting, 2017 IEEE International Symposium on (pp. 611-612). IEEE.

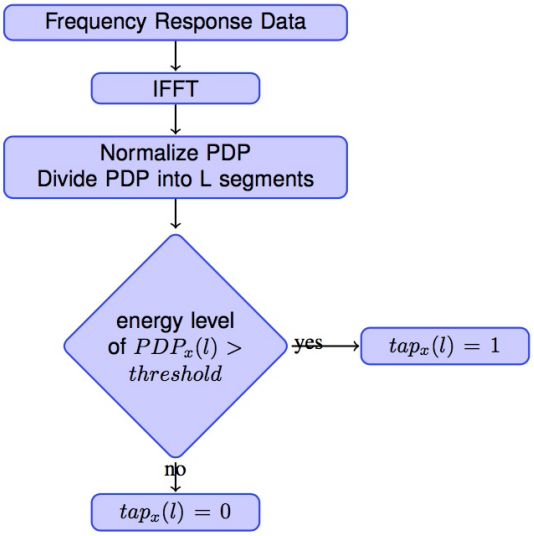

Figure 6.6: Flowchart of the Markov model.

with spatial variation "x".

$$h(x,\tau) = \sum_{p=0}^{P} z_p \alpha_p(x) exp[j[2\pi f_c \tau_p(x)]\delta(\tau - \tau_p(x)] \tag{62}$$

Where $\alpha_p(x)$ represents real amplitude of each multipath component, $\tau_p(x)$ is relative delay of each component compared to the first arriving one, and P shows the number of multipath components. The stochastic variable z_p describes appearance and disappearance of multipath components over spatial movements [115]. This formulation presumes that the environment is stationary in time and that variations are only due to the small changes in device position at time of deployment or the frequency of operation. This assumption would be valid for fixed devices deployed in relative static environments (e.g., wireless sensors).

Fig. 6.6 outlines the proposed modeling approach. An impulse response is obtained from frequency domain data. The power delay profile (PDP) is then calculated and is normalized such that the area under PDP is equal to unity. The number of taps should be predefined and will depend on the choice of environment (e.g., factory, office, etc). Each of these environments produces a different range of delay spread values which is a key factor in determining the number of taps. A rule of thumb for estimating number of taps based on distance between transmitters

and receivers and maximum delay spread of the channel is presented in [117]. To set a *threshold* value for our Markov model, PDP data has to be processed in order to reduce the impact of measurement noise. We follow the method described in [118], where a constant false alarm rate (CFAR) is achieved independent of the signal to noise ratio. The assumption is that the amplitude of this noise is Rayleigh distributed. Using this approach, we set the probability of false alarm at 10^{-3} to determine the threshold level (-32 dB). Let S = [OFF, ON] = $[s_0, s_1]$ denote set of states for taps. At each position, taps with total energy of less than the threshold value fall into the s_0 or "OFF" state and those with energy level greater belong to the s_1 or "ON" state. State transition probability (STP) and steady state probability (SSP) matrices for each tap can be defined as follows:

$$STP = \begin{bmatrix} P_{00} & P_{01} \\ P_{10} & P_{11} \end{bmatrix}, \quad SSP = \begin{bmatrix} P_0, P_1 \end{bmatrix} \tag{63}$$

Where each element P_{ij} in matrix STP is the transition probability of going from State i to State j. For instance, P_{01} describes the probability that a tap will be in "ON" state in next position, knowing that it is in "OFF" state at current location. P_0 in SSP matrix represents steady state probability of a tap to be in "OFF" state and, similarly, P_1 shows the probability of being in the "ON" state.

6.2.4 Model Validation

To validate the model, a set of S_{21} channel measurements were taken at 32 positions in a reverberation chamber. S_{21} sweeps were made between 59.5 GHz and 60.5 GHz (bandwidth of 1 GHz). The antennas were placed pointed towards each other and approximately 15 cm (i.e., 60λ) apart in a compact ($3' \times 2' \times 3'$) reverberation chamber. To illustrate the effect of small physical changes in the environment, a microstage was used to adjust the receive antenna by step sizes of 1 mm. Testing was conducted with the receiver and transmitter antennas oriented in vertical orientation. Additional elements such as metallic baffles and copper sheets were added in order to create a NLOS and highly reflective environment. An estimate of the channel impulse response was made by taking the IFFT of the measured frequency data.

Fig. 6.7 shows z_p processes associated with the fifth and eighths taps for modeling data

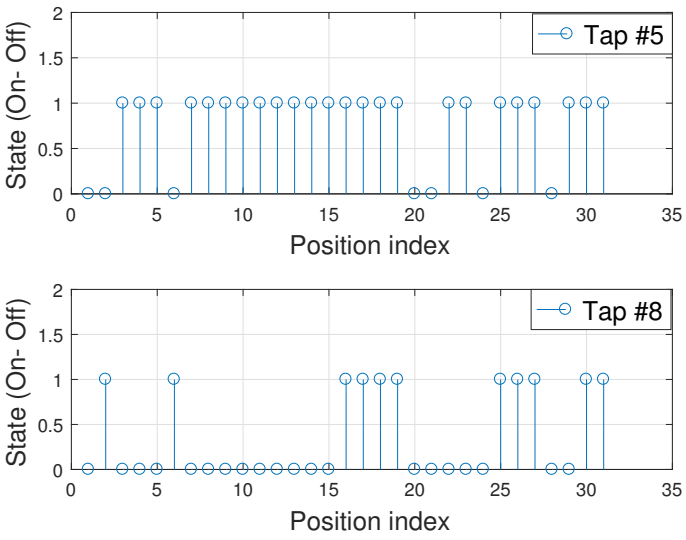

Figure 6.7: Sample persistence processes for *Taps* 5 and 8.

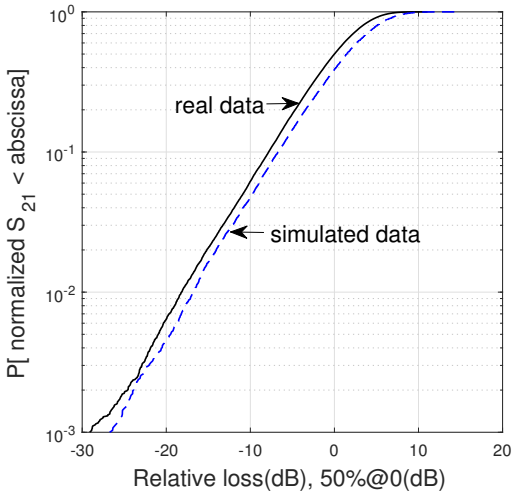

Figure 6.8: CDF of real and synthesized S_{21} at 32 positions.

inside the reverberation chamber for each of the 32 positions. $Tap-5$ is seen to be more critical in capturing chamber's environment, while $Tap-8$ provides additional variability. Cumulative distribution probability of normalized magnitude of measured and synthesized data over 32 positions (Fig. 6.8) indicates consistency between real and simulated channels.

Different fading scenarios ranging from Rician (different K values) to hyper-Rayleigh [119]

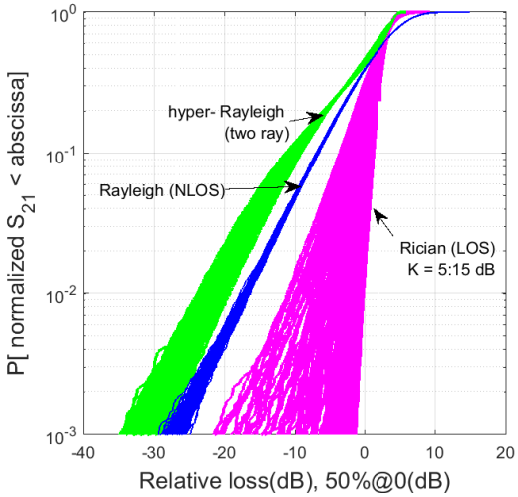

Figure 6.9: CDF of 300 possible fading scenarios simulated for the reverberation chamber environment.

were generated using synthesized tap model (Fig. 6.9). Rician fading curves represented by pink color are generated by adding LOS component to the current model. 100 distinct Rician curves are generated for different K factors ranging from 5 dB to 15 dB. 100 Hyper-Rayleigh curves that are shown with green color are generated by adding two strong destructive components to the model (using the same K but as defined in [119]). The 100 blue curves are different Rayleigh-like realizations of the synthesized model corresponding to NLOS measurements.

6.2.5 Conclusion

In this study, a Markov channel model for spatial variations in multipath environments is presented. Comparison between measurements taken at 60 GHz inside a reverberation chamber and synthesized data showed good agreement. Furthermore, the model was used to generate different fading scenarios ranging from Rician to hyper-Rayleigh.

7 Conclusion and Future Work

7.1 Summary

Machine-to-Machine (M2M) communication is widely employed in many popular wireless communication systems, such as traffic control, supply chain management, fleet management and telemedicine. The environments in which M2M systems are expected to operate may be challenging in terms of radio wave propagation due to their cluttered, multipath nature, which can cause deep signal fades and signal depolarization. A well-known approach to mitigating multipath is to leverage two antenna elements whose polarizations are orthogonal and thus fading characteristics are not correlated. The idea behind this work is to investigate the potential of tripolar antenna systems, which contain three perpendicularly oriented antennas, and to see whether these systems can be used for mitigating fading in M2M communication systems. Since the different antennas can be co-located, polarized antenna systems combine the advantages of multi-antenna systems (increased bitrate, reliability, etc.) while still maintaining a compact antenna system. The other aspect of this dissertation is developing new 3D multi-polarized channel models for wireless systems.

To understand how tripolar systems can be effective in a wireless communication channel, we need a theoretical framework for depolarization in three dimensions. Chapter 1 presents a Stokes vector-based analytical framework to study depolarization in three dimensions. This framework is applied to empirical data in order to compare and contrast depolarization seen in three distinct environments. For environments with significant multipath, the calculated parameters demonstrate that depolarization is a three dimensional effect. This work illustrates that commonly utilized two dimensional formulations do not sufficiently capture the effects of depolarization in complex environments. As wireless IoT systems are deployed in evermore cluttered environments, these results can help determine if antenna systems that are tripolar are warranted. If so, then employing 3D polarization diversity in these scenarios would considerably improve link reliability as compared to the traditional dual polarization, 2D diversity approaches. The provided theory verifies the effectiveness of employing tripolarized systems in multipath conditions.

To explore the necessity of tripolar antennas for improving link reliability in M2M communication systems, the data collected in an environment that emulates M2M systems are analyzed. The wide range of M2M applications suggests that the environments in which they will be deployed can vary greatly in terms of wireless propagation conditions (multipath, line-of-sight (LoS), and non-LoS). Chapter 3 illustrates that these effects, which include severe frequency-selective and depolarization effects in three dimensions, are highly dependent on the placement of the device in the environment. This chapter demonstrates the use of the 10%FD to statistically characterize the environments and a 3D cross-polarization discrimination (XPD) metric to show the three dimensional impact of depolarization.

Motivated by the results presented in Chapters 2 and 3, tripolar antenna system geometries that can be fabricated using 3D printing technologies are investigated in Chapter 4. Over two distinct environments (a highly reflective industrial environment and an NLOS office environment), the experimental results confirm the efficacy of a tripolar antenna array that is not copolar with with its vertically-oriented transmit counterpart and thus meets the build angle constraint faced by 3D printing technology. For each environment, in order to emulate the random placement of the transmitting device, the transmit antenna was moved, in small increments, to 50 different locations and S_{21} channel data was collected at 551 frequencies in the 2.4 GHz ISM band. Subsequently, two distinct 3D printed tripolar antennas are fabricated through additive manufacturing techniques and characterized for operation at 2.4 GHz. Over the air testing demonstrates a 1% channel improvement of up to 14 dB across over 50 locations in a multipath environment and 44% reduction in BER at a representative location.

Multi-polarized channel models are fundamental steps toward developing multi-antenna systems. In these types of channel models, the power imbalance between channel elements that occurs due to antenna polarization, antenna orientation, and propagation channel depolarization should be modeled accurately. The interaction of these three effects is significant, and requires complex channel models to be described completely. In this dissertation, a 3D geometry-based stochastic model is presented in Chapter 5 that considers the interaction between antenna's polarization and channel depolarization effects and is capable of evaluating circular (CP) and linear (LP) dual-polarized systems. The proposed geometrical model uses spatial distributions of scatterers in a shell-like 3D spheroid to build the multipath channel. Analysis of the prop-

agation characteristics of the data shows similarity between measured and simulated diversity gains for non-line-of-sight (NLOS) setting. In NLOS scenario, CP does not exhibit significant improvement in terms of diversity gain compared to LP. However, cross-polarization-discrimination (XPD) results of measurements and simulation shows less power imbalance in CP systems in comparison with LP systems. This fact causes CP systems to be less sensitive where orientation of the receive antenna changes dramatically relative to the transmit antenna. Both the experimental and simulated data proves superiority of CP polarization in the presence of LOS. Then, the proposed model along with the data taken from a simple low-cost omnidirectional antennas are employed to evaluate the hybrid polarization diversity. Hybrid polarization diversity offers to choose between four different polarizations namely, two orthogonal linear and two orthogonal circular polarizations. The experimental and simulated data demonstrate the proposed technique offers substantial benefit in high-multipath environments. The proposed technique can be useful in sensor network applications where sensor nodes should be implemented in very cluttered settings and where easy to manufacture and low-cost antenna solutions are desired.

Finally, in Chapter 6, the millimeter-wave (mmWave) spectrum provides a large bandwidth that can enable multi-Gbps data rate wireless links and thus meets the needs of a variety of forthcoming high bandwidth communication systems such as 5G mobile, in-building, vehicle-to-vehicle, infrastructure-to-vehicle, and wireless data center networks. The 28 GHz bands is currently considered for the next generation of mobile cellular. The channel models for mmWave systems are still nascent; measurements for indoor settings in particular have been limited. Due to unique features of communication at very high frequencies, one cannot expect to apply models developed for lower frequencies. As such, this work presents dual-polarized channel measurements and analysis at 28 GHz in a cluttered environment. Furthermore, 60 GHz frequency band is being considered for the next-generation short-range wireless networks. In this dissertation, a Markov channel model for spatial variations in multipath environments at 60 GHz is presented. Comparison between measurements taken inside a reverberation chamber and synthesized data shows good agreement.

To sum up, tri-polarization and quad polarization diversity improved the 1% link margin by 3-4 dB in comparison with conventional dual-polarized systems in multipath channels. That is, for a quality of service (QoS) of 99% link reliability, the margin or, equivalently, transmit power

could be reduced by over 3-4 dB or by 2-2.5 factor if M = 3 or M = 4 selection diversity is used versus just M = 2 selection diversity. This reduction of the transmitted power can for example be translated into longer time that a mobile phone battery can retain its charge.

7.2 Future Work

There are a number of different ways that the work in this dissertation could be extended. These proposed paths for future research can be classified as follows.

- The current 3D Stokes vector framework provides information about direction of propagation in a channel at different frequencies. Further studies can be conducted to investigate effectiveness of this approach for source localization as it may offer more compact antenna array systems and less computational complexity for this application [120]. Moreover, the extracted polarization indices from three dimensional measurements can be used extensively to characterize depolarization effects in wireless channels over parameters of interest such as time/space/frequency in order to devise more efficient as well as more optimized strategies for improving reliability in these channels.

- The suggested channel model in this dissertation studies dual-polarized systems. However, it can be expanded to model tri-polarized systems. Furthermore, the current model only consider depolarization effects caused by reflection from a smooth surface. To provide a more precise model, other depolarization mechanisms such as diffuse scattering and diffraction are needed to be taken into account. For instance, since many surfaces that are considered smooth in lower frequencies behave like rough surfaces in mmWave band, diffuse scattering plays a significant role in channel depolarization at mmWave band [24, 121]. In future research, diffuse scattering effects can be added to this model for mmWave channel characterization. Knife-edge diffraction (KED) or a creeping wave linear models can also be included in the model to predict diffraction loss around sharp objects [122].

- The tripolar antenna is designed for integration with commercial wireless sensor nodes. Future work can implement these compact, tripolar antennas in hardware to demonstrate the benefits in practice in real wireless network systems. The proposed hybrid polarization diversity technique can be also useful in sensor network applications where sensor nodes

should be implemented in very cluttered settings and where easy to manufacture and low-cost antenna solutions are desired. In future studies implementation of this technique in hardware and its effectiveness in sensor network applications can be tested.

7.3 Final Comments

Characterization and mitigation of fading in wireless communication channels and building channel models is only the beginning of the story and can not be considered as an achievement in itself. Indeed, it is the first step toward building better communications schemes. To exploit the most of the tripolar or quad-polarized antenna designs, it is necessary to develop sensor node communication protocols, coding schemes that exploit the most of these modified designs.

In addition, one of the major tendencies in today's research is multi-user systems. This includes cognitive radios, mesh networks etc. Current channel models including the proposed channel model in this dissertation have been built for single-link systems. The extension of channel models from single-link to multiple-link will be mandatory in order to have reliable models to characterize such pervasive multi-user communication schemes.

References

[1] "EE433: Supplemental homework problem set 5." [Online]. Available: https://www.usna.edu/EE/ee433/homework/EE433_Supplemental_5.pdf

[2] L. Frenzel, "The polarization ellipse," https://www.nrcan.gc.ca/earth-sciences/geomatics/satellite-imagery-air-photos/satellite-imagery-products/educational-resources/9575, 2016, [Online; accessed 2016-03-08].

[3] M. Alsehaili, S. Noghanian, A. R. Sebak, and D. A. Buchanan, "Angle and time of arrival statistics of a three dimensional geometrical scattering channel model for indoor and outdoor propagation environments," *Progress In Electromagnetics Research*, vol. 109, pp. 191–209, 2010.

[4] J. Frolik, V. Sipal, and D. J. Edwards, "Leveraging depolarization to increase the link reliability for wireless sensors operating in Hyper-Rayleigh environments," *Sensors Journal, IEEE*, vol. 14, no. 8, pp. 2442–2446, 2014.

[5] A. F. Molisch, *Wireless communications*. John Wiley & Sons, 2012, vol. 34.

[6] O. A. Amodu and M. Othman, "Machine-to-machine communication: An overview of opportunities," *Computer Networks*, 2018.

[7] P. K. Verma, R. Verma, A. Prakash, A. Agrawal, K. Naik, R. Tripathi, M. Alsabaan, T. Khalifa, T. Abdelkader, and A. Abogharaf, "Machine-to-machine (m2m) communications: A survey," *Journal of Network and Computer Applications*, vol. 66, pp. 83–105, 2016.

[8] W. C. Lee and Y. Yeh, "Polarization diversity system for mobile radio," *Communications, IEEE Transactions on*, vol. 20, no. 5, pp. 912–923, Oct 1972.

[9] R. Vaughan, "Polarization diversity in mobile communications," *Vehicular Technology, IEEE Transactions on*, vol. 39, no. 3, pp. 177–186, Aug 1990.

[10] M. R. Andrews, P. P. Mitra *et al.*, "Tripling the capacity of wireless communications using electromagnetic polarization," *Nature*, vol. 409, no. 6818, pp. 316–318, 2001.

[11] A. Goldsmith, *Wireless communications*. Cambridge University Press, 2005.

[12] J. Frolik and M. Golmohamadi, "On random and multidimensional channel effects in cluttered environments," *IEEE Antennas and Wireless Propagation Letters*, vol. 16, pp. 1863–1866, 2017.

[13] J. Milanović, S. Rimac-Drlje, and I. Majerski, "Radio wave propagation mechanisms and empirical models for fixed wireless access systems," *Tehnički vjesnik*, vol. 17, no. 1, pp. 43–53, 2010.

[14] J. Lekner, *Theory of reflection*. Springer, 1987.

[15] T. S. Rappaport, G. R. MacCartney, S. Sun, H. Yan, and S. Deng, "Small-scale, local area, and transitional millimeter wave propagation for 5G communications," *IEEE Transactions on Antennas and Propagation*, vol. 65, no. 12, pp. 6474–6490, 2017.

[16] F. Mani and C. Oestges, "Evaluation of diffuse scattering contribution for delay spread and crosspolarization ratio prediction in an indoor scenario," in *Antennas and Propagation (EuCAP), 2010 Proceedings of the Fourth European Conference on*. IEEE, 2010, pp. 1–4.

[17] V. Degli-Esposti, F. Fuschini, E. M. Vitucci, and G. Falciasecca, "Measurement and modelling of scattering from buildings," *IEEE Transactions on Antennas and Propagation*, vol. 55, no. 1, pp. 143–153, 2007.

[18] (2014) S-parameter measurements basics for high speed digital engineers. [Online]. Available: http://literature.cdn.keysight.com/litweb/pdf/5991-3736EN.pdf

[19] S. Ramaswamy and V. Raghavan, "A comparative study of rayleigh fading wireless channel simulators," Ph.D. dissertation, Texas A&M University, 2006.

[20] T. S. Rappaport *et al.*, *Wireless communications: principles and practice*. prentice hall PTR New Jersey, 1996, vol. 2.

[21] G. D. Durgin, *Space-time wireless channels*. Prentice Hall Professional, 2003.

[22] W. L. Stutzman, *Polarization in electromagnetic systems*. Artech house, 2018.

[23] J. J. Gil and I. San José, "3D polarimetric purity," *Optics Communications*, vol. 283, no. 22, pp. 4430–4434, 2010.

[24] F. Quitin, "Channel modeling for polarized MIMO systems," PhD dissertation, Université libre de Bruxelles, 2011.

[25] J. M. Albornoz, "A wideband channel sounder," Ph.D. dissertation, The Ohio State University, 2001.

[26] M. F. Iskander and Z. Yun, "Propagation prediction models for wireless communication systems," *IEEE Transactions on microwave theory and techniques*, vol. 50, no. 3, pp. 662–673, 2002.

[27] T. S. Rappaport, S. Y. Seidel, and K. Takamizawa, "Statistical channel impulse response models for factory and open plan building radio communicate system design," *IEEE Transactions on Communications*, vol. 39, no. 5, pp. 794–807, 1991.

[28] S.-C. Kwon and G. L. Stuber, "Geometrical theory of channel depolarization," *IEEE Transactions on Vehicular Technology*, vol. 60, no. 8, pp. 3542–3556, 2011.

[29] J. C. Liberti and T. S. Rappaport, "A geometrically based model for line-of-sight multipath radio channels," in *Vehicular Technology Conference, 1996. Mobile Technology for the Human Race., IEEE 46th*, vol. 2. IEEE, 1996, pp. 844–848.

[30] M. Golmohamadi and J. Frolik, "Depolarization in three dimensions: Theoretical formulations and empirical results," in *2016 IEEE 17th Annual Wireless and Microwave Technology Conference (WAMICON)*. IEEE, Apr 2016. [Online]. Available: https://doi.org/10.1109/wamicon.2016.7483834

[31] A. Konanur, K. Gosalia, S. Krishnamurthy, B. Hughes, and G. Lazzi, "Increasing wireless channel capacity through MIMO systems employing co-located antennas," *Microwave Theory and Techniques, IEEE Transactions on*, vol. 53, no. 6, pp. 1837–1844, June 2005.

[32] N. Das, T. Inoue, T. Taniguchi, and Y. Karasawa, "An experiment on MIMO system having three orthogonal polarization diversity branches in multipath-rich environment," in *Vehicular Technology Conference, 2004. VTC2004-Fall. 2004 IEEE 60th*, vol. 2, Sept 2004, pp. 1528–1532 Vol. 2.

[33] D. Stancil, A. Berson, J. Van't Hof, R. Negi, S. Sheth, and P. Patel, "Doubling wireless channel capacity using co-polarised, co-located electric and magnetic dipoles," *Electronics Letters*, vol. 38, no. 14, pp. 746–747, 2002.

[34] R. Tian and B. K. Lau, "Experimental verification of degrees of freedom for colocated antennas in wireless channels," *Antennas and Propagation, IEEE Transactions on*, vol. 60, no. 7, pp. 3416–3423, 2012.

[35] S. Salous, *Radio propagation measurement and channel modelling*. John Wiley & Sons, 2013.

[36] M. I. Mishchenko, L. D. Travis, and A. A. Lacis, *Scattering, absorption, and emission of light by small particles*. Cambridge university press, 2002.

[37] T. Setälä, A. Shevchenko, M. Kaivola, and A. T. Friberg, "Degree of polarization for optical near fields," *Physical Review E*, vol. 66, no. 1, p. 016615, 2002.

[38] J. J. Gil, "Interpretation of the coherency matrix for three-dimensional polarization states," *Physical Review A*, vol. 90, no. 4, p. 043858, 2014.

[39] W. Keusgen, "On limits of wireless communications when using multiple dual-polarized antennas," in *Telecommunications, 2003. ICT 2003. 10th International Conference on*, vol. 1. IEEE, 2003, pp. 204–210.

[40] M.-T. Dao, V.-A. Nguyen, Y.-T. Im, S.-O. Park, and G. Yoon, "3D polarized channel modeling and performance comparison of mimo antenna configurations with different polarizations," *Antennas and Propagation, IEEE Transactions on*, vol. 59, no. 7, pp. 2672–2682, 2011.

[41] B. Lindmark and M. Nilsson, "On the available diversity gain from different dual-polarized antennas," *Selected Areas in Communications, IEEE Journal on*, vol. 19, no. 2, pp. 287–294, 2001.

[42] R. Sabry, "A novel field scattering formulation for polarimetric synthetic aperture radar: 3D scattering and stokes vectors," *Progress In Electromagnetics Research M*, vol. 27, pp. 129–150, 2012.

[43] J. J. Gil, "Polarimetric characterization of light and media," *The European Physical Journal Applied Physics*, vol. 40, no. 01, pp. 1–47, 2007.

[44] J. Ellis and A. Dogariu, "On the degree of polarization of random electromagnetic fields," *Optics communications*, vol. 253, no. 4-6, pp. 257–265, 2005.

[45] M. R. Dennis, "A three-dimensional degree of polarization based on Rayleigh scattering," *JOSA A*, vol. 24, no. 7, pp. 2065–2069, 2007.

[46] T. G. Pratt, H. Tapse, B. Walkenhorst, and G. Acosta-Marum, "A modified XPC characterization for polarimetric channels," *IEEE Transactions on Vehicular Technology*, vol. 60, no. 7, pp. 2904–2913, 2011.

[47] M. Migliaccio, J. J. Gil, A. Sorrentino, F. Nunziata, and G. Ferrara, "The polarization purity of the electromagnetic field in a reverberating chamber," *IEEE Transactions on Electromagnetic Compatibility*, vol. 58, no. 3, pp. 694–700, 2016.

[48] T. Carozzi, R. Karlsson, and J. Bergman, "Parameters characterizing electromagnetic wave polarization," *Physical Review E*, vol. 61, no. 2, p. 2024, 2000.

[49] G. Bosyk, G. Bellomo, and A. Luis, "Polarization monotones of two-dimensional and three-dimensional random electromagnetic fields," *Physical Review A*, vol. 97, no. 2, p. 023804, 2018.

[50] C. Brosseau and R. Barakat, "Dimensionality of the coherency matrix in polarization optics," *Optics communications*, vol. 91, no. 5-6, pp. 408–415, 1992.

[51] R. A. Ramirez, M. Golmohamadi, J. Frolik, and T. M. Weller, "3D printed on-package tripolar antennas for mitigating harsh channel conditions," in *Radio and Wireless Symposium (RWS), 2017 IEEE*. IEEE, 2017, pp. 62–64.

[52] J. Frolik, T. M. Weller, S. DiStasi, and J. Cooper, "A compact reverberation chamber for hyper-Rayleigh channel emulation," *Antennas and Propagation, IEEE Transactions on*, vol. 57, no. 12, pp. 3962–3968, 2009.

[53] E. Genender, C. L. Holloway, K. A. Remley, J. M. Ladbury, G. Koepke, and H. Garbe, "Simulating the multipath channel with a reverberation chamber: Application to bit error rate measurements," *IEEE Transactions on electromagnetic compatibility*, vol. 52, no. 4, pp. 766–777, 2010.

[54] J. Frolik, "A practical metric for fading environments," *Wireless Communications Letters, IEEE*, vol. 2, no. 2, pp. 195–198, 2013.

[55] L. Lukama, K. Konstantinou, and D. J. Edwards, "Performance of a three-branch orthogonal polarization diversity scheme," in *Vehicular Technology Conference, 2001. VTC 2001 Fall. IEEE VTS 54th*, vol. 4. IEEE, 2001, pp. 2033–2037.

[56] C.-Y. Chiu, J.-B. Yan, and R. D. Murch, "Compact three-port orthogonally polarized MIMO antennas," *Antennas and Wireless Propagation Letters, IEEE*, vol. 6, pp. 619–622, 2007.

[57] C. Oikonomopoulos-Zachos, "Double layer compact four-port antenna using a symmetrical feeding technique for future MIMO antenna systems at 5.6 GHz," in *2010 IEEE Antennas and Propagation Society International Symposium*, 2010.

[58] M. Golmohamadi, R. Ramirez, B. Hewgill, J. Jamison, J. Frolik, and T. Weller, "Characterization of a geometrically constrained tripolar antenna under m2m channel conditions," in *Antennas and Propagation (EUCAP), 2017 11th European Conference on*. IEEE, 2017, pp. 2998–3002.

[59] J. Frolik, "Mitigating severe channel effects using tripolar antenna diversity," in *2015 9th European Conference on Antennas and Propagation (EuCAP)*. IEEE, 2015, pp. 1–4.

[60] R. A. Ramirez, E. A. Rojas-Nastrucci, and T. M. Weller, "3D tag with improved read range for UHF RFID applications using additive manufacturing," in *Wireless and Microwave Technology Conference (WAMICON), 2015 IEEE 16th Annual*. IEEE, 2015, pp. 1–4.

[61] B. K. Tehrani, B. S. Cook, and M. M. Tentzeris, "Inkjet-printed 3D interconnects for millimeter-wave system-on-package solutions," in *2016 IEEE MTT-S International Microwave Symposium (IMS)*. IEEE, 2016, pp. 1–4.

[62] J. A. Paulsen, M. Renn, K. Christenson, and R. Plourde, "Printing conformal electronics on 3D structures with aerosol jet technology," in *Future of Instrumentation International Workshop (FIIW), 2012*. IEEE, 2012, pp. 1–4.

[63] D. Hawatmeh, E. Rojas-Nastrucci, and T. Weller, "A multi-material 3D printing approach for conformal microwave antennas," in *2016 International Workshop on Antenna Technology (iWAT)*. IEEE, 2016, pp. 7–10.

[64] P.-S. Kildal, K. Rosengren, J. Byun, and J. Lee, "Definition of effective diversity gain and how to measure it in a reverberation chamber," *Microwave and Optical Technology Letters*, vol. 34, no. 1, pp. 56–59, 2002.

[65] Y. Mehmood, N. Haider, M. Imran, A. Timm-Giel, and M. Guizani, "M2M communications in 5G: State-of-the-art architecture, recent advances, and research challenges," *IEEE Communications Magazine*, vol. 55, no. 9, pp. 194–201, 2017.

[66] "Global machine to machine (M2M) market," Jul. 2017, http://www.marketsandmarkets.com/Market-Reports/machine-to-machine-market-732.html.

[67] "Projected machine-to-machine industry size," Nov. 2016, https://www.statista.com/topics/1843/m2m-machine-to-machine.

[68] M. Golmohamadi, R. Ramirez, B. Hewgill, J. Jamison, J. Frolik, and T. Weller, "Characterization of a geometrically constrained tripolar antenna under M2M channel conditions," in *Antennas and Propagation (EUCAP), 2017 11th European Conference on.* IEEE, 2017, pp. 2998–3002.

[69] W. C. Jakes and D. C. Cox, *Microwave mobile communications.* Wiley-IEEE Press, 1994.

[70] L. Simic, S. M. Berber, and K. W. Sowerby, "Energy-efficiency of cooperative diversity techniques in wireless sensor networks," in *2007 IEEE 18th International Symposium on Personal, Indoor and Mobile Radio Communications.* IEEE, 2007. [Online]. Available: https://doi.org/10.1109/pimrc.2007.4394562

[71] B. Kusy, D. Abbott, C. Richter, C. Huynh, M. Afanasyev, W. Hu, M. Brünig, D. Ostry, and R. Jurdak, "Radio diversity for reliable communication in sensor networks," *ACM Transactions on Sensor Networks (TOSN)*, vol. 10, no. 2, p. 32, 2014.

[72] L. Vallozzi, H. Rogier, and C. Hertleer, "Dual polarized textile patch antenna for integration into protective garments," *IEEE Antennas and Wireless Propagation Letters*, vol. 7, pp. 440–443, 2008.

[73] P. Vanveerdeghem, P. Van Torre, C. Stevens, J. Knockaert, and H. Rogier, "Flexible dual-diversity wearable wireless node integrated on a dual-polarised textile patch antenna," *IET Science, Measurement & Technology*, vol. 8, no. 6, pp. 452–458, 2014.

[74] D. Edwards, T. Hao, W. Malik, and C. Stevens, "Planar tripolar antenna," May 15 2012, US Patent 8,179,325.

[75] R. A. Ramirez, D. Lugo, T. M. Weller, M. Golmohamadi, and J. Frolik, "Additive manufactured tripolar antenna system for link improvement in high multipath environments," in *Antennas and Propagation & USNC/URSI National Radio Science Meeting, 2017 IEEE International Symposium on.* IEEE, 2017, pp. 2539–2540.

[76] T. P. Ketterl, Y. Vega, N. C. Arnal, J. W. Stratton, E. A. Rojas-Nastrucci, M. F. Córdoba-Erazo, M. M. Abdin, C. W. Perkowski, P. I. Deffenbaugh, K. H. Church *et al.*, "A 2.45 GHz phased array antenna unit cell fabricated using 3D multi-layer direct digital manufacturing," *IEEE Transactions on Microwave Theory and Techniques*, vol. 63, no. 12, pp. 4382–4394, 2015.

[77] A. L. Vera-López, E. A. Rojas-Nastrucci, M. Córdoba-Erazo, T. Weller, and J. Papapolymerou, "Ka-band characterization and RF design of acrynolitrile butadiene styrene (ABS)," in *2015 IEEE MTT-S International Microwave Symposium.* IEEE, May 2015. [Online]. Available: https://doi.org/10.1109/mwsym.2015.7167121

[78] P. I. Deffenbaugh, T. M. Weller, and K. H. Church, "Fabrication and microwave characterization of 3D printed transmission lines," *IEEE Microwave and wireless components letters*, vol. 25, no. 12, pp. 823–825, 2015.

[79] P. Deffenbaugh, K. Church, J. Goldfarb, and X. Chen, "Fully 3D printed 2.4 GHz bluetooth/wi-Fi antenna," in *International Symposium on Microelectronics*, vol. 2013, no. 1. International Microelectronics Assembly and Packaging Society, 2013, pp. 914–920.

[80] N.A, "Nscrypt, micro-dispensing," 2017, https://www.nscrypt.com/micro-dispensing/. [Online]. Available: https://www.nscrypt.com/micro-dispensing/

[81] S. M. Mikki and Y. M. Antar, "On cross correlation in antenna arrays with applications to spatial diversity and MIMO systems," *IEEE Transactions on Antennas and Propagation*, vol. 63, no. 4, pp. 1798–1810, 2015.

[82] K. R. Jha and S. K. Sharma, "Combination of MIMO antennas for handheld devices [Wireless Corner]," *IEEE Antennas and Propagation Magazine*, vol. 60, no. 1, pp. 118–131, 2018.

[83] N. P. Lawrence, C. Fumeaux, and D. Abbott, "Planar triorthogonal diversity slot antenna," *IEEE Transactions on Antennas and Propagation*, vol. 65, no. 3, pp. 1416–1421, 2017.

[84] J. Frolik, T. M. Weller, S. DiStasi, and J. Cooper, "A compact reverberation chamber for hyper-Rayleigh channel emulation," *IEEE Transactions on Antennas and Propagation*, vol. 57, no. 12, pp. 3962–3968, 2009.

[85] X. Chen and P.-S. Kildal, "Accuracy of antenna input reflection coefficient and mismatch factor measured in reverberation chamber," in *Antennas and Propagation, 2009. EuCAP 2009. 3rd European Conference on.* IEEE, 2009, pp. 2678–2681.

[86] N. Wisitpongphan, G. Ferrari, S. Panichpapiboon, J. Parikh, and O. Tonguz, "QoS provisioning using BER-based routing in ad hoc wireless networks," in *Vehicular Technology Conference, 2005. VTC 2005-Spring. 2005 IEEE 61st*, vol. 4. IEEE, 2005, pp. 2483–2487.

[87] T. Yélémou, J. Ledy, B. Hilt, A.-M. Poussard, and P. Meseure, "Performance comparison of BER-based routing protocols under realistic conditions," in *Local Computer Networks (LCN), 2011 IEEE 36th Conference on.* IEEE, 2011, pp. 259–262.

[88] T. S. Rappaport and D. A. Hawbaker, "Wide-band microwave propagation parameters using circular and linear polarized antennas for indoor wireless channels," *IEEE Transactions on Communications*, vol. 40, no. 2, pp. 240–245, 1992.

[89] A. Kajiwara, "Line-of-sight indoor radio communication using circular polarized waves," *IEEE Transactions on Vehicular Technology*, vol. 44, no. 3, pp. 487–493, 1995.

[90] T. Manabe, K. Sato, H. Masuzawa, K. Taira, T. Ihara, Y. Kasashima, and K. Yamaki, "Polarization dependence of multipath propagation and high-speed transmission characteristics of indoor millimeter-wave channel at 60 GHz," *IEEE Transactions on Vehicular Technology*, vol. 44, no. 2, pp. 268–274, 1995.

[91] F. Yildirim, A. S. Sadri, and H. Liu, "Polarization effects for indoor wireless communications at 60 GHz," *IEEE Communications Letters*, vol. 12, no. 9, 2008.

[92] Y. Zhang, L. Pang, X. Liang, X. Liu, R. Chen, and J. Li, "Propagation characteristics of circularly and linearly polarized electromagnetic waves in urban macrocell scenario," *IEEE Transactions on Vehicular Technology*, vol. 64, no. 1, pp. 209–222, 2015.

[93] J. Wang, Z. Lv, and X. Li, "Analysis of MIMO diversity improvement using circular polarized antenna," *International Journal of Antennas and Propagation*, vol. 2014, 2014.

[94] O. Landron, M. J. Feuerstein, and T. S. Rappaport, "In situ microwave reflection coefficient measurements for smooth and rough exterior wall surfaces," in *Proceedings IEEE Vehicular Technology Conference*, 1993, pp. 77–80.

[95] A. I. Lvovsky, "Fresnel equations," *Encyclopedia of Optical Engineering*, pp. 1–6, 2013.

[96] B. Gaffney and M. McLaughlin, "White Paper: Comparison of Narrowband and Ultra Wideband Channels," DecaWave, Tech. Rep., 01 2008.

[97] Z. Hossain, C. Mollica, and J. M. Jornet, "Stochastic multipath channel modeling and power delay profile analysis for terahertz-band communication," in *Proceedings of the 4th ACM International Conference on Nanoscale Computing and Communication.* ACM, 2017, p. 32.

[98] T. Zwick, C. Fischer, and W. Wiesbeck, "A stochastic multipath channel model including path directions for indoor environments," *IEEE journal on Selected Areas in Communications*, vol. 20, no. 6, pp. 1178–1192, 2002.

[99] M. Lu, T. Lo, and J. Litva, "A physical spatio-temporal model of multipath propagation channels," in *Vehicular Technology Conference, 1997, IEEE 47th*, vol. 2. IEEE, 1997, pp. 810–814.

[100] H. Hashemi, "Impulse response modeling of indoor radio propagation channels," *IEEE journal on selected areas in communications*, vol. 11, no. 7, pp. 967–978, 1993.

[101] R. Wilson, "Propagation losses through common building materials 2.4 GHz vs 5 GHz," *Magis Networks Inc.: San Diego, CA, USA*, 2002.

[102] D. K. Cheng *et al.*, *Field and wave electromagnetics*. Pearson Education India, 1989.

[103] F. Yildirim, A. S. Sadri, and H. Liu, "Polarization effects for indoor wireless communications at 60 GHz," *IEEE Communications Letters*, vol. 12, no. 9, 2008.

[104] F. Ferrero, C. Luxey, R. Staraj, G. Jacquemod, M. Yedlin, and V. Fusco, "A novel quad-polarization agile patch antenna," *IEEE Transactions on Antennas and Propagation*, vol. 57, no. 5, pp. 1563–1567, 2009.

[105] W. Cao, B. Zhang, A. Liu, T. Yu, D. Guo, and K. Pan, "A reconfigurable microstrip antenna with radiation pattern selectivity and polarization diversity," *IEEE Antennas and Wireless Propagation Letters*, vol. 11, pp. 453–456, 2012.

[106] Y.-F. Wu, C.-H. Wu, D.-Y. Lai, and F.-C. Chen, "A reconfigurable quadri-polarization diversity aperture-coupled patch antenna," *IEEE Transactions on Antennas and Propagation*, vol. 55, no. 3, pp. 1009–1012, 2007.

[107] A. Narbudowicz, X. Bao, M. J. Ammann, H. Shakhtour, and D. Heberling, "Circularly polarized antenna with steerable dipole-like radiation pattern," *IEEE Transactions on Antennas and Propagation*, vol. 62, no. 2, pp. 519–526, 2014.

[108] D. Yu, S.-X. Gong, Y.-T. Wan, Y.-L. Yao, Y.-X. Xu, and F.-W. Wang, "Wideband omnidirectional circularly polarized patch antenna based on vortex slots and shorting vias," *IEEE Transactions on Antennas and Propagation*, vol. 62, no. 8, pp. 3970–3977, 2014.

[109] A. Narbudowicz, X. Bao, and M. J. Ammann, "Omnidirectional microstrip patch antenna with reconfigurable pattern and polarisation," *IET Microwaves, Antennas and Propagation*, vol. 8, no. 11, pp. 872–877, 2014.

[110] M. Golmoharnadi, S. Chowdhury, J. Jamison, E. Kravitz, and J. Frolik, "28 GHz channel measurements in high multipath, indoor environments," in *2018 IEEE International Symposium on Antennas and Propagation & USNC/URSI National Radio Science Meeting*. IEEE, 2018, pp. 767–768.

[111] M. Golmohamadi, S. Chowdhury, and J. Frolik, "Markov modeling of spatial variations in multipath," in *Antennas and Propagation & USNC/URSI National Radio Science Meeting, 2017 IEEE International Symposium on*. IEEE, 2017, pp. 611–612.

[112] H. Zhao, R. Mayzus, S. Sun, M. Samimi, J. K. Schulz, Y. Azar, K. Wang, G. N. Wong, F. Gutierrez, and T. S. Rappaport, "28 GHz millimeter wave cellular communication measurements for reflection and penetration loss in and around buildings in new york city," in *Communications (ICC), 2013 IEEE International Conference on*. IEEE, 2013, pp. 5163–5167.

[113] X. Wu, Y. Zhang, C.-X. Wang, G. Goussetis, M. M. Alwakeel *et al.*, "28 GHz indoor channel measurements and modelling in laboratory environment using directional antennas," in *Antennas and Propagation (EuCAP), 2015 9th European Conference on.* IEEE, 2015, pp. 1–5.

[114] H. S. Wang and N. Moayeri, "Finite-state Markov channel-a useful model for radio communication channels," *IEEE transactions on vehicular technology*, vol. 44, no. 1, pp. 163–171, 1995.

[115] I. Sen and D. W. Matolak, "Vehicle–vehicle channel models for the 5-GHz band," *IEEE Transactions on Intelligent Transportation Systems*, vol. 9, no. 2, pp. 235–245, 2008.

[116] S. Lin, L. Kong, L. He, K. Guan, B. Ai, Z. Zhong, and C. Briso-Rodríguez, "Finite-state Markov modeling for high-speed railway fading channels," *IEEE Antennas and Wireless Propagation Letters*, vol. 14, pp. 954–957, 2015.

[117] T. Zwick, C. Fischer, and W. Wiesbeck, "A stochastic multipath channel model including path directions for indoor environments," *IEEE journal on Selected Areas in Communications*, vol. 20, no. 6, pp. 1178–1192, 2002.

[118] E. S. Sousa, V. M. Jovanovic, and C. Daigneault, "Delay spread measurements for the digital cellular channel in Toronto," *IEEE Transactions on Vehicular Technology*, vol. 43, no. 4, pp. 837–847, 1994.

[119] J. Frolik, "A case for considering hyper-Rayleigh fading channels," *IEEE Transactions on Wireless Communications*, vol. 6, no. 4, pp. 1235–1239, 2007.

[120] J. Bergman, T. Carozzi, and R. Karlsson, "Method and system for obtaining direction of an electromagnetic wave," Jun. 18 2002, uS Patent 6,407,702.

[121] R. Piesiewicz, C. Jansen, D. Mittleman, T. Kleine-Ostmann, M. Koch, and T. Kurner, "Scattering analysis for the modeling of THz communication systems," *IEEE Transactions on Antennas and Propagation*, vol. 55, no. 11, pp. 3002–3009, 2007.

[122] T. S. Rappaport, G. R. MacCartney, S. Sun, H. Yan, and S. Deng, "Small-scale, local area, and transitional millimeter wave propagation for 5G communications," *IEEE Transactions on Antennas and Propagation*, vol. 65, no. 12, pp. 6474–6490, 2017.